



Studies on the spinnability and surface modification of polycaprolactone nanofibers produced by AC electrospinning

Dissertation Thesis

Study programme:

P3106 Textile Engineering

Study branch:

Textile Technics and Materials Engineering

Author:

Manikandan Sivan, M.Sc.

Thesis Supervisor:

prof. RNDr. David Lukáš, CSc.
Department of Chemistry



Declaration

I hereby certify, I, myself, have written my dissertation as an original and primary work using the literature listed below and consulting it with my thesis supervisor and my thesis counsellor.

I acknowledge that my dissertation is fully governed by Act No. 121/2000 Coll., the Copyright Act, in particular Article 60 – School Work.

I acknowledge that the Technical University of Liberec does not infringe my copyrights by using my dissertation for internal purposes of the Technical University of Liberec.

I am aware of my obligation to inform the Technical University of Liberec on having used or granted license to use the results of my dissertation; in such a case the Technical University of Liberec may require reimbursement of the costs incurred for creating the result up to their actual amount.

At the same time, I honestly declare that the text of the printed version of my dissertation is identical with the text of the electronic version uploaded into the IS/STAG.

I acknowledge that the Technical University of Liberec will make my dissertation public in accordance with paragraph 47b of Act No. 111/1998 Coll., on Higher Education Institutions and on Amendment to Other Acts (the Higher Education Act), as amended.

I am aware of the consequences which may under the Higher Education Act result from a breach of this declaration.

September 15, 2022

Manikandan Sivan, M.Sc.

Abstract

The world's oldest (34000 years) textile-based fibrous imprints have been excavated from the Czech Republic (Nové Pavlovice), indicating this region's technological richness even during the Upper Paleolithic period. In this millennium, industrial-level fabrication of electrospun nanofibers and composite electrospun nanofibrous yarns have emerged from the Czech Republic through the invention of various electrospinning technologies like NanospiderTM and alternating current (AC) electrospinning. These two technologies were developed at the Technical University of Liberec (TUL); Prof. Jirsak's group created the NanospiderTM, and Prof. Lukas's group created the AC electrospinning. The electrospinning technique is driven by electrohydrodynamic phenomena; an electric force is used to draw charged liquid jets from the polymer solutions, followed by the creation of dried electrospun fibers through various instabilities and rapid solvent evaporation.

Direct current (DC) high voltage is widely used in electrospinning technology to create electrospun fibers from various polymeric liquids or melts. Although AC high voltage has unique features, such as it can be supplied in various waveforms and frequencies, compact fibrous plume formation, and works without an electrically active collector, its impact of the utilization on the polymer's electrospinnability remains unclear. Hence, the first objective is to study the AC spinnability of polycaprolactone (PCL) as the function of various less toxic solvents, polymer concentration, and AC high voltage. PCL was chosen due to its potential use in a broad range of biomedical and tissue engineering applications. Highly toxic volatile organic solvent systems have been traditionally used to fabricate the PCL nanofibers. However, in this thesis, various PCL electrospun nanofibrous scaffolds (ENS) were fabricated by making use of a benign solvent system, such as formic acid (F), formic acid/acetic acid (FA), and formic acid/acetic acid/acetone (FAA). The obtained results revealed that the acidic nature of F and FA promoted the acid-catalyzed degradation of PCL ester bonds and consequently decreased PCL's molecular weight over time. Thus, the FAA solvent system was invented first time by the author to improve the PCL stability in the spinning solution. Additionally, PCL in the FAA solvent system (FAA-PCL) reflects better spinnability accompanied by a six times higher degree of ENS productivity (12.4 ± 0.3 g/h). The resultant ENSs were also biocompatible with mouse fibroblast cells.

Since AC high-voltage can be manipulated via various waveforms and frequencies, the second objective is to study its impacts on AC spinnability. This study hypothesizes that the AC electrospinnability, morphology, scale, and productivity of PCL electrospun nanofibers are dependent on both the waveform and the frequency of the AC high-voltage signal. Herein, 10 wt% FAA-PCL was used owing to its better AC spinnability. In order to

focus only on the impacts of various waveforms (square, sine, and triangle) and frequencies (10, 20, 30, 40, 50, and 60 Hz) on the PCL's spinnability, other technological parameters such as applied high-voltage (50 kV), spinneret's geometry (spinneret's surface diameter is 2.5 cm), and spinneret to collector distance (22 cm) were kept constant for all the experiments. To get a stable plume of fibers, the peripheral speed of the cylindrical collector (30 – 40 m/min) and the solution feeding rate (14 – 18 mL/m) were slightly adjusted according to waveform and/or frequency. The obtained results demonstrated that both the waveform and the frequency of the applied high voltage signal (50 kV_{RMS}) significantly affect the formation of a stable fibrous plume and the PCL electrospun nanofiber (ENF) morphology. Consequently, trimodal– (beads, spindles, and helical), bimodal– (beads and spindles), and unimodal–structured ENF morphologies were attained for square, sine, and triangle waveforms, respectively. Moreover, the frequency of the waveform directly influences the number of beads and/or spindles per unitary fiber length. The square waveform reflects higher productivity (23.6 ± 0.4 g/h) than the sine (16.5 ± 0.3 g/h) and triangle waveform (6.9 ± 0.2 g/h).

It is interesting that although the electrospun fibers were created under the electric field, which contains the ions, free electrons, as well as x-rays, the original chemical structure of the precursor material was not changed. Hence, the PCL electrospun nanofibrous mat (ENM) was exposed to plasma discharge generated by argon or nitrogen discharge gases. Subsequently, the plasma treatment effects on ENM's morphology, wettability, surface functional groups, crystallite size, crystallinity, crystallization temperature, and melting temperature were analyzed. The various PCL ENMs were obtained through the AC electrospinning process using 10 wt% F–PCL, FA–PCL, and FAA–PCL precursor solutions. The experimental results revealed that without compromising the surface morphology of PCL ENMs, the water contact angle was significantly decreased from 136° to approximately 35° and 42° for nitrogen and argon plasma-treated samples, respectively, which was correlated to the substantial increase in surface polar oxygen and nitrogen functional groups. Moreover, the crystallite size and crystallinity degree of PCL ENM were also not significantly altered by the conducted plasma treatments.

Overall it can be concluded that this study will inspire the academic and industrial communities to fabricate various polymeric nanofibers on a large scale using the AC electrospinning technique. Also, it presents a simple approach to the industrial–scale fabrication of PCL ENF via the tuning of the AC high-voltage signal shape and/or frequency with the added advantage of the potential for obtaining a range of PCL ENF morphologies. The plasma treatment results revealed that the surface properties of the PCL ENMs could

be positively affected while maintaining their beneficial bulk properties, thereby making these plasma-modified ENMs excellent candidates in multiple biomedical and tissue engineering applications.

Keywords: AC electrospinning; Waveform; Frequency; Nanofibers; Morphology; Productivity; Polycaprolactone; Benign solvents; Plasma treatment.

Abstrakt

Nejstarší otisky textilních vláken na světě (34000 let) byly nalezeny v České republice (Nové Pavlovice), což svědčí o technologické tradici této oblasti již v období staršího paleolitu. V současném tisíciletí byl zde učiněn objev průmyslové výroby nanovláken (tak zvané elektrické zvlákňování) a výroby kompozitních nanovláknenných přízí díky vynálezům jako je NanospiderTM a elektrické zvlákňování střídavým proudem (AC electrospinning). Tyto dvě technologie byly vyvinuty na Technické univerzitě v Liberci (TUL); Skupina prof. Jirsáka vynalezla technologii NanospiderTM a skupina prof. Lukáše vytvořila AC elektrické zvlákňování. Technologie elektrického zvlákňování jsou založeny na elektrohydrodynamických jevech; elektrická síla se používá k vytvoření nabitých kapalinových trysek z polymerních roztoků, následuje vytvoření pevných nanovláken prostřednictvím různých nestabilit a rychlého odpařování rozpouštědla.

Stejněsměrné (DC) vysoké napětí je široce používáno v technologii elektrostatického zvlákňování k tvorbě nanovláken z různých polymerních kapalin nebo tavenin. Ačkoli má střídavé vysoké napětí vzhledem k elektrickému zvlákňování jedinečné vlastnosti, jakými jsou různé tvary jeho vlny a frekvence, tvorba kompaktní nanovláknenné vlečky a elektrické zvlákňování bez elektricky aktivního kolektoru, jeho dopad na zvláknitelnost polymerních roztoků zůstává zatím neprobádaný. Prvním cílem této práce je studovat AC elektrické zvlákňování polykaprolaktonu (PCL) v závislosti na volbě různých méně toxických rozpouštědel, koncentraci polymeru a střídavého vysokého napětí (25 a 32 kV_{RMS}) a na frekvenci vysokonapětového pole. PCL byl vybrán kvůli potenciálnímu využití v širokém spektru aplikací biomedicínského a tkáňového inženýrství. K výrobě nanovláken z PCL se tradičně používají systémy vysoce toxických těkavých organických rozpouštědel. V této práci však byly laboratorně vyrobeny různé PCL nanovláknenné scaffoldy (ENS) s použitím benigního/zdravotně nezávadného systému rozpouštědel, jako je kyselina mravenčí (F), kyselina mravenčí/kyselina octová (FA) a kyselina mravenčí/kyselina octová/aceton (FAA). Získané výsledky ukázaly, že kyselá povaha F a FA podporovala kyselé katalyzovanou degradaci esterových vazeb PCL a následně snižovala molekulovou hmotnost PCL v průběhu času. Rozpouštědlový systém FAA byl vyvinut autorem pro zlepšení stability PCL ve zvlákňovacím roztoku. Navíc PCL v systému rozpouštědel FAA (FAA-PCL) vykazuje lepší zvláknitelnost doprovázenou šestkrát vyšší produktivitou výroby nanovláknenných vrstev vyrobených elektrickým zvlákňováním (ENS) (12,4 ± 0,3 g/h). Výsledné ENS byly také biokompatibilní s myšími fibroblastovými buňkami.

Vzhledem k tomu, že charakter střídavého vysokého napětí lze měnit pomocí různých tvarů vln a frekvencí, druhým cílem této práce je studovat jejich dopady na elektrické

zvlákňování účinkem střídavého proudu. Na počátku práce jsem vyslovil hypotézu, že AC elektrické zvlákňování změnou tvaru vlny a frekvence umožňuje měnit morfologii vláken, jejich průměry a produktivitu výroby PCL nanovlákných vrstev. V práci jsem používal 10 % hmotn. FAA-PCL kvůli jeho lepší AC zvlákňování. V práci jsem se soustředil na dopady různých průběhů vlny (čtverec, sinus a trojúhelník) a frekvencí (10, 20, 30, 40, 50 a 60 Hz) na zvlákňovitost PCL. Dále jsem studoval další technologické parametry, jako je aplikované vysoké napětí (50 kV_{RMS}), geometrie zvlákňovací trysky (průměr pracovního povrchu zvlákňovací trysky je 2,5 cm) a vzdálenost zvlákňovací trysky k elektricky neutrálnímu kolektoru (22 cm). Tyto parametry byly udržovány konstantní pro všechny experimenty. Pro získání stabilní nanovlákné vlečky byla obvodová rychlost válcového kolektoru (30 – 40 m/min) a rychlost dávkování roztoku do tyčové zvlákňovací elektrody (14 – 18 mL/m) mírně upraveny podle tvaru vlny a/nebo frekvence. Získané výsledky prokázaly, že jak tvar vlny, tak frekvence aplikovaného vysokonapět'ového signálu (50 kV) významně ovlivňují tvorbu stabilní vláknité vlečky a morfologii PCL nanovláken (ENF). Následně bylo dosaženo trimodální nanovlákné struktury (obsahující kapky, vřetena a šroubovice), bimodální (obsahující kapky a vřetena) a unimodální (čistě vlákné) morfologie ENF pro čtvercové, sinusové a trojúhelníkové průběhy vysokonapět'ové vlny. Kromě toho frekvence tvaru vlny přímo ovlivňuje počet kapek a/nebo vřeten na jednotkovou délku nanovlákná. Čtvercový průběh vysokonapět'ové vlny poskytuje vyšší produktivitu ($23,6 \pm 0,4 \text{ g/h}$) než sinusový ($16,5 \pm 0,3 \text{ g/h}$) a trojúhelníkový průběh ($6,9 \pm 0,2 \text{ g/h}$).

Je zajímavé, že ačkoliv elektrostatická vlákna vznikala v důsledku vysokého elektrického pole, které vytváří ionty, volné elektrony a také UV záření, původní chemická struktura prekurzorového materiálu se nezměnila. Proto byla PCL elektrostatická nanovlákná vrstva (ENM) vystavena plazmovému výboji generovanému v argonu nebo dusíku. Následně byly analyzovány účinky plazmatické úpravy na morfologii ENM, smáčitelnost, povrchové funkční skupiny, velikost krystalitů, krystalinitu, teplotu krystalizace a teplotu tání. Různé PCL ENM byly získány prostřednictvím procesu střídavého elektrostatického zvlákňování za použití 10 % hmotn. F-PCL, FA-PCL a FAA-PCL prekurzorových roztoků. Experimentální výsledky odhalily, že aniž by byla změněna povrchová morfologie PCL ENM, byl kontaktní úhel vody významně snížen ze 136° na přibližně 35° a 42° pro vzorky ošetřené dusíkem a argonovou plazmou, v daném pořadí. Toto zjištění koreluje s podstatným zvýšením polárních kyslíkových a dusíkových funkčních skupin na povrchu nanovláken. Kromě toho se velikost krystalitů a stupeň krystalinity PCL ENM také významně nezměnily provedenými plazmovými úpravami.

Doufám, že tato práce bude inspirovat akademickou a průmyslovou komunitu k výrobě různých polymerních nanovláken v průmyslovém měřítku pomocí techniky střídavého elektrického zvlákňování. Práce je také naznačením jak při průmyslové výrobě PCL ENF prostřednictvím ladění tvaru a/nebo frekvence střídavého vysokonapětového signálu získat různé morfologie PCL ENF. Výsledky plazmatické úpravy odhalily, že povrchové vlastnosti PCL ENM by mohly být pozitivně ovlivněny při zachování jejich prospěšných objemových vlastností. Tím se tyto plazmou modifikované ENM stávají vynikajícími kandidáty v mnoha biomedicínských aplikacích a aplikacích pro tkáňové inženýrství.

Keywords: AC electrospinning; Tvar vlny; Frekvence; Nanovlákná; Morfologie; Produktivita; Polykaprolakton; Benigní rozpouštědla; Plazmatická úprava.

Dedication

I dedicate this thesis to my beloved grandfather Mr. Rudhraiya,
grandmother Mrs. Nagarathinammal, my father Mr. Sivan and mother Mrs. Santhi.

Acknowledgements

First and foremost, I express my sincerest gratitude to my supervisor Professor Lukas, who accepted me as one of his Ph.D students. During my Ph.D studies, he has shown a remarkable interest in my work. He gave me the opportunity and freedom to expand my scientific background, and develop my research on the topics which I found fascinating. He always provided instructive comments and evaluations at every stage of my research work and thesis development. Many thanks for showing constant interest in my research work and providing me with whatever a young researcher requires. I greatly admire his outstanding availability as well as generosity in all circumstances.

The Faculty of Textile engineering, Technical University of Liberec, hosted me as a PhD student and therefore, I also would like to express my gratitude to the Dean of the Faculty of Textile engineering Dr. Vladimir Bajzik, Vice Dean Dr. Iva Mertova, former Dean Dr. Jana Drasarova, and former Vice Dean Dr. Gabriela Krupincova. I would like to extend my gratitude to Dr. Jiri Chvojka, the Head of the Department of nonwoven and nanofibrous materials, and Prof. Oldrich Jirsak. A profound thankfulness goes to Mrs. Bohumila Keilova and Mrs. Hana Musilova for their assistance and support.

I would like to thank Dr. Petr Mikes, Dr. Jan Valtera, Mr. Tomas Janousek, and Dr. Vit Novotny, who helped me with the experimental parts related to AC electrospinning and chromatography. I also thank Dr. Lubos Behalek for DSC studies.

I would like to show my appreciation towards Prof. Rino Morent and Prof. Nathalie Degeyter at Ghent University for hosting me in their lab as an intern. The opportunity they provided me was quite productive and turned out to be a whole sub-chapter in my thesis.

I would like to thank my colleagues and co-authors at the Department of Nonwovens and nanofibrous materials and the Department of Bioengineering for the kind and open atmosphere during my PhD. Their assistance and support has made every working day enjoyable rather than a job. I want to particularly mention and thank Dr. Eva Kostakova, Dr. Veera Jencova, Dr. Veera Hedvicakova, and Ing. Sarka Hauzerova.

Also, It would not be right for me to take complete credit for this dissertation as it would not have been possible without the support of my wife Divya, and for this, I am forever indebted to her.

The sacrifices that my parents made for me while I was working on my PhD cannot be adequately expressed in words. Nevertheless, I want to thank them for teaching me how to work hard with persistence and self-respect. They unconditionally loved and believed in me, regardless of what I did professionally. I am extremely fortunate to have such wonderful and caring parents. I thank my family members Vishalakshi, Selvaraj, Manjula, Murugesan, Mahalakshmi, Madheswaran, Maheswari, Raja, Anitha, Nivetha, Udayakumar, Gopinath, Kabilesh, Kishorenath, Priyanka, Sasikala, Dineshkumar, Rubha and Vignesh.

The statement made by Albert Einstein that “The more I study science, the more I believe in God” is absolutely correct. I want to thank God for giving me the willpower to accomplish my objectives and for encircling me with supportive individuals.

Contents

List of Figures	xii
List of Tables	xvi
List of Abbreviations	xviii
List of Symbols	xx
1 Introduction	1
1.1 Purpose and aim of the thesis	4
1.2 Structure and research strategy of this thesis	8
2 State of the Art in Literature	10
2.1 Nanofiber fabrication methods	10
2.2 Historical development of electrospinning	12
2.3 Electrospinning setups	14
2.4 Creation of electrospun in DC vs AC electric field	14
2.4.1 Formation of the Taylor cone	15
2.4.2 Stretching of the charged jet	22
2.4.3 Thinning or bending instability of the charged jet	24
2.4.4 Solidification and subsequent fiber deposition	26
2.5 Materials used in AC electrospinning	28
2.5.1 AC electrospinnability of various solutions	28
2.6 Surface plasma treatment	35
3 Materials and Methodology	38
3.1 Materials	38
3.2 Methodology	38
3.2.1 Solubility parameter: Theory	39
3.2.2 Precursor solution preparation	40
3.2.3 Analysis of viscosity and surface tension of the various PCL solutions	41

3.2.4	Analysis of PCL stability in various solvents	42
3.2.5	AC electrospinning	43
3.2.6	AC high-voltage signal generator and amplifier connections to the spinneret	44
3.2.7	Dielectric barrier discharge (DBD) reactor	45
3.2.8	Productivity analysis	47
3.2.9	Scanning electron microscopy	47
3.2.10	Analysis of pore size and porosity	47
3.2.11	Analysis of number of beads and/or spindles	49
3.2.12	Water contact angle analysis	50
3.2.13	X-ray photoelectron spectroscopy	51
3.2.14	X-Ray Diffraction (XRD) characterization of the ENMs	51
3.2.15	Differential scanning calorimetry analysis	52
3.2.16	Fourier-transform infrared spectroscopy analysis	52
3.2.17	Sterilization	52
3.2.18	Cytotoxicity	53
3.2.19	In vitro experiment	54
3.2.20	Statistical analysis	54
4	Obtained results	56
4.1	Impact of AC high voltage and solvent systems on the spinnability of PCL electrospun nanofibers	57
4.1.1	Experimental conditions	57
4.1.2	Analysis of polymer–solvent interactions	58
4.1.3	Effects of the solvent system on the stability of PCL	59
4.1.4	Effects of solvent system on the surface tension and viscosity of the solution	61
4.1.5	AC spinnability of the polymeric solutions	64
4.1.6	Productivity of PCL electrospun nanofibers	68
4.1.7	Principal component analysis of AC spinnability of PCL	70
4.1.8	Cytotoxicity and in vitro analysis of PCL ENS	71
4.2	The impacts of various AC high-voltage signal waveforms and frequencies on the spinnability and productivity of PCL nanofibers	75
4.2.1	Experimental conditions	76
4.2.2	Effects of the AC high-voltage signal waveform and frequency on the electrospinnability of PCL	76
4.2.3	Impacts of the AC high-voltage signal waveform and frequency on the electrospun fibers morphology	78

4.2.4	Effects of the AC high-voltage signal waveform and frequency on productivity	84
4.2.5	Effects of the AC high-voltage signal waveform and frequency on the chemical structure of PCL	85
4.3	Plasma treatment effects on the bulk properties of PCL nanofibrous mats .	87
4.3.1	Experimental conditions	87
4.3.2	Water contact angle (WCA) analysis	88
4.3.3	Surface morphological analysis of pristine and plasma-treated ENMs	90
4.3.4	Surface chemical composition analysis	91
4.3.5	Crystal size and crystallinity analysis of PCL ENMs	95
5	Conclusions	100
5.1	Significant output from the research and future work	103
A	First Appendix	104
	References	107
B	Research outputs	123
B.1	List of Publications	123
B.1.1	The Web of Science or Scopus indexed Conference publications . . .	124
B.1.2	Conferences	125

List of Figures

1.1	The number of published scientific articles related to electrospinning per year	5
2.1	Various nanofiber fabrication strategies and their strengths and weaknesses	11
2.2	History of the electrospinning technology	12
2.3	Various electrospinning setups in terms of high-voltage connection	14
2.4	Polymeric jet under the various AC high-voltage waveform and frequencies.	18
2.5	Relationship between inter-jet distance and the critical field strength; as well as dimensionless wavelength and electrospinning number	20
2.6	Stretching of the charged jet in the DC and AC electric field.	24
2.7	Fibrous plume under the lower and higher frequency of AC high voltage . .	26
2.8	AC electrospun mats and electrospun fibrous yarn	29
2.9	Fabrication of various composite nanofibrous yarns.	31
2.10	Surface energy of PCL AC spun nanofibers and fabrication of ribbon shaped electrospun fibers.	33
2.11	Productivity of various bubble spinning methods.	34

2.12	Hydrophobic recovery as a function of aging time and in vitro analysis of plasma-treated electrospun nanofibers	36
3.1	Schematic representation of AC electrospinning and picture of the nanofibrous plume	43
3.2	Schematic illustration of the AC high-voltage signal generator (Won AG 1022) and amplifier (TREK) connected to the spinneret.	45
3.3	Schematic and pictorial representation of the DBD reactor.	46
3.4	Model of cross-sectional image of nanofibers for analyzing the pore size and porosity of ENS.	48
3.5	Model of a probe arrangement for the estimation of fiber/line intercepts.	50
4.1	3D representation of the Hansen solubility parameter and the solubility sphere	58
4.2	Light microscope images of FAA-PCL thermoreversible gel	60
4.3	GPC chromatograms of F-PCL, FA-PCL and FAA-PCL overtime	61
4.4	The surface tension for various precursor solutions corresponding to precursor concentration.	62
4.5	The dynamic viscosity of FAA-PCL, FA-PCL, and F-PCL precursor solutions corresponding to precursor concentration.	63
4.6	SEM micrographs of various PCL ENS as a function of the various solvent systems	65
4.7	Electrospun nanofiber diameter as a function of the polymer concentration and applied voltage	67
4.8	Productivity of various PCL electrospun nanofibers	69

4.9	Principal component analysis of AC spinnability of PCL	70
4.10	Cytotoxicity analysis of various ENS	72
4.11	In vitro analysis of various PCL ENS	73
4.12	Photographs of the nanofibrous plume with respect to various waveforms and frequency of AC high-voltage signal	77
4.13	SEM images of the PCL ENF as a function of the various waveforms and frequencies	79
4.14	Number beads and/or spindles as the function of the various waveforms and frequencies	81
4.15	Fiber diameter as a function of the various waveforms and frequencies of the AC high-voltage signal	83
4.16	Productivity of the PCL ENF as a function of the various waveforms and frequencies.	84
4.17	FTIR spectra of PCL ENF as a function of the various waveforms and frequencies.	85
4.18	WCA of PCL nanofibrous mats	89
4.19	SEM images of pristine and plasma treated PCL ENMs	90
4.20	XPS survey spectra of pristine and plasma-treated PCL ENMs.	92
4.21	XPS high-resolution C1s peaks of pristine and plasma treated PCL ENMs	93
4.22	Relative concentrations of the carbon-containing functional groups on un- treated and plasma-treated PCL ENMs.	94
4.23	XRD patterns of untreated and plasma-treated PCL ENMs.	95

4.24	FTIR spectra of pristine and plasma-treated PCL ENMs.	97
4.25	DSC curves of 1 st heating and cooling scans for untreated and plasma-treated PCL ENMs.	98
A.1	Viscosity of various PCL solution as a function of storage condition and time.	104
A.2	Pore size distribution probability.	105
A.3	SEM images of PCL ENF as a function of the square waveform's various frequencies.	105
A.4	A linear relationship between χ_c and X_c	106

List of Tables

2.1	DC vs AC electrospinning technology	16
3.1	Summary of prepared polymeric solutions	40
3.2	The experimental parameters of DBD plasma treatment	46
3.3	Stereological probe and the sampling area	50
3.4	Eigen values of the principal component analysis (PCA)	55
4.1	Various precursor solution and AC electrospinning processing parameters.	57
4.2	Solution properties	59
4.3	Vapour pressure and diffusion coefficient of various solvents	68
4.4	AC electrospinning processing parameters.	76
4.5	Various spinning solutions and AC electrospinning processing parameters	87
4.6	Plasma treatment parameters	88
4.7	The surface atomic composition of pristine and plasma treated electrospun fibers	91
4.8	The thermal and crystalline properties of the electrospun nanofibers	96

List of Abbreviations

AC	Alternating current
BSA	Bovine serum albumin
CED	Cohesive energy density
DBD	Dielectric barrier discharges
DC	Direct current
DCM	Dichloromethane
DMF	Dimethylformamide
DMEM	Dulbecco's modified Eagle medium
DSC	Differential scanning calorimetry
ECM	Extracellular matrix
ENF	Electrospun nanofiber
ENM	Electrospun nanofibrous mat
ENS	Electrospun nanofibrous scaffold
F	Formic acid
FA	Formic acid/acetic acid
FAA	Formic acid/acetic acid/acetone
FTIR	Fourier-transform infrared spectroscopy
GPC	Gel permeation chromatography

HPC	Hydroxypropyl cellulose
MTT	3-(4,5-Dimethylthiazol-2-yl)-2,5-Diphenyltetrazolium Bromide
PA	Poly-amide
PCL	Poly-caprolactone
PET	polyethylene terephthalate
PEO	Polyethylene oxide
PLA	Poly-lactic acid
PLGA	Poly-lactic-co-glycolic acid
PU	Poly-urethane
PVB	Poly-vinylbutyral
PVP	Poly-vinylpyrrolidone
RED	Relative energy dispersion
SEM	Scanning electron microscope
THF	Tetrahydrofuran
TiO₂	Titanium dioxide
WCA	Water contact angle
XRD	X-Ray Diffraction
XPS	X-ray photoelectron spectroscopy

List of Symbols

a	Parameter of the Mathieu equation
a_c	Capillary length
A	Amplitude
D	Crystallite size
D_{ac}	distance between AC spinneret to virtual collector
D_{dc}	distance between DC spinneret to collector
E_0	Electric field strength
E_c	Critical electric field strength
f	Frequency
g	Gravitational acceleration
k	Wavenumber
k_c	Critical wavenumber
K	Dimensionless wavenumber
L	Length of the jet's straight segment
L_A	$((\text{number of fiber intersects})/(\text{total length of the line})) \times \pi/2$
N	Number of fiber cross-sections
N_a	Number of points falling exclusively on the nanofiber cross-sections
N_c	Total number of points on the surface area of the sampling image

N_A	Number of beads and (or) spindles/area of the specimen
N_L	Number of beads and/or spindles per unitary fiber length
N_S	Numerical area density of the nanofiber cross-sections
V_m	Molar volume
P	Pressure
P_c	Capillary pressure
P_e	Electric pressure
P_h	Hydrostatic pressure
q	Parameter of the Mathieu equation
r	Characteristic radius of the curvature of the liquid surface
r_p	Probability density of pore radius
r_s	Mean value of pore radius
R	Universal gas constant
S	Sampling area
t	Time
U	Internal energy of system
V_c	Critical voltage
V_d	Velocity of the charge in the jet's straight segment
X_c	Crystallinity degree
β	Full-width at half maximum of the diffraction peak
γ	Surface tension
Γ	Electrospinning number
δ_d	Dispersion force (Solubility parameter)
δ_h	Hydrogen-bonding force (Solubility parameter)

δ_p	Polar force (Solubility parameter)
δ_t	Total solubility parameter
δ_1	Total solubility parameter of the polymer
δ_2	Total solubility parameter of the solvent
ΔH_{vap}	Enthalpy of vaporization
ΔH_{m1}	Melting enthalpy measured in the 1 st heating run
ΔH_{m1}^0	Melting enthalpy of perfect PCL crystals
ε	Electric permittivity
ξ	Wave's vertical displacement along the z-axis
θ	The Bragg angle
λ	Wavelength
Λ	Dimensionless wavelength
ρ	Density of fluid
τ_e	Electric charge relaxation time
ω	Angular frequency
Ω	Dimensionless angular frequency

Chapter 1

Introduction

The discovery of 34,000 years old textile-based fibrous imprints from the paleolithic site of Nové Pavlovice in the Czech Republic makes them one of the oldest man-made fibrous imprints [1, 2]. From this evidence, it can be deduced that this region of Europe was prosperous in textiles during the periods of the Upper Paleolithic as well. Interestingly, this has been continued even in the early stage of the third millennium, the polymeric electrospun nanofibers's fabrication using the electrospinning technology has emerged in the same region, which is known as the NanospiderTM (Elmarco, Czech Republic) and collectorless alternating current (AC) electrospinning (Technical University of Liberec, Czech Republic) [3–7].

Electrospinning is related to the electrohydrodynamic phenomenon in which electrified polymeric solution or melt is stretched into a continuous jet and, subsequently, experiences various electrohydrodynamic instabilities (stretching and bending or whipping instabilities) within an electric field, which results in the formation of the electrospun fibers [8, 9]. In the case of solution electrospinning, rapid evaporation of solvents from the jet occurs during its movements toward the counter electrode resulting in solidified electrospun fibers. In the polymeric melt, solidification occurs through heat transfer between the molten jet and ambient air [10].

Electrospinning is one of the most adopted nanofiber fabrication techniques than the drawing–processing, solvent casting, template–assisted synthesis, self–assembly, and phase separation; because it enables the mass production of continuous electrospun fibrous material with unique properties from the polymers or polymeric composites [11]. Electrospun

materials have grown in popularity in various fields, including biomedicine, energy, food, agriculture, textiles, liquid filtration, air filtration, and environmental applications, to mention but a few, attributed to their superior properties such as larger surface–area–to–volume ratio, potential functionalization, interconnected porosity, desirable flexibility for cellular activity, and diverse mechanical properties [11–15].

According to the data announced by “Business Communication Company, Inc. Research” (BCC) the global market for nanofiber products was worth \$80.7 million in 2009. Subsequently, it reached \$2.2 billion in 2021 and is expected to surpass \$6.7 billion by 2026 (report code: NANO43F, April 2022). To meet the international market demand, various research groups in academia and industrial sectors have been working until now. In 2005, the notable invention of NanospiderTM (Elmarco, Czech Republic) by Jirsak’s group (Technical University of Liberec, Czech Republic) is the first technology to enable the industrial–scale production of electrospun fibers, which is also one of the highest electrospun nanofibers productive machines so far now [3]. For industrial–scale production of electrospun materials, several companies such as Asahi Kasei Fibers, Wetlaid nonwoven fabrics, NnF CERAM (Pardam Nano4fibers), Applied Sciences, Donaldson, Dupont, and eSpin Technologies also exist in the global market [11]. The evolution of electrospinning from a single capillary needle to multi–nozzle systems coaxial, uniaxial, and free–surface spinneret accelerated the productivity of electrospun nanofibers to an industrial scale [16, 17]. Although the electrospinning setup consists of a power source, spinneret, and collector, this evolution was profoundly focused only on redesigning spinnerets and/or collectors but not significantly on the high–voltage power source [18].

A significant step in the evolutionary process of electrospinning was recently taken by Lukas’s group (Technical University of Liberec), who, inspired by Kessick *et al.* utilized AC high–voltage as a power source for electrospinning [19]. The term AC electrospinning was started popularized by Lukas and his co–workers in 2014, who published various articles and patents on AC electrospinning technology [4–7, 20–24]. Furthermore, it also has the potential to utilize various types of spinnerets, including disc, wire, and multi–free–surface spinnerets, for fabricating electrospun materials.

Unlike DC high voltage, the polarity of the AC high voltage is a function of time. Therefore, the rate of polarity changes (or frequency) can be manipulated via various waveforms (sine, square, triangle, etc.,) [25–28]. This unique feature of AC provides better control over the delivery of the electric charges to the spinning solution as well as the following electrohydrodynamic instabilities. According to previous studies, the waveform and/or

applied frequency are able to affect the electrification of the liquid, jet initiation and termination, the length of the charged segments, the whipping instability, and the formation of a virtual collector [19, 23, 26, 29]. The time-dependent polarity of the AC high voltage facilitates the formation of a compact fibrous plume structure since it simultaneously contains positive and negatively charged segments. Consequently, charges within the nanofibrous plume are neutralized, and a dense thicker fibrous plume emerges a few centimeters (approximately 3 cm) away from the spinneret via ionic wind [23]. Since AC electrospinning does not require an electrically active collector which serves for the facile fabrication of multi-dimensional nanofibrous structures over common DC electrospinning, including composite nanofibrous yarns (electrospun fibers wounded around the classic yarn) [21, 24], bulky electrospun fibrous scaffolds [22, 30, 31], and drug delivery systems [25]. Pokorny *et.al.* compared the spinnability and productivity of PVB nanofibers by using DC and AC high voltage [23]. They reported that a six times higher throughput of PVB electrospun nanofiber was achieved by using AC (180 mL/h) compared to using the DC voltage (30 mL/h) because of the greater degree of hydrodynamic instability of the polymer liquid under the AC field. In another study, corona AC electrospinning resulted in a ten-fold higher throughput of polyvinylpyrrolidone nanofibers than corona DC electrospinning [32].

Since nanofibers are believed to be excellent attorneys for the native extracellular matrix (ECM), their usage as scaffolds in tissue engineering began to increase [33]. A large variety of aliphatic poly(hydroxy ester) electrospun fibers, including polycaprolactone (PCL), polylactic acid (PLA), polylactic-co-glycolic acid (PLGA) have been intensively used as a biomaterial in biomedical fields. Among them, PCL electrospun fibers have been regularly fabricated using electrospinning technology for applications of tissue regeneration, drug delivery, and wound dressing. This is particularly due to its FDA hallmark, tunable spinnability in terms of different morphologies using varieties of solvents and/or blends of solvents, slow degradation rate, and superior mechanical properties [34]. To fabricate the PCL nanofibers, highly toxic volatile organic solvents and/or solvent systems such as chloroform, dimethylformamide (DMF), tetrahydrofuran (THF), dichloromethane (DCM), chloroform/methanol, DMF/THF as well as DMF/chloroform have been traditionally used [35]. These organic solvents are not only a source of danger to the operator and environment but also to end-users in the form of residual solvents [36].

Removal of residual solvents from the electrospun nanofiber is usually tricky. In the case of biodegradable implants like PCL, the residual solvents could be released when it degrades. Subsequently, it could cause toxicity to the surrounding cells when toxic solvents are used. At the same time, PCL degradation byproducts are either eliminated

directly by the kidney or metabolized via the tricarboxylic acid cycle [37]. According to the European Pharmacopoeia, all of these solvents are Class 2, and their utilization should be limited in the fabrication process due to their inherent toxicity [38].

Although PCL has been widely used in the biomedical field, its inherent hydrophobicity restricts initial cell interactions, thus limiting the range of applications in the field of tissue engineering [39]. Blending hydrophilic polymers with PCL spinning solution is currently one of the widely used methods to improve the hydrophilicity of PCL nanofibers. However, it significantly leads to a deterioration of mechanical properties possessed by blended polymers. Although this method improves the wettability, it profoundly impacts the bulk properties of the resultant PCL electrospun nanofiber (morphology, crystallinity, and mechanical properties) [40]. As an alternative to blending, surface modification technologies can be employed to achieve the desired positive cellular interactions on the surface of the PCL electrospun nanofibers. Non-thermal plasma treatment is utilized to improve the wettability of PCL ESMs. This strategy has been widely used and is a versatile, cost-effective, and environmentally benign (solvents are not used) mild surface modification approach. The depth of plasma treatment (less than 5 nm) is, in most cases, limited to the first few surface layers of the electrospun fibers [41, 42].

1.1 Purpose and aim of the thesis

There are many studies available regarding the redesign or modification of electrospinning setups (spinneret and/or collector), spinnability of various polymers-based materials, and the resultant electrospun fibers's physicochemical, mechanical as well as biological properties. All the studies mentioned above have been conducted on common DC electrospinning. Although AC electrospinning technology has some advantages over common DC electrospinning (i.e., better control over the electrification of the liquid via various waveforms and frequencies of the AC high voltage signal, formation of a compact fibrous plume, and the electrospun fibers can be collected on the electrically neutral material), it is inadequately explored in the realm of electrospinning. However, AC high voltage is frequently pronounced in the electro spraying field. This thesis desires to show that AC high voltage also has the potential to produce electrospun nanofibers in high throughput. As presented in Fig. 1.1, since 2000, the number of annual publications related to electrospinning has grown from 9 to 3892 articles (total: 35600); on the other hand, very few studies have been conducted regarding AC electrospinning.

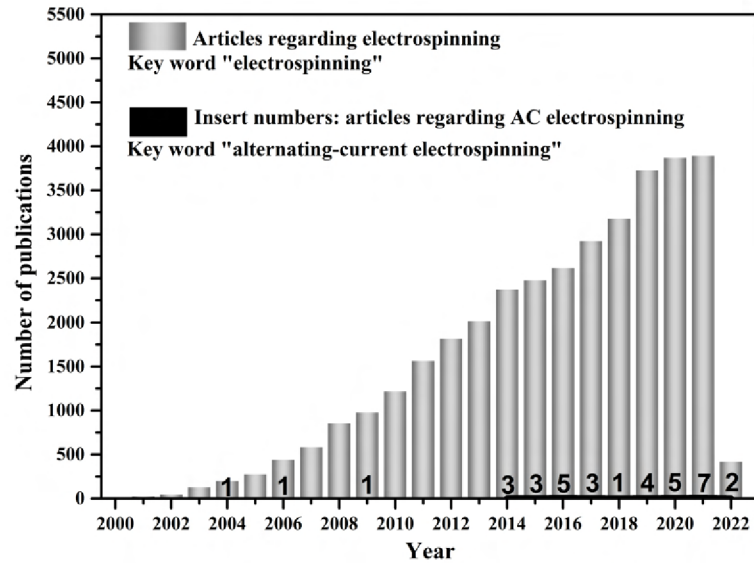


Figure 1.1: According to the Web of Science (WoS), the number of published scientific articles related to electrospinning per year (keyword “electrospinning”, the search category “title” and the period “2000 to February 2022”). The inserted numbers are the AC electrospinning related publications (keyword “alternating-current electrospinning”, the search category “title” and the period “2000 to February 2022”).

Therefore, the objectives of this work are focused on the following item.

❶ **Investigate the impact of AC high-voltage and solvent on PCL’s spinnability.**

Electrospinning technology employs DC high-voltage to produce electrospun fibers from the polymeric liquid or melt. However, until now, the impact of AC high-voltage on the spinnability of polymers remains inadequately explored.

A few specific problems of this work or objective are,

- Unlike DC electrospinning, the selection of desirable solvents for AC electrospinning of PCL is not yet optimized. Furthermore, commonly used solvents for DC electrospinning of PCL are highly toxic volatile organic solvents (Class 2). Also, the AC spinning of PCL was impaired when these organic solvents were used. Hence, the solvent or solvent system, which has low toxic potential (Class 3) should be identified for studying the AC spinnability of PCL [38].

- **Idea or hypothesis 1:** The carboxylic acids could be used as a solvent system for improving the AC spinnability of PCL rather than common toxic volatile organic solvents.

Interestingly, this hypothesis brought up another new ternary solvent system since a

highly acetic environment cleaves PCL's ester bonds through an acid-catalyzed cleavage reaction. This new ternary solvent system improved the PCL's stability over time in the aqueous acetic environment. Also, it resulted in better AC spinnability than when using pure carboxylic acid.

The validation of this hypothesis is presented in sub-chapter 4.1. Herein, the effects of various less toxic potential solvents and AC high-voltage (25 and 32 kV) on the spinnability, morphology, and productivity of PCL ENMs are studied. Besides this, cellular activity on various PCL ENS is also evaluated.

② **Investigate the impact of various AC high-voltage signal waveforms and frequencies on the spinnability and productivity of PCL.**

For the first time, this study describes the application of a new technological parameter in the alternating-current (AC) electrospinning process for enhancing the electrospinnability and productivity of PCL ENF. High-voltage AC is influenced via changes in both the waveform and the frequency; however, the overall contribution to PCL electrospinnability remains unclear.

□ **Idea or hypothesis 2:** The waveform and/or applied frequency of AC high-voltage signal are able to affect the electrification of the liquid, jet initiation and termination, the length of the charged segments, the whipping instability, and the formation of a virtual collector. Thus the waveform and frequency of AC high-voltage signal can be used as new technological parameters for controlling the AC spinnability of polymers. This study hypothesizes that the electrospinnability, morphology, diameter, and productivity of PCL ENF are dependent on both the waveform and the frequency of the AC high-voltage signal.

The validation of this hypothesis is presented in sub-chapter 4.2. Herein, the impacts of various AC high-voltage signal's waveforms and frequencies on the spinnability, morphology, and productivity of PCL ENFs are studied.

③ **Analysis of the plasma treatment effects on bulk properties of PCL.**

Generally, plasma treatments are considered to be mild surface treatments whose depth (a few nanometers) is normally less than the diameter of the electrospun fibers [41, 42]. In addition, a large number of reports have been published dealing with the

plasma treatment of PCL ENMs, and most of these studies are mainly focused on tissue engineering applications as scaffolds. To this date, available studies discuss the effects of plasma treatment on PCL ENMs by means of morphology, wettability, and surface chemistry. However, the degree of crystallinity is one of the key parameters controlling the degradation and mechanical properties of semi-crystalline polymers like PCL [43].

- **Idea or hypothesis 3:** In most cases, there are no impacts of plasma treatment on the bulk properties (morphology, crystallinity degree, crystal size, melting temperature, and crystallization temperature) of PCL electrospun nanofibers.

The validation of this hypothesis is presented in sub-chapter 4.3. Herein, various plasma surface treatments effect on the bulk properties of PCL nanofiber are studied.

1.2 Structure and research strategy of this thesis

As evident from the literature, the AC spinnability of polymers is not yet well explored. In addition, only a limited number of studies are available regarding the plasma surface treatment's impacts on the electrospun nanofiber's bulk properties. Therefore, this PhD dissertation explores the AC spinnability of PCL nanofibers as a function of high-voltage and solvent systems and the plasma treatment effects on their bulk properties.

Chapter 2. State of the art in literature: This chapter introduces various nanofiber fabrication strategies, and special attention is given to electrospinning technology, followed by a historical and theoretical overview of the DC and AC electrospinning techniques. Then the chapter continues to discuss the AC spinnability of various materials and the plasma surface treatments.

Chapter 3. Materials and Methods: This chapter is dedicated to the materials, methods, and experimental setups used to achieve the objectives of the thesis. Solvent selection method (the Hildebrand and Hansen solubility theory), the solution characterization methods (viscometer, tensiometer, and GPC), the electrospun fabrication method (AC electrospinning), plasma treatment (DBD reactor), the electrospun morphological analysis (SEM and stereological method), productivity analysis (gravimetric method), physicochemical analysis (water contact angle, XPS, XRD, DSC, FTIR, sterilization method (ethylene oxide), cytotoxicity (MTT assay) and in vitro analysis (MTT assay and fluorescent microscope) of electrospun PCL fibers, and finally, the statistical methods used are described.

Chapter 4. Obtained results: This chapter is dedicated to experimental findings, which is further divided into three sub-experimental parts (sub-chapters 4.1, 4.2, and 4.3). In the first sub-experimental part (sub-chapter 4.1), the better solvent system for PCL to produce the AC electrospun nanofibers is identified. Subsequently, the identified solvent system and AC high-voltage effects on AC spinnability of PCL are analyzed. Furthermore, electrospun fiber's surface morphology, pore, porosity, productivity, biocompatibility, and in vitro analysis results have been discussed. Secondly (sub-chapter 4.2), the impacts of AC high-voltage waveform and frequency on the AC electrospinnability of PCL are also explained. Finally (sub-chapter 4.3), to improve the hydrophilicity of PCL electrospun nanofibers, a DBD plasma treatment was performed. Furthermore, plasma treatment effects on bulk properties (morphology, wettability, crystallinity degree, melting, and crystallization temperature) of PCL electrospun nanofibers are discussed.

Chapter 5. Conclusion: This chapter gives an overall conclusion on the conducted work and an outlook on future considerations. The thesis is completed with two appendices. First appendix is dedicated to supporting images for sub-chapter 4, while the list of publications related to the thesis is presented in the next appendix.

Chapter 2

State of the Art in Literature

This chapter introduces various nanofiber fabrication strategies; however, particular attention is given to electrospinning technology. In addition, historical and theoretical overviews of the DC and AC electrospinning techniques are also discussed. Then the chapter continues to discuss the AC spinnability of various materials and the plasma surface treatments.

2.1 Nanofiber fabrication methods

The notation of “There’s plenty of room at the bottom” by Richard Feynman had sparked tremendous attention and development on nano sized materials. Today, we can see that this is definitively in the case of nanofibers, which are found to resolve several challenging issues in various fields, including bio–medicine (scaffolds, drug delivery, and sensors), environment (air/water filtration), energy (storage and harvesting), nanofiber–based yarn (suture). This is attributed to their unique fabrication methods and superior properties (i.e., larger surface–area–to–volume ratio, potential functionalization, interconnected porosity, desirable flexibility for cellular activity, and diverse mechanical properties) [11–15]. Even though there are various nanomaterials like nanoparticles, nanodots, nanoclays, nanosheets, nanoflowers, nanotubes, and etc., among these, nanofibers have been much–explored due to their market demands and unique fabrication methods [11].

As shown in Fig. 2.1, based on the physical and chemical routes, various strategies have been created and developed for nanofiber fabrication. However, the chemical route–

based techniques (hydrothermal synthesis, chemical vapor deposition, template synthesis, and phase separation) are time-consuming, capable of producing limited fiber length (low length to width aspect ratio), and result in low productivity. On the other hand, comparatively, most of the physical route-based techniques (electrospinning, physical vapor deposition, centrifugal spinning, and solution blowing) offer distinct advantages over chemical routes based methods as it capable of fabricating the continuous nanofibers at a higher production rate.

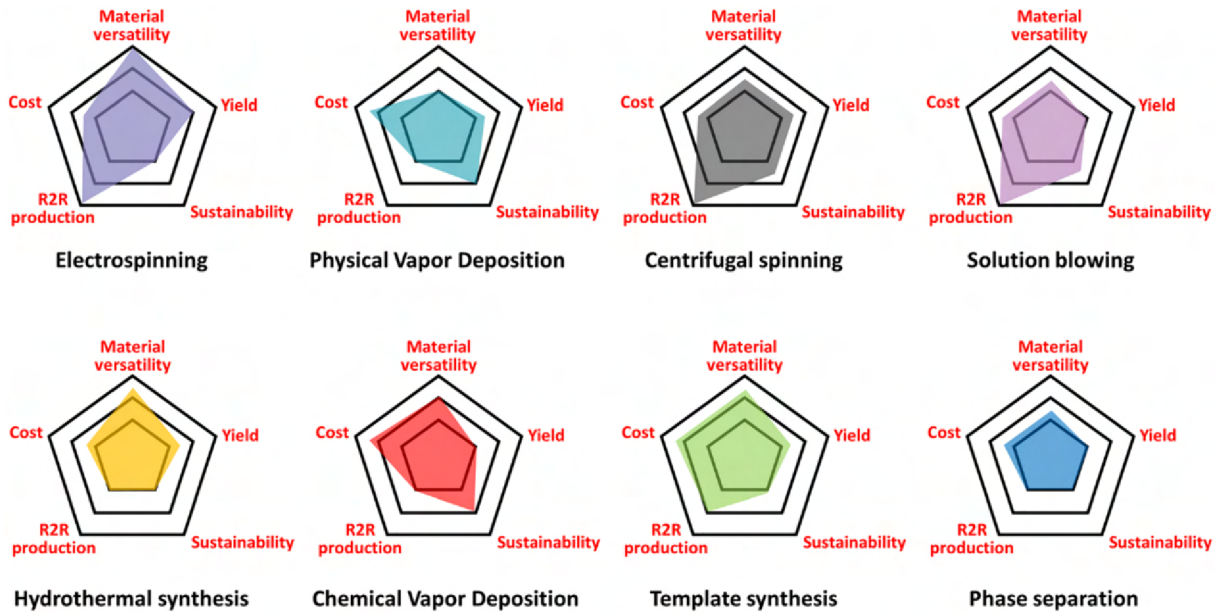


Figure 2.1: Various nanofiber fabrication strategies and their strengths and weaknesses [11].

As shown in Fig. 2.1, in terms of roll to production, the electrospinning, centrifugal spinning and solution blowing resulting better position among other nanofiber fabrication techniques. However, electrospinning reflects the utmost versatility to fabricate nanofibers from various materials such as polymers, ceramics and composites at a higher yield. The electrospinning techniques suffers mainly in terms of sustainability due to the usage of volatile toxic organic solvents, however, it can be addressed by using green solvents. With nanotechnology playing a vital role in advanced technologies, electrospinning has gained enormous attention within both the academia and industrial communities, especially for its capability to synthesize nanofibers at a large scale. Owing to their features, ENFs are actively adopted to resolve several challenging issues in various areas, including bio-medicine, industrial (air/water filtration), energy (storage, harvesting, conversion), environmental applications, agriculture, space exploration, and nanofiber-based yarns.

2.2 Historical development of electrospinning

The technological advancement of electrospinning for fabricating the electrospun nanofiber is not instantaneously happened. However, the evolution of electrospinning is made possible with the help of scientists from various parts of the world (Fig. 2.2). Thus, it is worth mentioning here a timeline for the evolution of electrospinning from its inception to the current advancements.

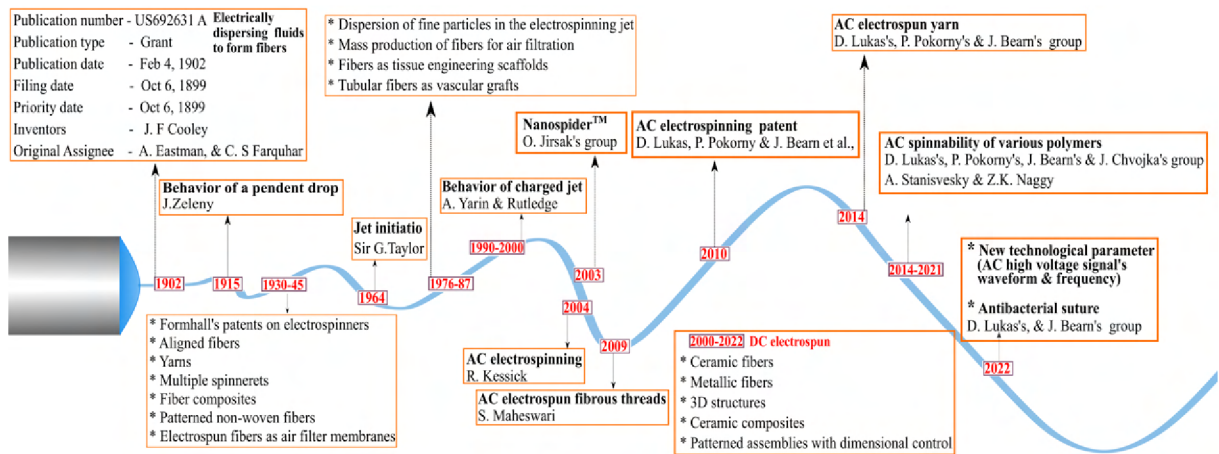


Figure 2.2: *History of the electrospinning technology.*

During the years 1600 to 1700, the concept of electrospinning or electrostatic spinning was conceived by William Gilbert and Stephen Gray, which they observed the formation of a cone-shaped water droplet in the presence of an electric field and electrohydrodynamic atomization of water droplets, respectively. The subsequent investigation about the behavior of charged liquid jets stability in 1882 by Rayleigh, who theoretically estimated the maximum amount of charges that a liquid droplet could carry before liquid jets would be ejected from the free surface [44]. In 1887, Charles Boys reported that electrospun fibers could be produced from a viscoelastic liquid when it moved to the edge of the electrified object [45]. Currently, this invention is known as electrospinning, which opens the door to fabricating ultra thin electrospun fibers with a diameter ranging from tens of nanometers to a thousand nanometers [46].

In 1902, the earliest patents on electrospinning devices were filed by John Francis Cooley and William Morton, which described the prototype of the electrospinning setup for electrospun material fabrication [47, 48]. In 1914, Zeleny established a mathematical model to understand the impact of the applied voltage on the liquid droplet at the tip of the metal capillary [49]. Afterward, Anton Formhals filed his first patent on electrospinning

in 1934, and he filed at least 20 patents between 1934 to 1944 [50]. In 1938, the Soviet Union used electrospun nanofibers for the first time to create “Petryanov filters”, which were air filters designed to capture aerosol particles. This work resulted in the opening of a factory in Tver in 1939 that produced smoke filters with electrospun-based nanofibrous membranes as gas masks. Thus, during this period, electrospinning technology started moving from the lab towards the commercial industries for producing textile yarns. Twenty years later, between 1964 to 1969, the physicist Geoffrey Taylor established the theoretical formulation of electrospinning and modeled the change of a polymer solution’s spherical to conical shape under the influence of an electric field, currently known as Taylor cone [51]. Afterward, in the early 1980s, Donaldson Co. Inc. in the United States started to produce and sell nanofibrous filters for air filtration. The first industrial-level fabrication of nanofibers using needleless technology was invented by Prof. Jirsak under the brand name NanospiderTM from the Technical University of Liberec. This technology is further developed by the Czech company Elmarco, Liberec.

The term “electrospinning” was started popularizing in the early 1990s by several research groups, mainly led by Reneker and Rutledge [8, 52, 53]. They produced various electrospun materials using different organic polymers. Since then and until now, electrospinning has been the method of choice for producing the continuous electrospun fibers with diameters down to the nanometers scale in terms of their simple experimental setup, low cost, mass production potential as well as the possibility to tune the morphology, diameter, and functionality.

Likewise, in 2004 Kessick *et al.* introduced AC high-voltage as a power source for electrospinning technology [19]. They showed the possibility of producing electrospun nanofibers as well as electrospun nanofibrous threads for the first time using AC high voltage. After that, Lukas’s group filed a patent on AC electrospinning [4–7]. Subsequently, they published scientific articles about the AC spinnability of various synthetic and natural polymers, including PCL, PVB, PU, PA6, PAN, PVA, gelatin, collagen, and chitosan [21, 23, 30, 54–57]. At the same time, Stanishevsky from U.S [58, 59] and Nagy from Hungary [25, 32] got inspiration from Lukas; subsequently, they started working on AC electrospinning. However, Lukas’s group is well established in this technology in terms of electrospun nanofiber production and, most notably on, fabrication of composite nanofibrous braided yarns. They were successful in the production of planner and bulky electrospun nanofibers as well as nanofibrous-coated composite yarns on the industrial scale by doing considerable variations in the design of spinneret and/or collector.

2.3 Electrospinning setups

The basic setup for typical electrospinning is rather simple, which consists of four essential components, a power source (either DC or AC high-voltage), a solution reservoir (usually, a syringe pump), a spinneret (blunt needle, roller, wire, and plate), and grounded collector (rotating or stationary collector) [3, 16, 18, 60]. During the electrospinning process, the spinning liquid is extruded from the solution reservoir to the spinneret's surface by the syringe pump. This solution forms a pendant droplet as a result of gravity and surface tension. When high-voltage (either DC or AC) is supplied to the pendant droplet, it gradually deforms into the Taylor cone, from where a charged liquid is ejected. The charged jet initially extends in a straight line and then undergoes various bending instabilities (whipping and stretching) followed by rapid solvent evaporation. Consequently, electrospun fibers were deposited on grounded or oppositely charged collector. In the basic electrospinning setup, the spinneret is connected to the high-voltage, while the collector is grounded. A few electrospinning setups in terms of various high voltage connections are shown in Fig. 2.3, such as common electrospinning, oppositely charged spinneret electrospinning setup, spinneret-collector electrospinning setup, and AC electrospinning setup.

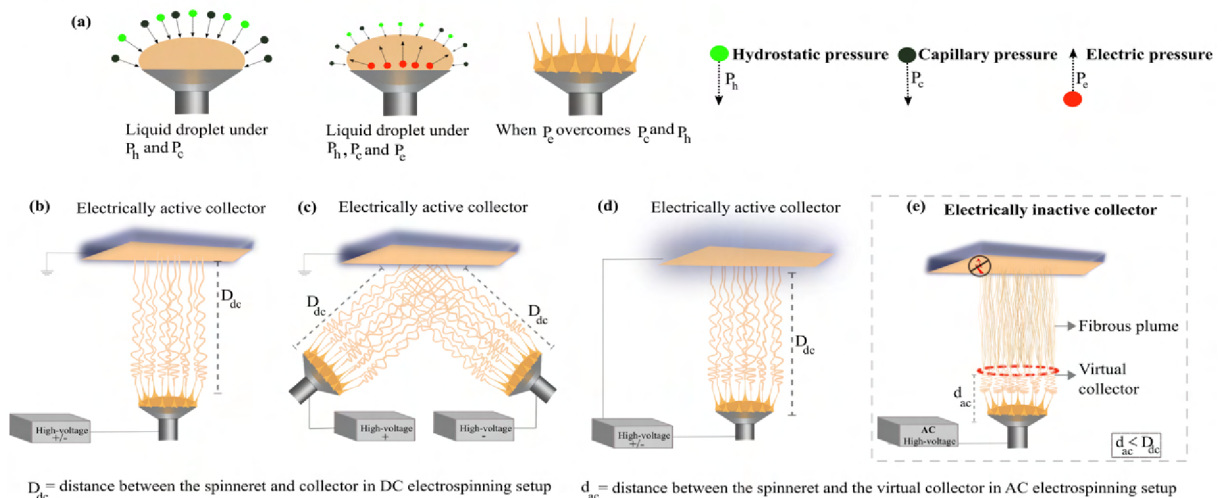


Figure 2.3: (a) Polymeric liquid under various pressures, (b) standard electrospinning setup with high voltage connected through a spinneret, (c) oppositely charged spinneret setup, (d) high-voltage connected to spinneret and collector, and (e) AC electrospinning.

2.4 Creation of electrospun in DC vs AC electric field

The electrospinning is a synergistic process of high-speed nonlinear electrohydrodynamics, complex rheology, and the transport of charge, solvent, mass, and heat within the

liquid jet. The creation of electrospun nanofibers using the electrospinning process can be visualized into four subsequent steps: (i) electrification of the liquid and formation of the Taylor cone, (ii) liquid jet initiation and subsequent extension, (iii) Thinning or bending instability of the charged jet, and (iv) solidification and subsequent fiber deposition. A detailed discussion of these steps is provided in the following subsections. These behaviors of the liquid jets under a DC electric field were studied by Rayleigh, Zeleny, Taylor, Yarin, and Lukas. Conversely, the liquid jet's behavior under the AC electric field is not explored well. For readers' better understandability, the behavior of the liquid jet under DC is first discussed, followed by AC electric field. Furthermore, the difference between DC and AC electrospinning technology is given in the Table 2.1.

2.4.1 Formation of the Taylor cone

As discussed in sub-chapter 2.3 on the preceding page, first, the spinning liquid is introduced to the surface of the spinning electrode at a constant flow rate by a pressure-driven system or pump (e.x., linear, peristaltic, and screw pump). Then, the electrification of the liquid is occurred by applying the high-voltage difference between the spinning electrode and the collector (counter electrode). Depending on the electrical polarity of the applied high-voltage, the charges are transported to the surface of the liquid, which is commonly known as electrostatic induction. Upon gradually increasing of high voltage, more charges will be accumulated on the liquid surface, which results in the increased surface charge density. Therefore, the liquid droplet tends to deform its (or increase the surface area) shape to attenuate the electrostatic repulsion due to the continuous accumulation of the excess surface charges, which also experiences a Coulombic attractive force exerted by the external electric field. At the same time, the surface tension of the liquid tries to minimize the surface area. Hence, the droplet's shape deforms into another shape that minimizes the sum of electrostatic energy and surface-free energy.

Formation of DC cone jet

In order to the explain formation of DC cone jet via the way of electrohydrodynamics, the liquid droplet is assumed as a perfect conductor. When a sufficient high-voltage is applied to the conductive liquid, it experiences tangential stress on the surface due to the electric pressure (P_e). At the same time, capillary pressure (P_c) and hydrostatic pressure (P_h) at the surface of spinning solution acts in the direction against the electric pressure (P_e). Subsequent increases in applied voltage, P_e tends to suppress the P_c as well as P_h at a critical voltage of V_c . As a consequence, the liquid shape deforms into a Taylor cone,

Table 2.1: *DC vs AC electrospinning technology. (Abbreviation: E or E_0 =electric potential, ω = angular frequency, and t = time).*

DC electrospinning	AC electrospinning
DC high-voltage is constant at anytime ($E = E$)	AC high-voltage is a function of time ($E = E_0 \cos\omega t$)
Zero frequency of voltage	High-voltage can be manipulated via various waveforms & frequencies [20]
Liquid experience lesser degree of instability under the DC electric field [60]	Liquid experience higher degree of instability under the AC electric field [60]
Forms the Taylor cone with the half angle range of 32° to 49.3° [61, 62]	Forms conical regime with the angle of $\sim 9^\circ$ [61]
Jet experience either positive or negative charge polarity [23, 26]	Jet experience simultaneously positive and negative charge polarity [23, 26]
Jet's straight segment length is linearly proportional to the electric potential [52]	Jet's straight segment length is linearly proportional to the frequency of the AC high voltage
Higher degree of whipping instability [19]	Lower degree of whipping instability [19]
Since the whipping zone is giant, the fibers are away from each other during jetting [19]	Forms compact plume of fibers due to attraction between the positive and negative charged segments of the fibers [23]
Fibers are collected within the whipping zone	Fibers are collected above the virtual collector [23, 26]
Needs electrically active collector [63]	Works without an electrically active collector [23, 26]
The distance between the spinning-electrode and grounded collector is >3 cm	The distance between the spinning electrode and the virtual collector is the function of the frequency (i.e., 3 cm at 30 kV_{RMS} & 50 Hz) [23]
In most cases, the final product is in the form of the layered structure	Possible to get the bulky and multidimensional nanofibrous structure [21, 24, 28]

from which the electrified jet is ejected at the critical voltage. Thus, the highest charge density is presented at the apex of the Taylor cone from where the liquid is initiated towards the grounded collector. The hydrostatic, electric, and capillary pressure can be estimated for conductive liquid by $P_h = \rho g \xi$, $P_c = 2\gamma/r$, and $P_e = \varepsilon E^2/2$ respectively, where $\rho, g, \xi, \varepsilon, E, \gamma$, and r are the density of fluid, gravitational acceleration, depth of

the fluid, the electric permittivity of the gas in the vicinity of the electrode, total field strength, the surface tension of the liquid, and characteristic radius of the curvature of the liquid surface, respectively. Based on Taylor and Van Dyke's calculation, the critical voltage V_c (in kV) that is need for turning the droplet (with zero hydrostatic pressure) into a conical shape can be determined using the following formula (in CGSe unit) [51],

$$\sqrt{4\ln\left(\frac{2h}{r}\right)\pi\gamma 1.30(0.09)} < V_c < \sqrt{4\ln\left(\frac{4h}{r}\right)\pi\gamma 1.30(0.09)} \quad (2.1)$$

Where h is the distance between the liquid's surface and the collector (cm), R is the capillary radius of the spinneret (cm), and γ is the surface tension (dyn/cm). The constant 0.09 is used to estimate the voltage and the factor 1.3 is derived from $2 \cos 49.3^\circ$. As long as there is V_c and continuously supplying the adequate amount of liquid the droplet retains its conical shape during the electrospinning process.

Furthermore, Vaseashta investigated the dynamics of the multiple cone formation and he concluded that the conservation law of mass and momentum for both stretching and charged segments are the main mechanisms for a dynamic balance between the surface tension and bending instability [64]. Following the similar approach of the 1D model of wave equation such that the wave's vertical displacement along the z-axis is described using the periodic real part of a complex quantity ξ ,

$$\xi(x, t) = A \exp[i(kx - \omega t)]. \quad (2.2)$$

Where, A , k , ω , and t stand for the amplitude, wavenumber, angular frequency, and time, respectively. The wavenumber $k = 2\pi/\lambda$, and the angular frequency $\omega = 2\pi/T$ where λ is the wavelength and T is the period. Initially, the amplitude A of the wave is much smaller than its wavelength λ . However, when the liquid experiences external electric forces, the exponential growth of the amplitude of the liquid surface wave is achieved. The liquid in the spinneret is also subjected to gravitational and electrical fields in addition to capillary effects caused by the nonzero curvature of its surface.

Lukas *et al.* [65] formulated the following three basic hydrodynamic equations, the constitutive equation (ρ is constant), the continuity equation ($\Delta\Phi = 0$), and the Euler equation ($\rho\frac{\partial\vec{v}}{\partial t} + \nabla p = 0$), to study the behavior of liquid surface waves under external electric forces. They derived the Euler equation (used as a boundary condition) and the dynamic balance between the P_e , P_c and P_h with following assumptions: a velocity field $\vec{v} = \vec{v}[x(t), y(t), z(t), t]$, the conductive liquid is incompressible one, which means ρ is

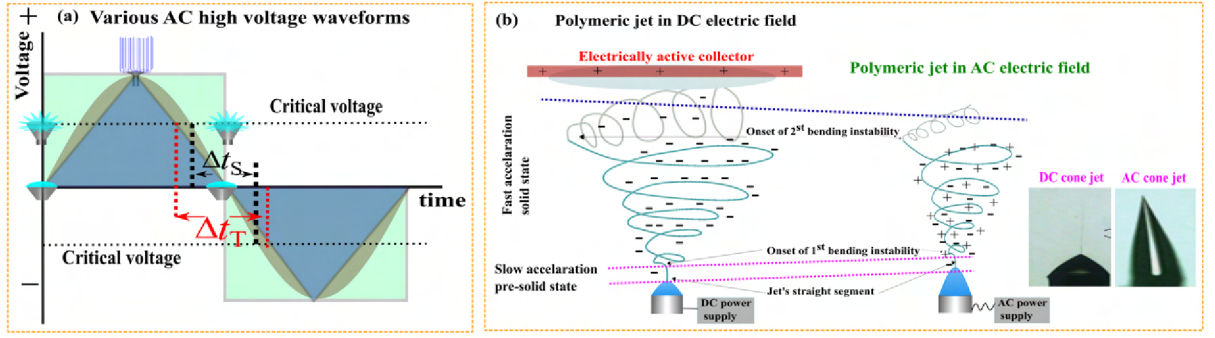


Figure 2.4: (a) *Electrohydrodynamic instability and jet ejection as a function of the time and voltage for various waveforms (Δt_S and Δt_T is the time interval between changes in the voltage polarity for the sine and triangle waveforms, respectively), and (b) The polymeric jet under the DC and AC electric field [61]*

constant, and the amplitude A of the wave is initially negligibly small, as compared to its wavelength λ . However, A comparable with λ at their later stage of time evolution. Since the jets evolve from the wave crests with higher amplitude than that of the lower amplitude at the initial stage. Simply, if $A \ll \lambda$, the liquid flow is a potential one, i.e., $\nabla \times \vec{v} = 0$, thus the time derivative of velocity ($d\vec{v}/dt$) can be approximated with its partial derivative $\partial\vec{v}/\partial t$. Since $\nabla \times \vec{v} = 0$, the scalar velocity potential can be introduced as $\vec{v} = \nabla\Phi$. These aspects simplify the Euler equation which is $\rho\frac{\partial\vec{v}}{\partial t} + \nabla p = 0$ into the following form

$$\nabla \left(\rho \frac{\partial\Phi}{\partial t} + P \right) = 0. \quad (2.3)$$

To investigate the liquid surface dynamics, Eq. 2.3 is further reshaped by investigating the liquid's surface pressure (P). The P is consisting of the components of hydrostatic pressure ($P_h = \rho g\xi$), capillary pressure $P_c = -\gamma(\partial^2\xi/\partial x^2)$, and electric pressure $P_e = \frac{1}{2}\varepsilon E^2 \cong \frac{1}{2}\varepsilon E_0^2 + \varepsilon E_0^2 k\xi$ and whose gradients are non-zero, the boundary condition at the liquid surface reshapes as

$$\rho \frac{\partial\Phi}{\partial t} \Big|_{z=\xi} + \rho g\xi - \gamma \frac{\partial^2\xi}{\partial x^2} - \varepsilon E_0^2 k\xi = 0. \quad (2.4)$$

The velocity potential Φ on the surface of the liquid (i.e., $z = \xi \cong 0$) and the velocity component v_z of the liquid surface are related as $V_z = \partial\xi/\partial t = \partial\Phi/\partial z|_{z=0}$. Also, the term $\partial\xi(x, t)/\partial t$ may be expressed as $-i\omega A \exp[i(kx - \omega t)]$. Since, the velocity potential on the surface quenches with infinite depth of the liquid ($z \rightarrow \infty$), $\Phi(x, z, t)$ is supposed to be $\Phi(x, z, t) = B \exp(+kz) \exp[i(kx - \omega t)]$, thus, implying $\Phi(x, z, t)/\partial z = kB \exp[i(kx - \omega t)]$. Using the Eq. 2.4 and along with derived expressions for Φ and that for B , a dispersion

law for ω^2 is exhibited as

$$\omega^2 = (\rho g + \gamma k^2 - \varepsilon E_0^2 k) \frac{k}{\rho} \quad (2.5)$$

It is clear from Eq. 2.5 that ω^2 depends on the gravitational acceleration (g), wave number (k), liquid surface tension (γ), liquid density (ρ), and field strength (E_o). The field strength E_o is a crucial parameter for starting a jetting for a specific polymer solution or liquid. When E_o exceeds a critical electric field strength E_c , ω^2 turn into a negative, and consequently, ω becomes an imaginary quantity. Additionally, it is acknowledged that the self-organization of electrohydrodynamic formation is demonstrated by the exponential growth of the amplitude of jets on free liquid surfaces [65]. The critical condition can be obtained by setting ω^2 accompanied by the condition $\partial\omega/\partial t = 0$. Thus, Eq. 2.5, i.e., $\omega^2(k) = 0$ provides the minimal or critical value of the growing wave's wavenumber $k_c = \varepsilon E_c^2 / 2\gamma$. Subsequently, as shown Eq. 2.6, the critical field strength E_c for growing wave or unstable waves is obtained by substituting the k_c for k in the dispersion equation, i.e., Eq. 2.5 [65, 66].

$$E_c = \sqrt[4]{4\gamma\rho g/\varepsilon^2}. \quad (2.6)$$

Additionally, by solving $d\omega^2/dk = 0$, the minimum value of the squared angular frequency with respect to wavenumber k is obtained as follows,

$$k_{1,2} = \frac{2\varepsilon E_0^2 \pm \sqrt{(2\varepsilon E_0^2)^2 - 12\gamma\rho g}}{6\gamma}. \quad (2.7)$$

From Eq. 2.7, the average distance between two neighboring jets can be expressed in terms of wavelength $\lambda = 2\pi/k$ as

$$\lambda = 12\pi\gamma \left[2\varepsilon E_0^2 \pm \sqrt{(2\varepsilon E_0^2)^2 - 12\gamma\rho g} \right] \quad (2.8)$$

Also, its dependency on E_o is shown in Fig. 2.5. Furthermore, the distance between neighboring jets was more comprehensively described using capillary length $a_c = \sqrt{\gamma/\rho g}$, and the electrospinning number $\Gamma = a\varepsilon E_o^2/2\gamma$ as $\lambda = 3\pi a/(\Gamma + \sqrt{\Gamma^2 - 3/4})$. The inter-jet distance can be described as dimensional-less quantity $\Lambda = \lambda/a_c$, and its relationship with Γ is universal for free surface electrospinning, i.e., needleless electrospinning, which is $\Gamma_c = 2\pi$. The relation between dimensionless inter-jet and the electrospinning number is given below as

$$\Lambda = 3\pi/\Gamma + \sqrt{\Gamma^2 - 3/4}. \quad (2.9)$$

Similarly, the relationship between dimensionless relaxation time $T = \tau/\sqrt{a_c/g}$ and electrospinning number was also derived by substituting the dimensionless wave number $K = 2\pi/\Lambda$ and dimensionless wavelength Λ for k and λ , respectively in Eq. 2.5. The relationship T and Γ is shown in Fig. 2.5a and in Eq. 2.10 as

$$\Gamma = \sqrt{\frac{3}{2K(K\Gamma - 1)}}. \quad (2.10)$$

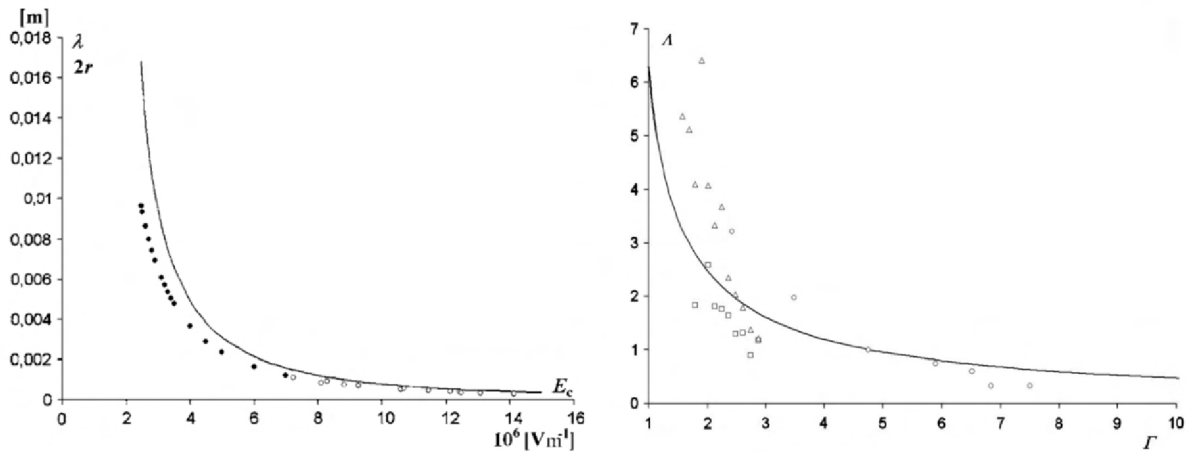


Figure 2.5: (a) Relationship between inter-jet distance λ and the critical field strength E_c and (b) dependence of dimensionless wavelength Λ on electrospinning number Γ [65].

Formation of AC slender cone regime

The AC electrospinning technology differs from common DC electrospinning in terms of the applied high-voltage and the fiber collection process. Although the AC field strength is time-varying, $E(t) = E_0 \cos(\omega t)$, the electric pressure is always positive and acting upwards from the surface of the liquid; which is clearly observed from the equation of electric pressure $P_e = \varepsilon E_t^2/2$. This electric pressure in the liquid is not constant since the polarity and voltage of the AC potential are functions of time (Fig. 2.4a). Hence, during the AC electrospinning, some of the jets are quenched when electric pressure decreases. Subsequently, when it increases, a few of the jets are created again from the free surface of the liquid at time periods of 0.0006 s (applied voltage 30 kV and frequency 50 Hz) [23]. The polymeric jet consists of positive and negative charged segments whose length depends mostly on the frequency of the AC voltaic waveform (Fig. 2.4a, b, and Fig. 2.6b). In addition, depending on the frequency and voltage of the AC waveform, the ambient gas

molecules at the vicinity of the spinning electrode are being ionized and, consequently, result in the formation of an ionic cloud. This ionic cloud attracts the oppositely charged segments of the emerging jet, and thus acts as a virtual collector.

Maheswari *et al.* studied the distinction between the shape of the DC and AC cone jets of ethanol [61]. They reported that the half-angle of the DC cone is 47° (insert of Fig. 2.4b). Conversely, under the AC field instead of forming the Taylor cone shape, it deformed into a lesser angle conical regime with an angle of 9° (insert of Fig. 2.4b). It can be seen that the AC cone angle is significantly less than in the DC case although the same fluid was used. This can be related to the spinning solution's charge relaxation time $\tau_e = \varepsilon/4\pi k$, where, ε and k are dielectric constant and conductivity of the spinning solution [67]. This regime of slender conical meniscus happens when the applied relevant frequency time scale (for 15 kHz is $33 \mu\text{s}$) is at least an order of magnitude smaller than the charge relaxation time of the meniscus (for ethanol is $310 \mu\text{s}$). It indicates that the meniscus experiences insufficient time to relax. An alternative explanation is that the applied AC high voltage frequency tends to change the polarity of the high-voltage much quicker. However, the liquid refuses to cooperate in reversing the polarity since it needs more time. This implies that the meniscus is not fully discharged. Thus, the resulting coulombic repulsion sustains the AC cone. In addition, the AC cone angle was approximately constant for the wide range of applied frequencies (15 to 200 kHz).

As previously discussed, the onset of electrospinning can be described as a dynamic balance between the electric pressure and capillary force. Since the polymeric solution has sufficient entanglement, the polymeric drop under the sufficient electric field transforms into a Taylor cone followed by the formation of charged jets and solidifies into polymer filaments under a dynamic balance of air drag, electric field, and gravitational field forces, thus producing jets towards the counter electrode.

Most developed theories currently available are based on DC electrospinning. However, it is hard to find a theoretical description of the onset of AC electrospinning. In the previous sub sub-chapter, the theory about the instability of liquid under the DC electric field was discussed. Since the AC electric field $E = E_0 \cos \omega t$ is the function of time, it modifies the Euler equation $\nabla \left(\rho \frac{\partial \Phi}{\partial t} + P \right) = 0$ into the linear second ordinary differential equation with time oscillating coefficient, as given below,

$$\frac{\partial^2 A(t)}{\partial t^2} + gkA(t) + \frac{\gamma}{\rho} k^3 A(t) - \frac{\epsilon_0 k^2}{\rho} E_0^2 \cos^2 \omega t A(t). \quad (2.11)$$

Eq. 2.11, further can be simplified using the following relation $\cos^2 x = \frac{1}{2} \cos 2x + \frac{1}{2}$,

$$\frac{\partial^2 A(t)}{\partial t^2} + \left[\left(gk + \frac{\gamma}{\rho} k^3 - \frac{\epsilon_0 k^2}{2\rho} E_0^2 \right) - \frac{\epsilon_0 k^2}{2\rho} E_0^2 \cos^2 \omega t \right] A(t). \quad (2.12)$$

By introducing the following dimensionless quantities, electrospinning number $\Gamma = \epsilon_0 a_c E_0^2 / 2\gamma$, dimensionless frequency $\Omega^2 = a_c / g T^2$, dimensionless wavenumber $K = a_c k$ and dimensionless relaxation time $\tau = \sqrt{(g/a_c)} t$ (as we did for DC case), Eq. 2.12 converted into the following form,

$$\frac{\partial^2 A(\tau)}{\partial \tau^2} + \left[\frac{K}{\Omega^2} (1 - \Gamma K + K^2) - \frac{1}{\Omega^2} \Gamma K^2 \cos 2\tau \right] A(\tau) = 0. \quad (2.13)$$

This equation resembles the Mathieu equation (Eq. 2.14), which is a homogeneous second-order linear differential equation with a periodically variable coefficient.

$$\frac{\partial^2 A(\tau)}{\partial \tau^2} + (a - 2q \cos 2\tau A(\tau)) = 0. \quad (2.14)$$

$$\frac{\partial^2 A(\tau)}{\partial \tau^2} = \frac{a}{g} \frac{\partial^2 A(t)}{\partial t^2}, \quad a = \frac{K}{\Omega^2} (1 - \Gamma K + K^2), \quad 2q = \frac{1}{\Omega^2} \Gamma K^2.$$

Where $A(\tau)$ represents the non-harmonic capillary wave's amplitude, a , and q are the Mathieu equation parameters that were compiled from the liquid's physicochemical properties and electric field intensity. The parameter determining hydrodynamic instability, which has the character of self-organization using the mechanism of the fastest growing instability, is so-called characteristic Mathieu exponent. The total extreme of the characteristic Mathieu exponents will provide a prediction of the characteristic hydrodynamic time and distance between neighboring jets.

2.4.2 Stretching of the charged jet

The higher charge density is located at the apex of the Taylor cone, from where the jet will be ejected. Subsequently, the ejected jet is accelerated, followed by further extensions by the external electric field towards the grounded collector. The ejected jet initially flows in a straight line for a certain distance near the spinneret. The electrification of the liquid followed by the Taylor cone formation and subsequent jet ejection are called near-field slow acceleration pre-solid states.

Stretching of charged jet in DC electric field

As shown in Fig. 2.6a, once the jet is ejected from the Taylor cone's apex, the length of straight line segment is linearly proportional to the applied DC high-voltage [52, 68]. Thanks to the viscoelastic and electric stress of spinning liquid as well as the rapid evaporation of the solvent, which suppresses the Rayleigh instability, as a consequence jet continuously stretched (or elongated) until it solidifies. Otherwise, the Rayleigh instability causes a break in the charged jet to form the spherical droplets. Since the charges (or ions) travel along with the liquid jet, it feels the electric stress throughout its journey. The charge velocity in the straight segment (V_d), as well as the critical length of the jet's straight segment (L) can be measured using the following equations [69]:

$$V_d = \frac{\varepsilon z_i}{6\pi a \eta} E_e \quad (2.15)$$

where, (Eq. 2.15), ε , z_i , η , a and E_e are the absolute value of the charge of an electron, the valence of the charge carriers, solvent viscosity, mean radius of the ions, and electric field strength, respectively.

$$L = \frac{4kq^3}{\pi\rho^2 I^2} \left(\frac{1}{R_0^2} - \frac{1}{r_0^2} \right) \quad (2.16)$$

where, (Eq. 2.16), $R_0 = (2\sigma Q/\pi k\rho E)^{1/3}$, σ , Q , k , ρ , and r_0 are the surface charge, liquid's flow rate, the electrical conductivity of the liquid, the density of the solution, and the initial radius of the jet, respectively. I is the current passing through the jet.

Stretching of the charged jet in AC electric field

In the case of AC electrospinning, the length of the straight segment of the jet is determined by the waveform and frequency of the applied AC high voltage. If the frequency of the high-voltage increases the length of the charged jet segment decreases. This could be attributed to the fact that the lower frequency high-voltage consists of a single polarity (either positive or negative) over a longer time. Conversely, if the frequency is relatively high, the polymeric jet is subjected to the rapid alteration of positive and negative charge polarities [30]. Hence, the jet's charged segments will be smaller when a higher frequency of AC high voltage is used than that of lower frequencies (Fig. 2.6b). Regardless of the effective AC high-voltage, the polymeric jet's straight segment is mainly influenced by the frequency of the AC high voltage. The impacts of various waveforms and frequencies of AC high-voltage on the electrospinnability, morphology, and productivity of PCL

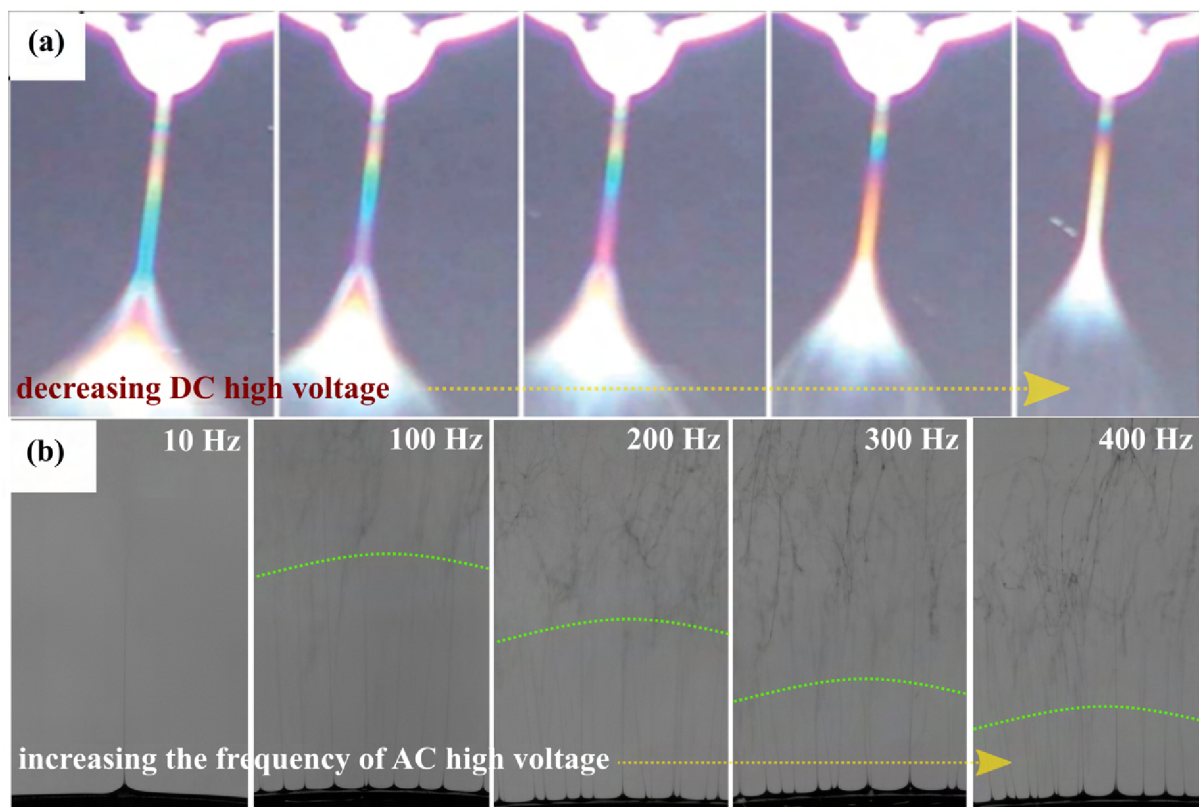


Figure 2.6: (a) *Stretching of the charged jet in the DC electric field* [52, 68] and (b) *stretching of the charged jet in the AC electric field*.

electrospun was profoundly discussed in Chapter 4.2 on page 75.

2.4.3 Thinning or bending instability of the charged jet

Fluid instabilities (Rayleigh–Plateau and Richtmyer–Meshkov instability) are generally thought to be detrimental to the electrospinning process since they lead to breaking up the liquid jet (known as electrospraying). However, bending instability is vital to the formation of electrospun fibers during the electrospinning process. The charged liquid jet may experience the following three types of instabilities: (1) Plateau–Rayleigh instability (detrimental to the electrospinning process), (2) axisymmetric instability, and (3) bending or whipping instability. The latter instability gives a substantial contribution to the formation of electrospun nanofiber. Studying the actual dynamics of a jet’s whipping instability is hard as it is a very fast phenomenon. Fig. 2.4b depicts the jet formation stages in the DC and AC electrospinning process. The dynamics for the jet’s bending instability can be explained by the well-known Earnshaw’s theorem. It states that a charged body cannot be able to maintain a steady equilibrium condition by relying merely on the interac-

tion between charges [70]. Doshi and Renekar initially proposed that electrospun fibers are created by splitting the single charged jet into multiple jets due to increased surface charge density when the jet diameter decreases [71]. However, shin *et al.* demonstrated that jet splaying is simply an optical artifact caused by the rapid movement of the jet during the bending instability process; in reality, the charged jet is rapidly whipping [53].

Thinning of the charged jet in DC electric field

In addition to jet initiation (as described in Chapter 2.4.2 on page 22), viscoelastic forces and surface tension also dominate the charged jet's velocity in the straight line segment. These two forces tend to prevent the jet's movements toward the counter electrode. As a consequence, the jet's acceleration is gradually attenuated. Meanwhile, the jet however moves forward or stretched regardless of its velocity due to the electric pressure. Hence diameter of the jet gradually decreased. When the velocity of the jet is constant or drops to zero, any small perturbation can able to distorts the straight movements of the jet. Since the liquid jet carries excess charges, this small perturbation in the charged jet triggers the electrically driven instability also referred to as whipping or bending instability [8, 9]. From now on, the jet enters into the fast acceleration solid-state, also referred to as the far-field regime (Fig. 2.4 on page 18b).

Although this fast acceleration solid-state process is not fully understood, the experimental analysis shows that the charged jet experiences non-axisymmetric instabilities driven by electric pressure. This non-axisymmetric instability is generally referred to as bending or whipping instability. Renekar *et al.* reported three steps in the initiation of the bending cycle, which follow as (i) a straight segment of the jet suddenly develops a linear array of bends. (ii) As the jet segments in each bend elongated due to excess charge (or electric pressure), the linear array of bends became a series of spiraling loops with increasing size. (iii) as the spiral loops grow, the cross-section diameter of the jet decreases, and consequently, nano-sized electrospun fibers were obtained [8, 9].

Thinning of the charged jet in AC electric field

In the DC electrospinning process, the jet experiences single polarity (i.e., higher net charge), thus the jet will be stretched as much as possible towards the counter electrode (Fig. 2.4b). Conversely, the net charge in the jet is reduced under the AC field since the jet is simultaneously experienced the positive and negative charge polarities. It causes a lesser extent of the jet to whip and stretch (Fig. 2.4b). Besides, the emerging electro-

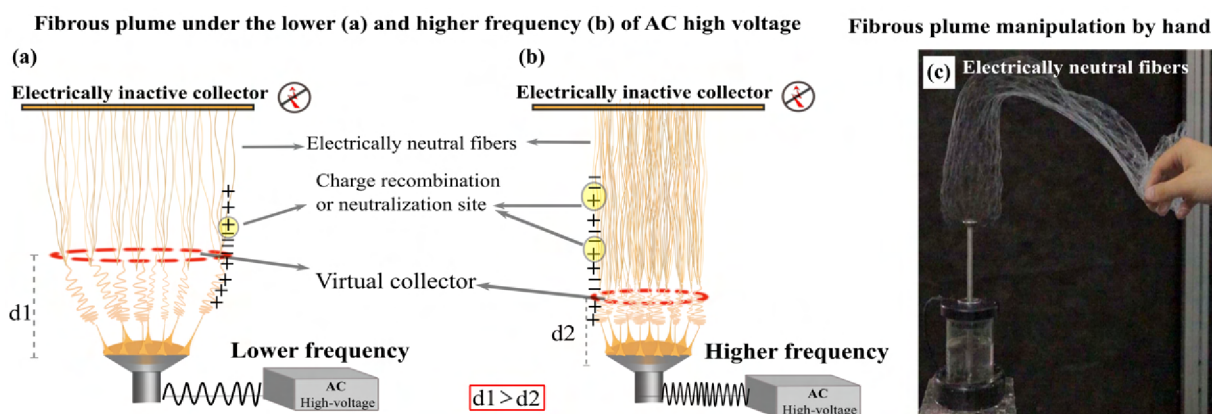


Figure 2.7: *Fibrous plume under the lower (a) and higher frequency (b) of AC high voltage, and (c) Manipulation of emerging nanofibrous plume by hand to demonstrate that the nanofibrous plume can be collected on an electrically inactive substrate as well. It implies that this method works without any electrically active or grounded collector [24]. ($d1$ and $d2$ represent the distance between the AC spinneret and the virtual collector at lower and higher frequencies, respectively).*

spun fibers following the various instabilities also consist of the charged segments. These charged segments of each electrospun fiber are attracted to each other or in other words charges were recombined (Fig. 2.7). Consequently, these fibers were self-bundled and forms a compact plume structure in the zone of the virtual collector (Fig. 2.7). The fibrous plume mutually communicates with the surrounding electric wind, which is created by the AC field. Thus it moves continuously upwards from the electrode. Since the electric wind critically governs the movements of the fibrous plume, there is no necessity to use the electrically active collector for collecting the electrospun fibers during the entire AC electrospinning process. The self-bundling tendency of such AC-produced fibrous plumes significantly simplifies the collection of fibers compared to the DC electrospinning approach.

2.4.4 Solidification and subsequent fiber deposition

The final stage of electrospinning is the solidification of the jet due to the evaporation of solvent, followed by the deposition of dried polymeric electrospun fibers on the grounded collector. During the DC or AC electrospinning, the solvent starts to evaporate from the polymeric jet in three stages [72–74]: (i) emanation of the jet from the liquid surface, (ii) formation of straight jet, and (iii) whipping/bending instability. The solvent molecules tend to evaporate at a critical rate and a critical time at each stage of the jet movements. For instance, during stages (i) and (ii), solvent evaporation occurs merely by diffusion

mechanism due to the lower velocity of the air in the vicinity of the polymer solution. In the case of the bending/whipping region (stage (iii)), the jet starts to stretch due to the whipping movements, thus leading to an increase in the surface area of the jet, and as a result, high air velocities are created in the vicinity of the jet. This promotes efficient evaporation of the solvent through the convection mechanism due to the whipping movements of the jet. As a consequence, solidified polymers are collected in the form of electrospun fibers. Also, Wu *et al.* demonstrated a higher degree of in-homogeneity of solvent concentration over the microscopic jet cross-section than in the sub-micrometer jet cross-sections [72]. During the evaporation process, a 50 μm radius jet initially had a solvent concentration of 0.9 g/cm^3 , which radius and concentration were reduced to 20 μm and 0 g/cm^3 , respectively, within 3.6 s.

The solidification of the jet is much quicker in high viscous solutions since polymeric chain entanglements are higher than that in low viscous solutions. When the solidification of the jet is rapid, the elongation process of the jet can continue only for a limited time. However, during the DC electrospinning dried jet continuously flying towards the grounded collector consequently, dried electrospun fibers were deposited on collector where the excess charges on the fibers are rapidly dissipated.

Solidification of AC electrospun

In the case of AC electrospinning, charges in the electrospun fibers were mutually neutralized at the virtual collector. Thus, above the virtual collector there is no electrically driven stretching of the dried electrospun jet. Hence, AC electrospun fibers can be collected on electrically inactive substrate. Interestingly, as shown in Fig. 2.7c, AC electrospun fibers can be also manipulated by the naked hand at a certain distance from the spinneret (i.e., above the virtual collector). In contrast, the jet under the DC electric field will be stretched (due to repulsion of charge) until it reaches the counter electrode, where the charges are neutralized. Also, the distance between the AC spinneret and the virtual collector is in any case much smaller (~ 3 cm) than the distance between the DC spinneret and the grounded collector (~ 10 cm). Hence there could be a relatively higher amount of residual solvents present in the AC electrospun fibers than in the DC electrospun fibers. However, these residual solvents can be removed by keeping the electrospun fibers in the ambient condition or aerated.

2.5 Materials used in AC electrospinning

Although a wide range of materials such as polymers, sol–gels, and small molecules has been used to fabricate the electrospun fibers using electrospinning, polymers are the most commonly used in the form of a solution or melt, due to their inherent properties [75]. Since AC electrospinning is an emerging technology, only a very few polymers have been electrospun into nanofibers. For instance, Lukas’s group, Beran’s group, Pokorny’s group and Chvojka’s group from the Technical University of Liberec (Czech Republic), Stanishvsky’s group from the University of Alabama at Birmingham (USA), and Nagy’s group from the Budapest University of Technology and Economics (Hungary) have investigated the AC spinnability of polymeric and non–polymeric materials [20, 23–25, 59]. The following subsections give a brief account of the materials in the context of AC electrospinning or AC electrospun nanofiber.

2.5.1 AC electrospinnability of various solutions

The author’s best knowledge, polyethylene oxide (PEO) was the first polymer that was used by Kessick *et al.* to study the impact of AC and DC potential on the electrospinnability [19]. They demonstrated that compared to utilizing DC potential, AC potential reduces or eliminates the liquid jet instability and degree of solvent evaporation. Additionally, the PEO electrospun was deposited on the target without any electrically driven support. The characteristics of AC potential are responsible for this behavior. They explained this behavior, stating that the jet’s net charge is lowered in the presence of an AC electric field, which in turn reduces fiber instability. Due to its AC nature, the electrospun consist of charge segments with alternating polarity, whose length depends on the frequency of the AC high–voltage. The electrospun PEO nanofibrous mats produced from AC electrospinning reflect a higher degree of fiber alignment and contain residual solvents due to reduced fiber instability (Fig. 2.8a). Whereas the PEO nanofibrous mats from DC electrospinning exhibit a much smaller fiber diameter than the AC spun mats since the charged jet experienced a higher degree of instability in the DC electric field (Fig. 2.8b).

Fabrication of electrospun nanofibrous yarns

For the first time, Maheshwari *et al.* demonstrated that AC potential is feasible to fabricate the multi–strand nanofibrous threads using polyvinyl pyrrolidone (12% w/w) [26]. Under the AC electric field, the whipping envelope shape was characteristically different

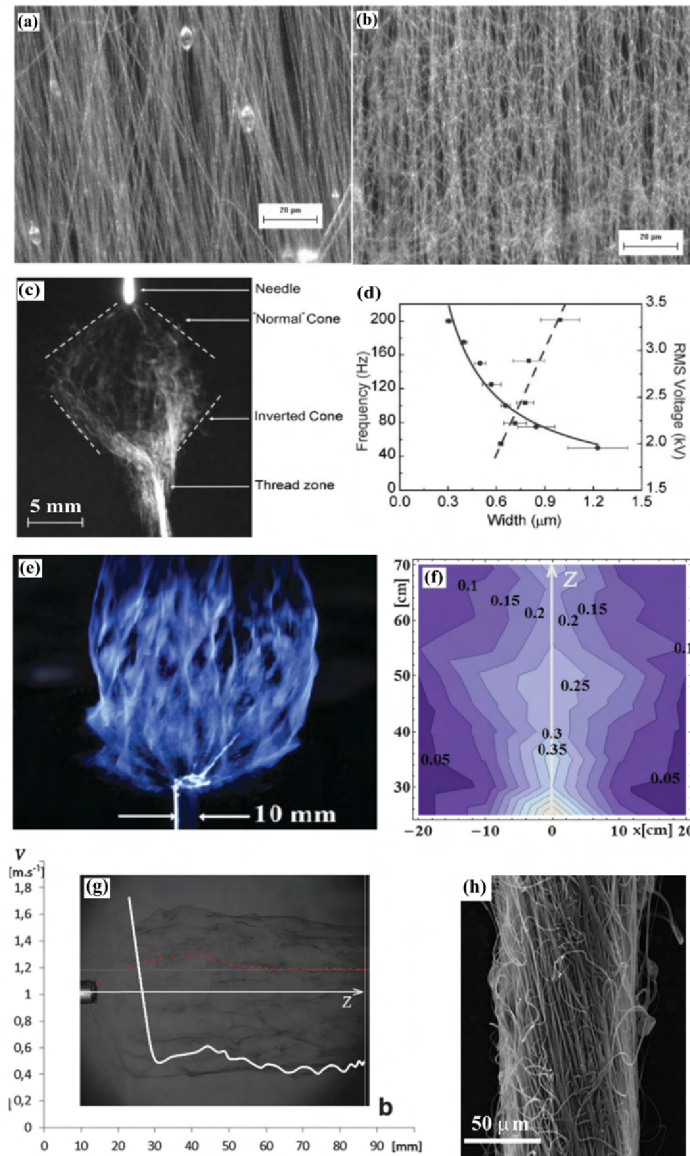


Figure 2.8: *Optical microscope images of PEO AC (a) and DC (b) electrospun fibers [19], (c) photograph of the AC electrospinning process, which was taken at an exposure time of 20 ms. The whipping envelope can be seen as a combination of a normal upright cone and an inverted cone. A distinct thread zone is seen below the apex of the inverted cone, (d) variation of the area of the whipping envelope with frequency and voltage [26], (e) PVB nanofibrous plume emerging from rod spinning electrode, (f) the contour plot of electric wind velocity's vertical components (cm s^{-1}) created by the spinning electrode with a diameter of 1 cm whose axis coincidences with the z coordinate ($30 \text{ kV}_{\text{RMS}}$ with a frequency of 50 Hz), (g) red dots denote the typical track of a liquid droplet inside the nanofibrous plume recorded using a high-speed camera. A plot of the velocity magnitude values v is included as a function of the z -axis distance from the spinning-electrode, which exhibits an abrupt change in the velocity derivative close to the distance $z = 3 \text{ cm}$, and (h) PVB electrospun nanofibrous yarn produced using AC electrospinning [23].*

as compared to the DC electrospinning (in the DC case, only upright cone shape). As shown in Fig. 2.8c, the shape of the whipping envelope was the combination of the usual upright cone and an unusual inverted cone. The later cone may also be formed due to the author's intentional mechanical drowning of the nanofibrous plume to deposit on the flexible cable. Seemingly, the zone of thread formation appeared just below the apex of the inverted cone. This thread formation occurred only at an appropriate frequency of the AC high-voltage. The applied AC potential and the frequency strongly influenced the area of the whipping region. As shown in Fig. 2.8d, it increased with the applied AC high-voltage while decreasing with frequency. Thus it is clear that the AC potential and the frequency display a linear and inverse trend with the area of the whipping region.

Similarly, PVB electrospun nanofibrous yarn was fabricated by Pokorny *et al.* at an applied AC high-voltage of 30 kV_{RMS} with the frequency of 50 Hz (2.8h) [23]. The vertical components of electric wind velocity and the position of the virtual collector were measured for the spinning electrode, which had a diameter of 1 cm and a length of 15 cm (connected with the AC high-voltage source with 30 kV_{RMS} and frequency of 50 Hz). The highest electric wind velocity value at the point nearest to the spinning electrode was $57 \pm 14 \text{ cm s}^{-1}$ (Fig. 2.8f). As shown in Fig. 2.8g, by tracking the liquid droplet's movements inside the fibrous plume, the impact of the electric wind combined with the movement of the nanofibrous plume was also investigated. The second derivative of the velocity magnitude curve was observed at a distance of $2.9 \pm 8 \text{ cm}$ above the surface of the spinning electrode. Prior to the virtual collector, the velocity magnitude drastically declines, whereas, behind it, which almost remains constant, $46 \pm 8 \text{ cm s}^{-1}$. This value is consistent with the anemometer-measured electric wind velocities. Thus, it can be assumed that the virtual collector was formed at this distance, and also, the net charges of nanofibrous segments have recombined (Fig. 2.7) or vanished here.

Fabrication of electrospun nanofibrous composite yarns

The AC electrospinning has a high potential to create the composite yarn that is nanofibers coated classic yarn. This kind of composite yarn fabrication is technologically challenging using common DC electrospinning since it requires an electrically active collector, which interns an obstacle for coating nanofibers on the core yarn. Otherwise, the core yarn should be electrically active; however, it is practically less feasible to fabricate composite yarns continuously. Valtera *et al.* fabricated the various types of composite yarns using PVB and PA6 as the nanofibrous sheath and PES or PA6 as a core yarn with varying linear density (Fig. 2.9a and b) [24]. By using more than one spinning electrode, it can be

possible to achieve a multilayered nanofibrous sheath with various functional properties. In addition, they showed that increasing the number of the spinning electrode from one to three enables the industrial-level production of composite yarns from 600 to 3600 m/hour.

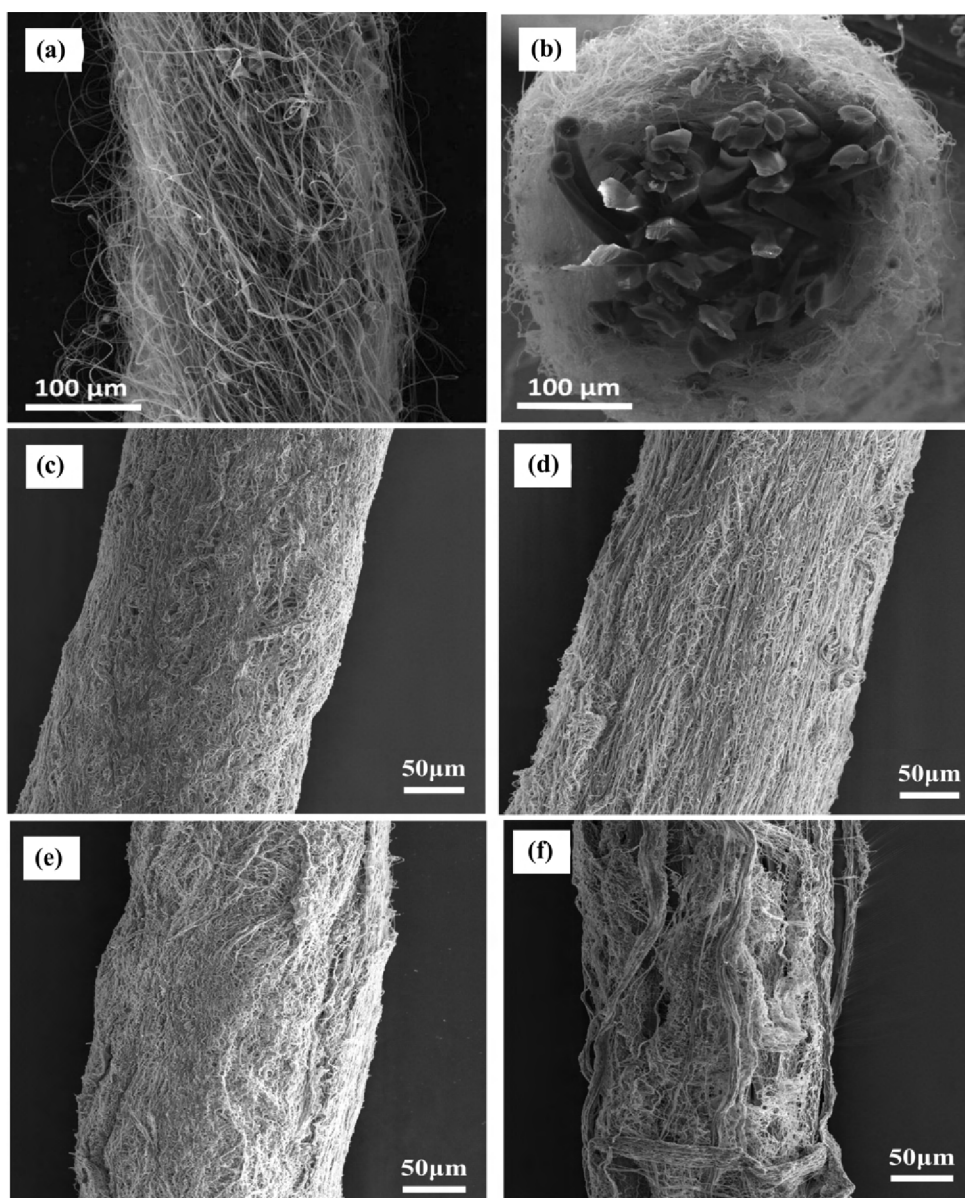


Figure 2.9: (a) morphology of polyester core - PA nanofibrous sheath composite yarn, (b) cross-section image of polyester core - PA nanofibrous sheath composite yarn [24], (c) morphology of PA6 core - PA6 nanofibrous sheath composite yarn, (d) PA6 core - PA6/chlorhexidine nanofibrous sheath composite yarn, (e) PA6 core - PU nanofibrous sheath composite yarn, and (f) PA6 core - PU/chlorhexidine nanofibrous sheath composite yarn [21].

Madheswaran *et al.* for the first time fabricated the classic core-antibacterial nanofibrous sheath composite yarns using the AC electrospinning technology (Fig. 2.9c to f) [21].

They proposed that these functional composite yarns could be used as surgical sutures since it has consistent mechanical and functional properties. The core yarn gives the overall mechanical property while the nanofibrous envelope provides the functional properties. The fabricated composite yarns exhibit biocompatibility with antibacterial, adequate mechanical, and thermal properties. The only minor problem with the composite nanofibrous is the lower adhesion between the core and the nanofibrous envelope, which was between 0.7 to 8.5 N. This force depends on the used core and nanofibrous envelope as well as the degree of twisting of the nanofibers [21, 24].

Fabrication of electrospun nanofibrous mats

Three years later, Kessick's invention, Sarkar *et al.* used pristine PEO and nanoparticle, or carbon nanotube blended PEO polymeric solution to study the AC, and DC high-voltage impact on the electrospinnability [76]. They reported that the AC spinnability was stable at only a specific frequency range, however, which depends on the used spinning solution. Their findings (AC spinnability and the electrospun morphology) as well are in line with Kessick *et al.* [19]. Lawson *et al.* produced PCL electrospun nanofibrous mats using free surface AC electrospinning [54]. They demonstrated that PCL electrospun nanofibers with a diameter range of 150 to 2000 nm could be produced at production rates up to 14 g/h using glacial acetic acid as a solvent and sodium acetate as an additive. At the applied AC high-voltage of 20 or 38 kV, the PCL electrospun fibers with a diameter of 150 to 300 nm and microfibers were produced from the solutions of 10 and 20 wt% PCL with 2 wt% sodium acetate, respectively.

Another study showed that the applied high voltage significantly influences the surface energy of the PCL electrospun nanofibrous layer and, consequently, affects the glycerol or hydrogel wettability of PCL [28, 77]. The DC electrospun PCL layer exhibited higher surface energy (44.1 mJ/m²), whereas approximately one order lesser degree of surface energy (5.2 mJ/m²) was observed for the AC electrospun layer compared to DC spun layer. The different surface energy values of PCL layers were caused by the conformations of macromolecules which were significantly affected by the DC and AC electric fields. In addition, the frequency of applied AC high voltage also strongly influences the surface energy of the PCL mat and, thus, their wetting behavior (Fig. 2.10a and b). The surface energy decreased from 51.70 to 46.94 mJ/m² when the frequency increased from 10 Hz to 50 Hz [28]. The surface energy of AC spun PCL was not considerably affected by the concentration of the PCL.

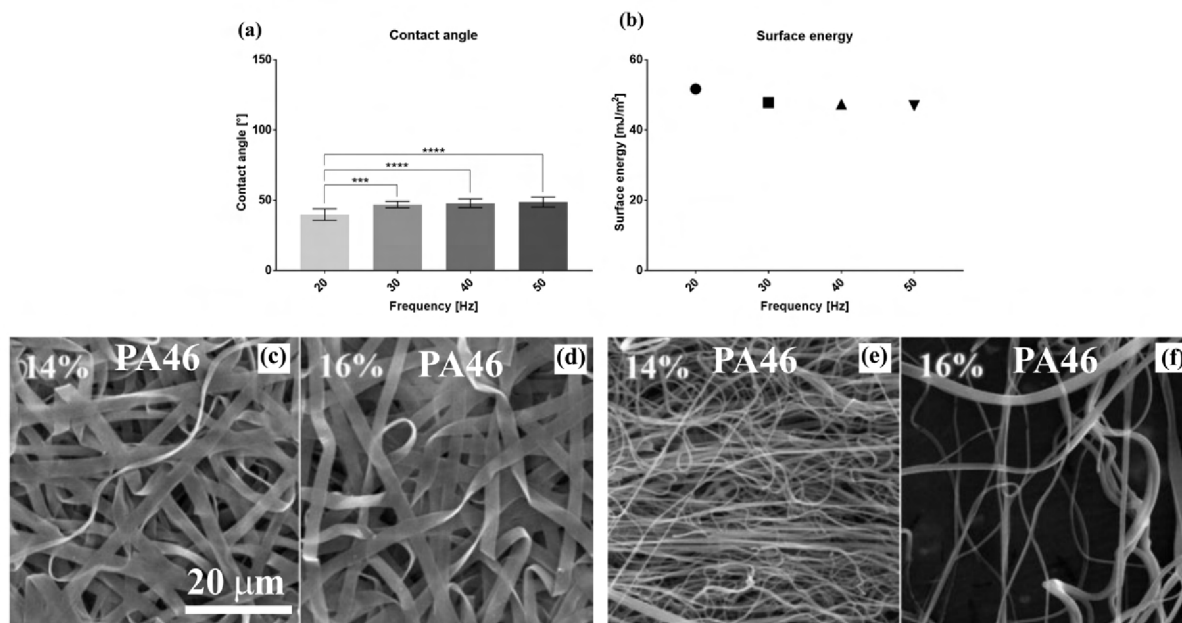


Figure 2.10: *Glycerol contact angle (a) and surface energies (b) of AC electrospun PCL layers [28], and PA46 electrospun nanofiber produced from DC (c and d) and AC (e and f) electrospinning (PA46 concentration is 14 or 16 wt%) [55].*

PA-based AC electrospun fibers were also fabricated by Kalous *et al.* and Holec *et al.* [27, 55, 78] using formic acid/acetic acid, and formic acid/dichloromethane, respectively. The former author used sulfuric acid (0.2 mol/L) or methanesulfonic acid (0.37 mol/L) as an additive for enhancing the AC spinnability of PA since, without an additive, the compact fibrous plume did not appear. Interestingly, DC spun PA46 reflected the ribbon structured fibers, whereas AC spun resulted in mostly cylindrical structured fibers with very few ribbon structures (Fig. 2.10c – f). Also, there is no clear correlation observed between the DC and AC spun PA-based fibers. The surface energy of PA-based DC electrospun fibers was increased when the number of carbon in the repeating units of PA decreased. Thus PA4 resulted in a lower contact angle than PA11. AC spinnability of PA6 was significantly influenced by the applied AC high-voltage waveforms and frequencies. The square waveform of the AC high voltage evinced higher productivity of electrospun fibers than the sine waveform. The variation of productivity was linear with the frequency of AC high voltage. It is considered that each polymer solution has a frequency limit. After this frequency is exceeded, no good-quality nanofibers can be created. In the case of PA6, the frequency limit was 50 to 150 Hz (for sine and square waveforms; amplitude voltage of 42 kV_{RMS}) and for polyvinylpyrrolidone–vinyl acetate copolymer was 50 to 100 Hz (sine, square, triangle, and sawtooth waveforms; 25 kV_{RMS}) [25, 27].

Apart from polymeric electrospun nanofibers, ceramic electrospun fibers have been also produced using AC electrospinning [59, 79–81]. Stanishevsky *et al.* fabricated the nanofibrous alumina structures from the aluminum nitrate/poly-vinylpyrrolidone (PVP) electrospun nanofibers using AC electrospinning at an applied voltage of 40 kV_(RMS) (frequency: 50 or 60 Hz) [59]. The calcination was performed on the aluminum nitrate/PVP electrospun nanofibers at a temperature between 700 – 100 °C in order to get nanofibrous alumina structures. The resultant fibrous material could be used as gas filters and separation membranes. L. Nealy *et al.* produced titanium dioxide (TiO₂) nanofibers from the TiO₂/PVP/ hydroxypropyl cellulose (HPC) precursor solution [79]. They found that the resultant nanocrystalline TiO₂ nanofiber’s morphology, size, as well as the composition of crystalline phases is the function of the mass ratio of the TiO₂/PVP/ HPC. The productivity of TiO₂/PVP/ HPC electrospun nanofibers was inversely proportional to the increase of TiO₂/polymer mass ratio regardless of the electric potential, spinneret geometry, and rheological properties of the precursor solution. The higher throughput of crystalline TiO₂ nanofibers (5.2 g/h) was obtained from a mass ratio of 1.5:1 TiO₂/polymer.

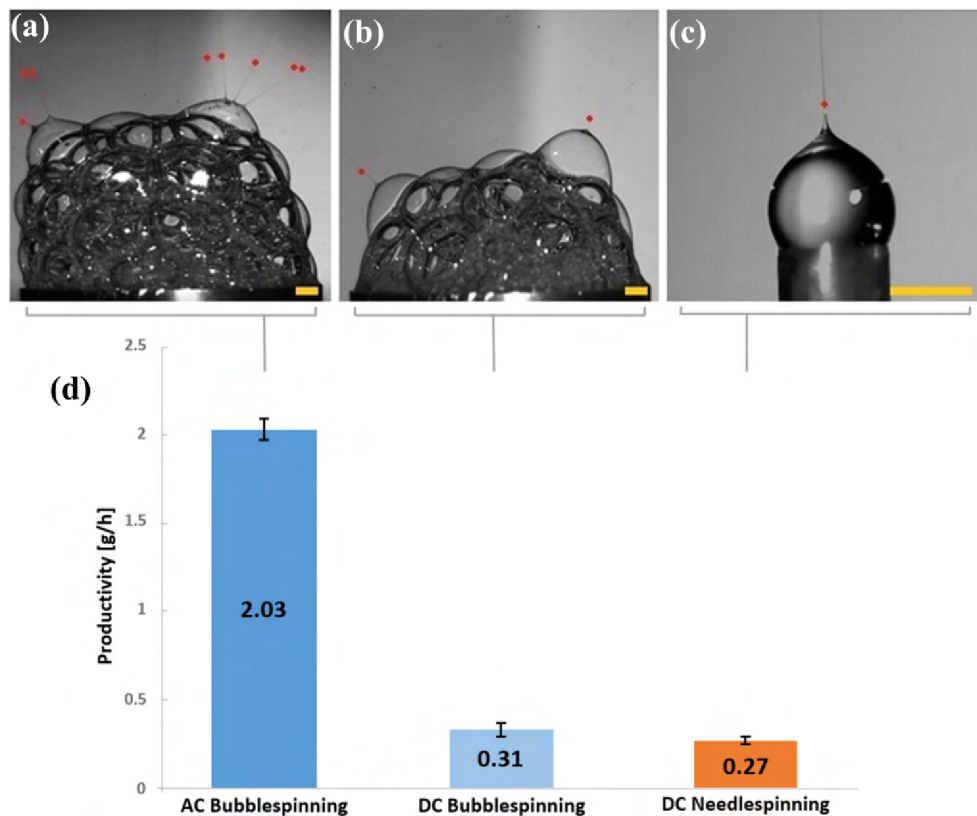


Figure 2.11: (a) High-speed camera images of the Taylor cone and subsequent straight segment of the jet (red dots) during the process of AC electrospinning (a), DC electrospinning (b), needle DC electrospinning, and their nanofiber productivities (d). Scale bar is 1 mm. [60].

Additionally, AC high voltage was also used in free surface bubble electrospinning Fig. 2.11. Bubbles were created on its surface by forcing the air into the liquid solution. This implies already liquid surface has been disturbed. Subsequently, a higher degree of surface disruption was obtained when applying a high voltage. This surface disruption encourages the formation of more jets. The experiment results showed that the productivity of electrospun PVA nanofibers using AC bubble electrospinning is much higher than conventional DC bubble electrospinning at 2.0 g/h and 0.3 g/h, respectively. The diameter of the fibers produced by AC bubble electrospinning is slightly lower than that of DC bubble electrospinning. Given similar fiber quality, the performance of AC bubble electrospinning is better than DC bubble electrospinning [60].

2.6 Surface plasma treatment

Plasma is defined as a partially ionized but almost neutral (quasi-neutral) gaseous mixture of ions, free electrons, radicals, photons, and neutral particles (i.e., atoms and molecules). It is generally produced by the excitement of the surrounding gas in the electric field. Depending on the thermal equilibrium state, plasma can be further classified into two different categories: thermal or equilibrium and non-thermal or non-equilibrium plasma. In the case of a thermal plasma, ions, free electrons, radicals, photons, and neutral particles have the same temperature. On the other hand, in non-equilibrium (cold) plasma, the temperature of these species is not in equilibrium. Non-equilibrium plasma is generally generated in the presence of a strong electric or magnetic field, where the relative velocity of the electrons is much higher than the ions's velocity. Consequently, it reflects in the creation of plasma at considerably lower gas temperature, which makes this plasma a suitable candidate for the surface modification of thermally sensitive materials, for instance, electrospun nanofibrous materials.

Plasma can be generated using a wide range of methods, such as Dielectric barrier discharges (DBD), radio frequency discharges, and microwave discharges. However, in the case of electrospun nanofibrous, a DBD reactor is often used [40]. The experimental settings are discussed in sub-chapter 3.2.7 on page 45. The dielectric bi-layer makes the homogeneous charge distribution across the electrodes; as a consequence, the formation of micro-discharge is encouraged rather than single arc discharges. Vicinity of the micro-discharge, the ionization of supplied gas occurs owing to the acceleration of electrons from the cathode to the anode. The collisions between the accelerating electron and the surrounding gas continuously produce the ions, thereby making the sustaining plasma .

Plasma activation

When the polymeric material is exposed to a plasma discharge, the polar or non-polar functional groups will be introduced on the material's surface. For instance, polar functional groups will be introduced on the material's surface as follows: due to the uniform bombardment of plasma-generated reactive species to the surface, weak surface bonds (e.g., C-H/C-O) present in the polymeric chains are broken, resulting in the generation of surface radicals. These radicals, however, rapidly react with the reactive plasma species present in the discharge gas (i.e., argon or nitrogen) resulting in the formation of polar surface groups (e.g., C=O, O=C-O, C-N, C=N, and N-C=O). The type of incorporated polar functional groups, however strongly depends on the used working gas [22, 40, 82]. Similarly, non-polar fluorine-containing groups can be grafted by using fluorine-containing discharge gas (Carbon tetrafluoride or Sulphur hexafluoride) [83]. As a consequence, increased surface hydrophobicity of the material will be obtained [40]. If polar groups are incorporated on the polymeric material's surface, its surface energy and hydrophilicity will be improved significantly. In contrast, hydrophobicity will be increased if non-polar groups are incorporated on the material's surface.

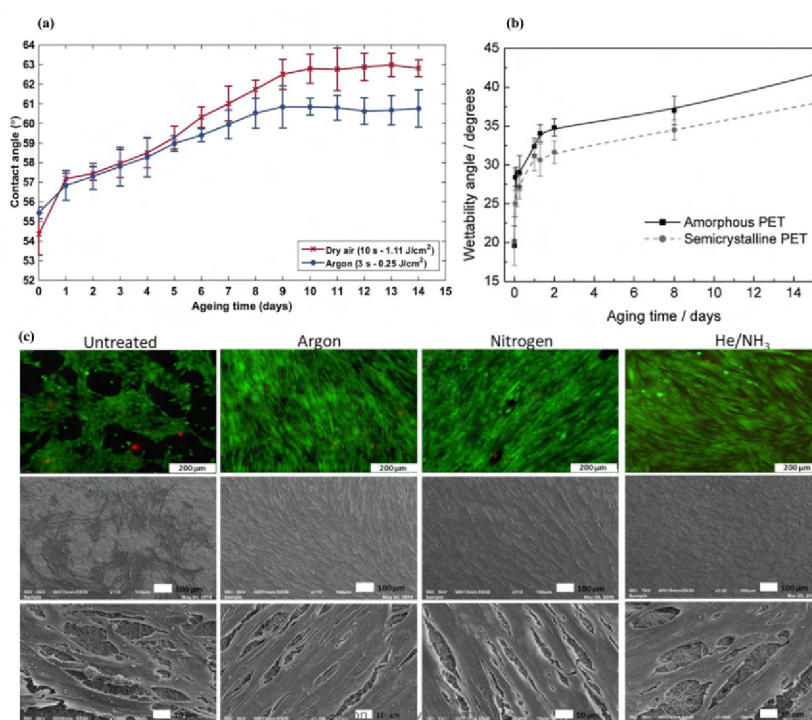


Figure 2.12: (a) poly(ethylene terephthalate) and (b) PCL foil's hydrophobic recovery as a function of aging time [84, 85], and (c) human foreskin fibroblasts cells were cultured on untreated and plasma-treated materials, and at 7 days after seeding, fluorescence pictures and SEM micrographs were taken [40].

It is worth saying that the plasma-induced surface chemical changes were not permanent since, over time, the incorporated functional groups tend to reorient towards the material's bulk to form an energetically stable or desirable state, so-called aging effects or partial hydrophobic recovery (as shown in Fig. 2.12a and b). In addition, a high-energy surface of the plasma-treated material tends to adsorb species from the ambient air to decrease its surface energy. In the case of electrospun nanofibers, hydrophobic recovery was less pronounced than in films. This could be attributed to the following fact: since all the electrospun fibers are intertwined with each other, there is a minimal chance of reaction between the ambient air and the fibrous surface than in foil or non-porous materials. Fig 2.12c, which includes live/dead fluorescence images and SEM micrographs taken seven day after seeding, clearly shows that cells adhere poorly to untreated PCL NFs and that adherent cell aggregates/clusters are prominent on the surface. The cells spread much more in the plasma-modified PCL samples and have the spindle-shaped morphology seen in healthy fibroblasts.

Currently available literature, in most cases, studies the effects of plasma treatments on morphology and their wettability as well as surface chemistry. However, the degree of crystallinity is one of the key parameters controlling the degradation and mechanical properties of semi-crystalline polymers like PCL. To study the importance of the degree of crystallinity, Junkar *et al.* [84] and Kim *et al.* [86] modified a polyethylene terephthalate (PET) foil with an oxygen plasma and concluded that crystallinity plays a major role in reducing the post-plasma aging effect and hydrophobic recovery rate. Besides, Helen *et al.*[87] demonstrated the significant role of crystallinity on cell response to poly(caprolactone-co-glycolide) by revealing that fibroblast like-cells are more likely to attach and proliferate on crystalline surfaces. Despite its potential impact on the bulk properties, plasma aging rate, hydrophobic recovery, and cell response, the effects of plasma treatment on PCL ENMs crystallinity are rarely investigated. Consequently, it is clear that just studying the plasma treatment effects on fiber morphology, wettability, and surface chemistry are not sufficient for understanding the cellular response to ENM surfaces, for which crystallinity should be addressed as well. To the best of the authors knowledge, for the first time, plasma treatment effects on the bulk properties of AC spun PCL is studied and discussed in sub-chapter 4.3 on page 87.

Chapter 3

Materials and Methodology

The aim of this chapter is to provide the reader with a clear overview of the materials and the strategic methodology used to achieve the aim of the PhD dissertation.

3.1 Materials

Granular polycaprolactone (number averaged molecular weight $M_n = 80$ kDa) was purchased from Sigma Aldrich. Analytical grade formic acid, acetic acid, and acetone were obtained from Penta chemicals. Materials for cytotoxicity and in vitro studies, such as Dulbecco's modified Eagle medium (DMEM), 3-(4,5-Dimethylthiazol-2-yl)-2,5-Diphenyltetrazolium Bromide (MTT), bovine serum albumin (BSA), Triton-X-100, phalloidin-fluorescein isothiocyanate, and 4',6-diamidino-2-phenylindole (DAPI) were also purchased from Sigma Aldrich.

3.2 Methodology

Details on the methodology consisting of solubility parameters theory, spinning solution preparation, AC electrospinning setup, and morphological and physicochemical characterization techniques are presented in this sub-chapter. In addition, this sub-chapter also includes biocompatibility and in vitro experiments.

3.2.1 Solubility parameter: Theory

The primary step of electrospinning is to identify the suitable solvent or solvent blend to prepare the ideal spinning solution. Based on the Hansen solubility theory, the better solvent or solvent blend for studying the AC spinnability of PCL was identified. The theory of solubility parameter is explained here.

A molecule in the liquid can be removed or evaporated when it acquires adequate energy to overcome the cohesive energy (or the liquid-phase inter-molecular forces) of the neighboring molecules. The enthalpy of evaporation reflects the energy required to evaporate the molecule from the liquid, which can be experimentally measured. This energy is directly related to the molecule's cohesive energy density (CED). The square root of the CED per molar volume is known as the total solubility parameter in \sqrt{MPa} (i.e., Hildebrand solubility parameter),

$$\delta_t = \sqrt{CED} = \sqrt{\frac{-U}{V_m}} = \sqrt{\frac{\Delta H_{vap} - RT}{V_m}}, \quad (3.1)$$

where U is the internal energy of system, ΔH_{vap} is the enthalpy of vaporization, R is the universal gas constant ($R = 8.3145 \text{ J/mol K}$), V_m is the molar volume, and T is the absolute temperature. Numerical value of δ_t provides information about the degree of interaction between two or more materials. For instance, a similar δ_t value of polymer and solvent makes a homogeneous solution upon mixing. Later on, Hansen found that one dimensional δ_t can be split into three independent components based on fundamental intermolecular interactions, whose geometric sum is also called the total solubility parameter [88, 89],

$$\delta_t = \sqrt{\delta_d^2 + \delta_p^2 + \delta_h^2}, \quad (3.2)$$

where δ_d , δ_p , and δ_h represent solubility parameters of the dispersion force, polar force, and hydrogen-bonding force, respectively. In contrast to the one-dimensional Hildebrand solubility parameter, Hansen used δ_d , δ_p , and δ_h as an orthogonal axis coordinate to construct the 3D solubility space for predicting the miscibility of the materials. The distance between the solvent and the polymer in the Hansen space has been estimated according to the following equation:

$$D = [4(\delta_{dp} - \delta_{ds})^2 + (\delta_{pp} - \delta_{ps})^2 + (\delta_{hp} - \delta_{hs})^2]^{1/2} \quad (3.3)$$

where δ_{xp} and δ_{xs} are Hansen component parameters for the polymer and solvent, respectively. Furthermore, the ratio between the polymer–solvent solubility distance and the polymer’s interaction radius of the Hansen sphere, D/R_a , provide their relative energy dispersion (RED), which reflects the affinity between the polymer and the solvent. The solubility parameters and an interaction radius value of PCL ($R_a=5.5$) are taken from the literature [89] and R_a is corresponding to the molecular weight of PCL 65 kDa. For $RED < 1$, high affinity between polymer and solvent, and for $RED > 1$, progressively lower affinity between polymer and solvent. The results of this study are presented in Chapter 4.1.2 on page 58.

Flory and Huggins developed another approach to understanding polymer solubility and explained the polymer solution’s non-ideal character. The Flory-Huggins parameter χ was included in the definition of the mixing enthalpy and has the following relationship to the solubility parameters of two substances:

$$\chi_{12} = \frac{V_M}{RT}(\delta_1 - \delta_2)^2 \quad (3.4)$$

where δ_1 and δ_2 are the total solubility parameter of the correspond polymer and solvent system, respectively. V_M , R and T are molar volume of the solvent, universal gas constant, and absolute temperature, respectively. In general, a solvent is thought to be a good solvent for the polymer when χ_{12} is less than 0.5, and a poor solvent when χ_{12} is greater than 0.5.

3.2.2 Precursor solution preparation

For reader quick view, the spinning solution which was used in this dissertation is listed in Table 3.1 and also explained in the following paragraphs.

Table 3.1: *Summary of prepared polymeric solutions with respect to their sub-chapter number.*

Sub-chapter number	Polymer	Solvent	Polymer concentration [wt%]
4.1	PCL	Formic acid	5, 10, 15, and 20
		Formic acid+acetic acid	
		Formic acid+acetic acid+acetone	
4.2	PCL	Formic acid+acetic acid+acetone	10
4.3	PCL	Formic acid	10
		Formic acid+acetic acid	
		Formic acid+acetic acid+acetone	

Precursor solution preparation for studying the PCL's AC spinnability

To evaluate the AC spinnability of PCL as a function of various solvents and polymer concentrations, 12 types of polymeric solutions were prepared by dissolving the PCL pellets (5, 10, 15, 20 wt%) into of formic acid (F-PCL), formic acid/acetic acid (1:1 v/v) (FA-PCL), and formic acid, acetic acid and acetone (1:1:1 v/v/v) (FAA-PCL). These solutions (F-PCL, FA-PCL, and FAA-PCL) were stirred overnight at room temperature to ensure the complete dissolution of PCL pellets.

Spinning solution preparation for analyzing the impact of waveform and frequency of AC high voltage on PCL's spinnability.

In order to study the effects of various waveform and frequencies of the high voltage signal on the spinnability, 10 wt % of PCL precursor solution was prepared by dissolving PCL pellets in a mixture of acetic acid/formic acid/acetone (1/1/1 v/v) (FAA-PCL). The attainment of a homogeneous PCL solution involved thorough mixing using a magnetic stirrer overnight at ambient temperature.

Precursor solution preparation for investigating the plasma treatment effects on the PCL nanofiber's bulk properties

For analysing plasma treatment effects on the AC spun PCL electrospun nanofibers, three types of polymeric solutions were prepared by dissolving the PCL pellets in formic acid (F-PCL), formic acid/acetic acid (1:1 v/v) (FA-PCL), and formic acid/acetic acid/acetone (1:1:1 v/v/v) (FAA-PCL) to prepare 10 wt% solutions of PCL. These solutions were stirred overnight at room temperature to obtain a complete dissolution of the PCL pellets.

3.2.3 Analysis of viscosity and surface tension of the various PCL solutions

Although F, FA, and FAA solvent systems have low toxic potential and are capable of producing ultrathin electrospun fibers, these solvents promote the acid-catalyzed degradation of PCL's ester bonds [90]. Therefore, to avoid the degradation of PCL, the precursor solutions were analyzed 13 hours after solution preparation time (dissolution time counted) in terms of their viscosity, surface tension, and AC electrospinnability.

The viscosity was determined using a HAAKE 172 RotoVisco 1 viscometer (Thermo Scientific - USA). The viscosity values of F-PCL, FA-PCL, and FAA-PCL (volume: 200 μL) were measured for the time period of 120 s at the shear rate range of 500–750 s^{-1} as a function of various PCL concentrations (5, 10, 15 and 20 wt%). Surface tension of these solutions were measured using a K12 tensiometer (Kruss GmbH) by the Wilhelmy plate method. Prior to each measurement, the rectangular platinum plate was flame dried. The stated viscosity and surface tension values correspond to the average of 5 and 3 measurements per sample, respectively. The surface tension and viscosity of various precursor solution is reported in sub-chapter 4.1.4 (Fig. 4.4 on page 62 and Fig. 4.5 on page 63).

3.2.4 Analysis of PCL stability in various solvents

In order to studying the PCL stability in various solvents (carboxylic acids) in terms of PCL's molecular weight and the viscosity of PCL solutions, gel permeation chromatography (GPC) and viscometer were used. At the first step, 10 wt% F-PCL, FA-PCL, and FAA-PCL solutions were prepared in two containers as mentioned in the previous section. After the complete dissolution (13 hours, with dissolution time counted), one container from each solution (F-PCL, FA-PCL, and FAA-PCL) was kept in the room temperature and the remaining one was kept in the fridge at 2 $^{\circ}\text{C}$ for at least 216 hours. To study the PCL stability as a function of time in addition to the solvent system and storage condition, the desired amount of samples were taken for GPC and viscosity analysis at specific time intervals after the complete PCL dissolution (24, 48, 72, 144, 216 hours).

GPC was used to monitor the changes in PCL molecular weight over time after the complete PCL dissolution (24, 48, 72, 144, 216 hours) in F, FA, and FAA solvents during the solution stability experiments (while storing the F-PCL, FA-PCL, and FAA-PCL at room temperature and in the fridge at 2 $^{\circ}\text{C}$). A Dionex Ultimate 3000 HPLC chromatograph equipped with a diode array detector, Varian LC-385 ELSD detector, and Agilent 1260 MDS LALS/RALS detector was used for the determination. The temperature of the ELSD nebulizer and the evaporator were both set to 80 $^{\circ}\text{C}$. Nitrogen was used as the drying gas with a flow rate of 1.3 L/min. The chromatogram of each sample was recorded at 220 nm by the DAD and also by the ELSD and RALS/LALS detectors for 14 minutes. A Phenomenex Phenogel 1E5 polystyrene resin gel permeation column with a length of 30 cm, i. d. of 7.8 mm and 5 μm particle size was used. Pure HPLC grade tetrahydrofuran was used as the mobile phase. A flow rate of 1 mL/min was chosen. The column compartment temperature was set to 35 $^{\circ}\text{C}$, and 30 μL of samples, filtered through a 13 mm diameter nylon syringe filter with a pore size of 0.45 μm , were injected.

At the same time, for studying the stability of PCL in the F, FA, and FAA solvent system, the viscosity of F-PCL, FA-PCL, and FAA-PCL was also analyzed over time (24, 48, 72, 144, 216 hours). As a consequence of acid-catalyzed hydrolysis, the molecular weight of PCL in F-PCL, FA-PCL, and FAA-PCL solutions reduces over time. Thus reflected as the reduction in the viscosity over time as well. Hence, viscosity of these solutions were determined also using a HAAKE RotoVisco 1 viscometer (Thermo Scientific – USA). The stability of PCL in various solvents with respect to various solvent system is discussed in Chapter 4.1.3 (Fig. 4.3 on page 61).

3.2.5 AC electrospinning

Fabrication of the PCL ENMs was carried out using needleless and collectorless AC electrospinning at an applied effective high voltage of 35 kV_{RMS} . The AC electrospinning set-up, shown in Fig. 3.1, was assembled using the following components: a grounded KGUG 36 high-voltage transformer with a conversion ratio of $36000\text{V}/230\text{V}$, an ESS 104 variable autotransformer for controlling the output voltage, a Thalheimer Transformatorwerke used for a 230 V AC input and an output of 0 - 250 V and a rod spinning electrode coupled to a polymer solution reservoir.

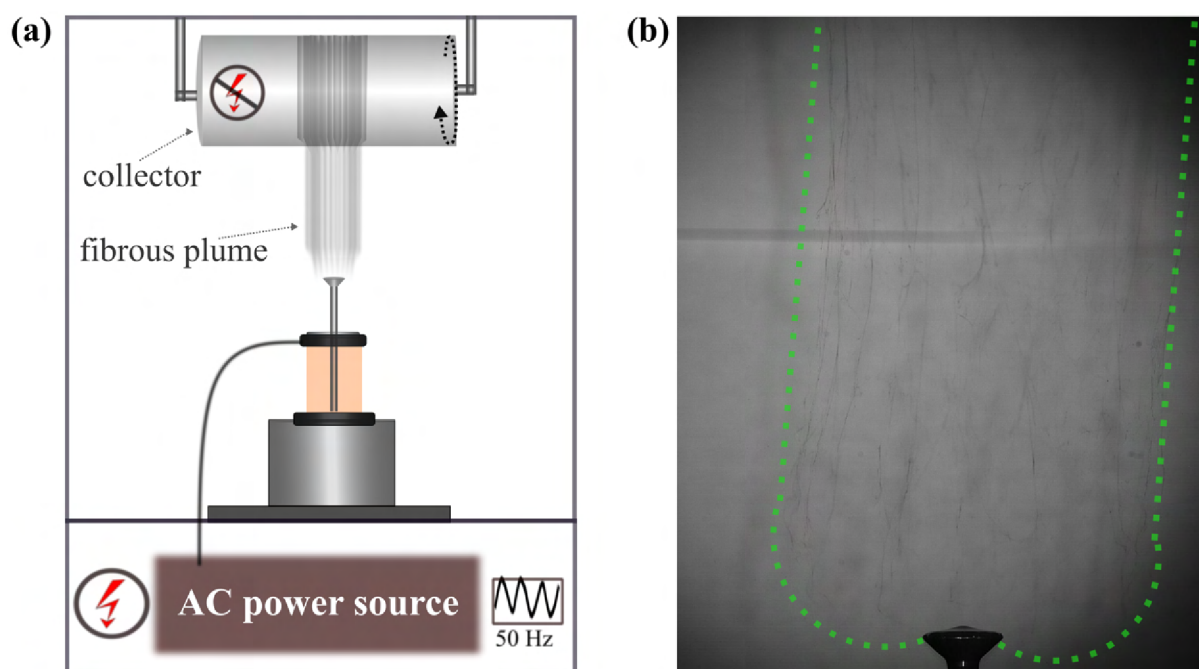


Figure 3.1: Schematic representation of AC electrospinning (a) and picture of the nanofibrous plume (b).

The maximum output current was 4 A with a capacity of 1.2 kVA. This AC power supply operated at 50 Hz at an effective voltage of up to a maximum of 35 kV_{RMS}. The rod spinning electrode (length: 100 mm & spinning head Ø: 20 mm) was coupled to a polymer solution hopper with a screw pump (Technical University of Liberec – Czech Republic). The screw pump delivers the polymer solution to the surface of the spinning electrode head through a coaxial channel, in which the polymer jets emerge. Generated fibers were collected on the rotating cylinder. The excess solution then flows down the outer surface of the electrode back into the polymer solution reservoir which is to ensure the continuous process of AC electrospinning and to wipe out deposited fragments of solid nanofibers on the electrode to the reservoir. The infusion rate of the pumped solution is 18 mL/min at the frequency (speed of screw pump) of 500 rpm for all experiments. The entire work was done using this technology according to specific objectives.

3.2.6 AC high-voltage signal generator and amplifier connections to the spinneret

A signal generator (Won AG 1022) connected to a high-voltage amplifier (TREK 50/12C-H-CE) was used to generate the required AC high voltage in tunable waveforms and frequencies (Fig. 3.2). The output of the waveform generator (0 to ±10V) was connected to the signal amplifier (output range of -50 kV to +50 kV and an amplification factor of 5000V/1V). The output of the signal amplifier was then connected to the spinning electrode. The experiment considered square, sine and triangle waveforms (as shown Fig. 2.4a) over a frequency range of 10 – 60 Hz with an applied effective AC voltage of 50 kV. Details of the AC spinning setup are available in Valtera *et al.* [24]. Briefly, the high voltage was connected to the electrode, which was coupled with a screw pump and the solution container. The screw pump served to assist the feeding of the polymeric solution to the surface of the spinneret at a constant and controlled rate. The rotation speed of the screw pump was maintained in the range 400 – 500 RPM in order to ensure the delivery of 14 – 18 mL/m of the solution to the surface of the spinneret (diameter: 25 mm) according to the various waveforms and frequencies of the AC voltage. The steady fibrous plume that emerged was collected on a spun-bond fabric (polypropylene), which was attached to a rotating drum (an electrically-inactive collector). The peripheral speed of the collector was maintained at 30 – 40 m/min. The results of this experiment are discussed in Chapter 4.2 on page 75.

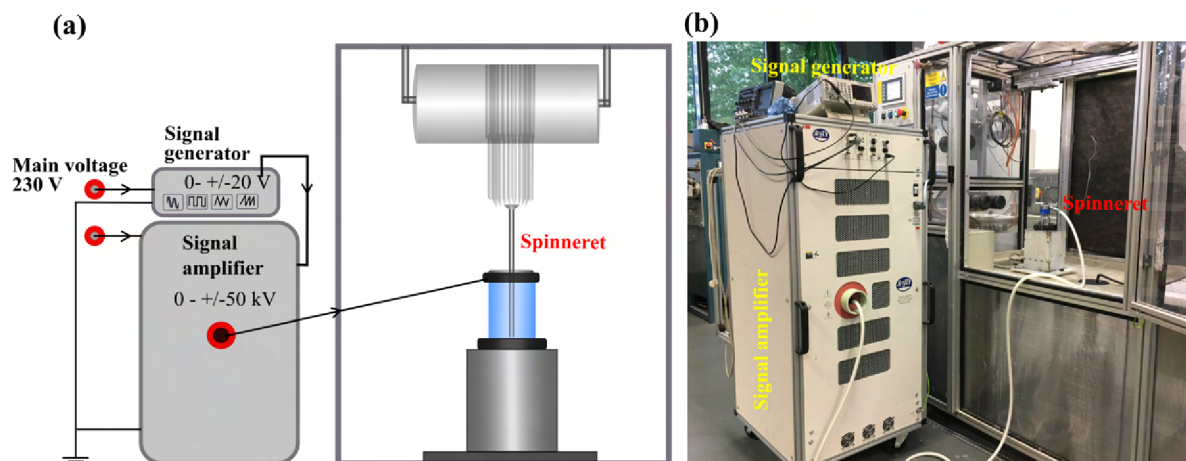


Figure 3.2: Schematic illustration (a) and pictorial representation (b) of the AC high-voltage signal generator (Won AG 1022) and amplifier (TREK) connected to the spinneret.

3.2.7 Dielectric barrier discharge (DBD) reactor

This DBD experiments were conducted during the author's internship stay in Ghent University, Belgium. The DBD reactor mainly consisted of 2 electrodes, 2 dielectric layers, and a high voltage power supply. Two circular electrodes made of copper and having a diameter of 55 mm were both covered with a quartz glass plate (permittivity: 3.75 at 20 °C). The upper electrode was connected to a 50 kHz AC high voltage source, while the lower electrode was grounded through a capacitor C (10 nF). The gas gap between the 2 glass plates was fixed at 35 mm for all conducted experiments, and the plasma discharge area was approximately 23.75 cm². The flow rate of the discharge gas flowing between the glass plates was controlled by a digital mass flow controller (Bronkhorst).

A schematic configuration of the experimental DBD set-up is presented in Fig. 3.3, and more information can be found in Cools *et al* [91]. To perform the plasma treatment, the ENM was first fixed on the lower glass plate, and the plasma reactor was pumped down to 0.05 kPa using a rotary vane pump. Subsequently, the reactor was filled with the discharge gas at a rate of 3 standard liters per minute (slm). After reaching a reactor pressure of 50 kPa, the reactor was flushed at 3 slm with the working gas for 4 minutes to remove residual gases and to obtain a reproducible gas composition. These procedures were repeated before plasma ignition for each sample under study. After the purging step, the working gas flow rate was fixed to 1 slm, and the reactor pressure was reduced to 5 kPa. At this medium pressure, plasma treatment was performed using argon and nitrogen gases at a pre-selected discharge power resulting into a visually stable plasma discharge. The exact values of the applied discharge powers were calculated from voltage-

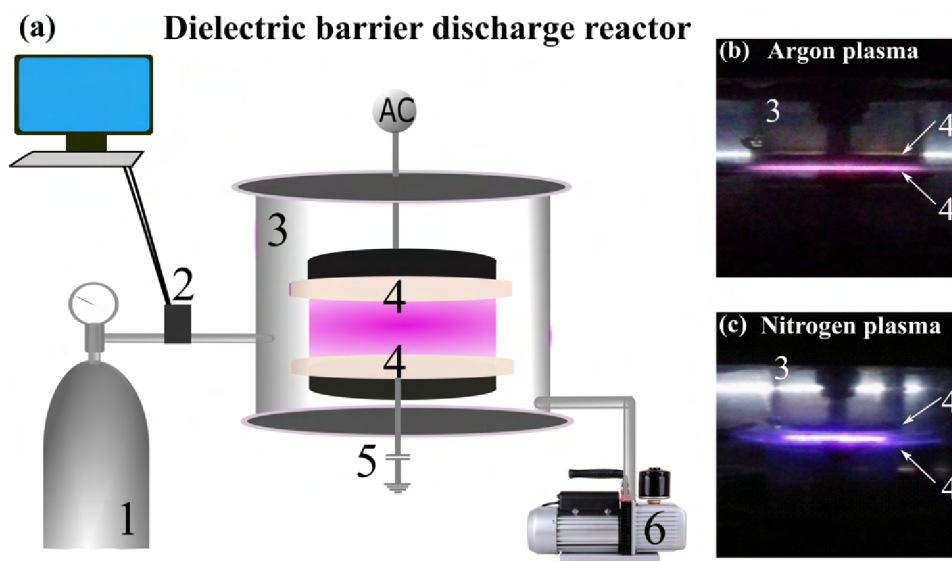


Figure 3.3: (a) Schematic and pictorial representation of the DBD reactor (1. gas cylinder, 2. mass flow controller, 3. plasma chamber, 4. dielectric barrier, 5. capacitor, and 6. rotary vane pump), (b), and (c) images of the argon and nitrogen plasma. (This image is featured on the cover page of the journal ‘Surface and Coatings Technology’2020, 399)

charge plots (so-called Lissajous figures) [92]. As Ar and N_2 plasma treatments required slightly different discharge powers for a stable plasma generation, results will be presented as a function of energy density instead of plasma exposure time to enable an objective comparison. The energy density was calculated by multiplying the exposure time with the discharge power and then dividing this value by the area of the circular electrodes. An overview of the performed plasma treatment conditions for each PCL ENM under study is presented in Table 3.2. The outcomes of this experiment are discussed in Chapter 4.3 on page 87.

Table 3.2: Used experimental plasma treatment parameters for PCL ENSs.

Sample	Discharge gas	Discharge power	Treatment time	Energy density
		[W]	[s]	[J/cm ²]
F-PCL	Argon	2.2	65	6.0
F-PCL	Nitrogen	2.6	63	6.9
FA-PCL	Argon	2.2	55	5.1
FA-PCL	Nitrogen	2.6	64	7.0
FAA-PCL	Argon	2.2	60	5.6
FAA-PCL	Nitrogen	2.6	61	6.7

3.2.8 Productivity analysis

The nanofiber productivity was measured via the gravimetric method using a Sartorius analytic weighing machine to study the impacts of the various solvent systems (F, FA, and FAA), AC high-voltages (25 and 32 kV), waveforms (square, sine, and triangle) and frequencies (10-60Hz) of AC high-voltage signal on the productivity of electrospun fibers. Prior to the weighing of the PCL ENF, all the samples were left in an open space for 24 h at room temperature so as to ensure the removal of the residual solvents. Three measurements were carried out for each sample, and the mean value was presented as final productivity. This results have been presented in sub–hapter 4.1.6 on page 68 (Fig. 4.8 on page 69) and sub–chapter 4.2.4 on page 84 (Fig. 4.16 on page 84).

3.2.9 Scanning electron microscopy

To evaluate the effects of various solvent systems (F, FA, and FAA), AC high voltage (25 and 32 kV), various AC high-voltage’s waveforms (square, sine, and triangle) as well as frequency (10 to 60 Hz) and various plasma treatments (argon and nitrogen plasma treatments) on the morphology and fiber diameter of the PCL electrospun nanofibers, a Vega S3B Easy Probe (Tescan, Czech Republic) scanning electron microscopy (SEM) and ImageJ software (NIH, USA), respectively, were used to visualize and measure them. At first, all the PCL electrospun nanofibers were sputter-coated with a thin layer of gold using Quorum (Q150R ES) sputter coater. Then the SEM micrographs of F-PCL, FA-PCL, and FAA-PCL were acquired in high vacuum at an accelerating voltage of 20 kV. From each sample’s micrographs, the mean diameter of electrospun nanofibers was measured ($n = 200$). The SEM images of various PCL electrospun fibers is exhibited in Fig. 4.6 on page 65, Fig. 4.13 on page 79, 4.14 on page 81, and 4.19 on page 90.

3.2.10 Analysis of pore size and porosity

The pore size and porosity of various ENSs were analyzed using the stereological method and the Masounave approach [93–95]. To analyze the pore size and porosity, the ENSs were frozen with liquid nitrogen and then cut crosswise to obtain good quality cross-sections of the nanofibers (Fig. 3.4). Instead of cutting the samples at room temperature, it was soaked in liquid nitrogen for at least 2 minutes, and then crosswise cutting was performed. Since PCL has glass transition temperature and melting temperatures at $-60\text{ }^{\circ}\text{C}$ and $60\text{ }^{\circ}\text{C}$, respectively, it transforms into a brittle state after soaking in the

liquid nitrogen ($-196\text{ }^{\circ}\text{C}$). Subsequently, the frozen ENM was dissected crosswise using a surgical knife (also soaked in liquid nitrogen) which ensures the perfect crosswise cutting of nanofibers. Three SEM images from each sample were used to analyze the pore size and porosity of the ENS.

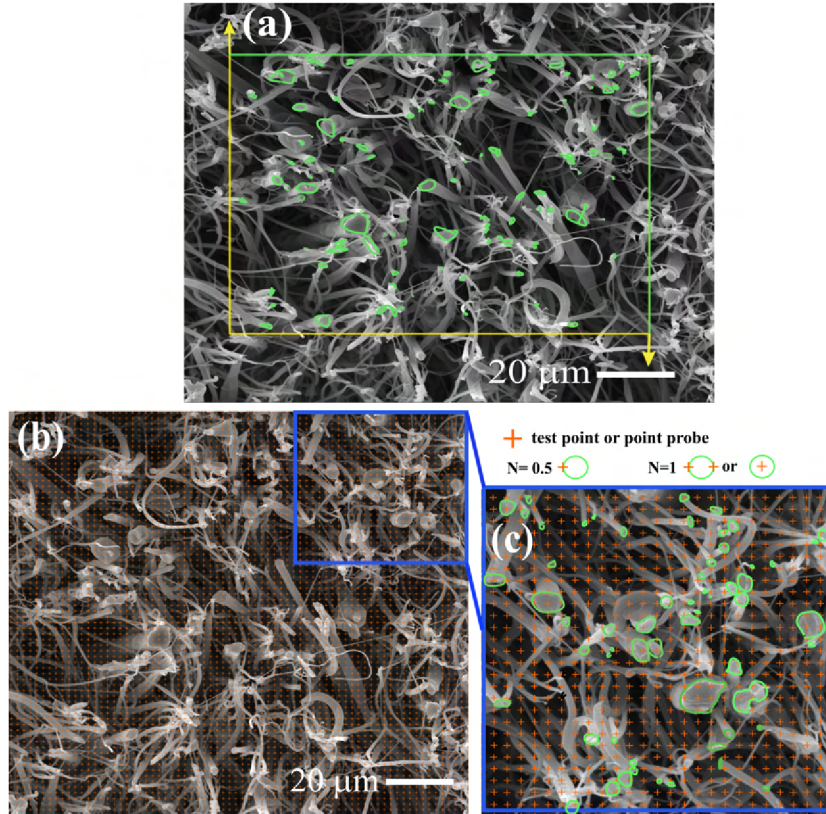


Figure 3.4: *Model of the cross-sectional image of nanofibers for analyzing the pore size and porosity of ENS. (a) Model SEM image for analyzing the pore size (yellow and green lines are exclusion and inclusion lines, respectively. Green circles represent the cross-sections of the electrospun nanofibers.), (b), and (c) SEM image with test point grid or point probe (+) for estimating the porosity of ENSs (for the readers better view, cross-sections of electrospun nanofibers are highlighted in green).*

In the first step, an unbiased counting frame was drawn on the SEM image, which contains two inclusion lines (green) and two exclusion (yellow) lines (Fig. 3.4a). The number of fiber cross-sections (N) is counted when they are within the unbiased counting frame or sampling area (S). The fiber cross-sections are also counted when they are touching the inclusion line and not counted when they are touching the exclusion lines. This method ensures that if two counting frames are placed side by side on a sampling image, the fiber cross-section will only be counted once. The numerical area density ($N_S = N/S$) of the nanofiber cross-sections was then found as a ratio of these values. The probability density of pore radius (r_p) and mean value of pore radius (r_s) were obtained by substituting the

value of N_S in the following equations [93]:

$$r_p = \frac{1}{\sqrt{2\pi N_s}}. \quad (3.5)$$

$$r_s = \sqrt{\frac{\ln 2}{\pi N_s}}. \quad (3.6)$$

Likewise, the porosity of the ENSs was also analyzed manually by the point-counting stereological method (uniform random sampling). As shown in Fig. 3.4b and 3.4c, a grid of points (testing system with point probes) was superimposed on the SEM image of the ENSs, followed by the calculation of the total number of points on the surface area of the sampling image (N_c). The number of points falling exclusively on the nanofiber cross-sections in the sampling area was also counted (N_a). Then the porosity of ENSs was calculated using the following equation:

$$Porosity = \left(1 - \frac{N_a}{N_c}\right) \times 100\%. \quad (3.7)$$

The mean value of pore and the porosity of various PCL ENMs are exhibited in Fig. 4.11 on page 73. Additionally, the probability density of pore radius is depicted in Fig. A.2 on page 105.

3.2.11 Analysis of number of beads and/or spindles

The stereological method (uniform random sampling) was used for the counting of the beads and/or spindles per unitary fiber length (N_L) [96]. As shown in Fig. 3.5, four identical lines (stereological probe) were drawn on the SEM image, followed by the calculation of the number of fibers that intercepted or passed through each line. The number of fiber intercepts (N) divided by the total length of the line (L) and multiplied by $\pi/2$ gave the normalized geometric count ($L_A = \pi N/2L$). The number of beads and/or spindles were also counted, followed by the calculation of the amounts thereof divided by the area of the sampling image (N_A). The total length of the line and the area of the sampling images were identical for all the images (Table 3.3). The number of intersects, beads and spindles were thus quantified for each sample (at least two images). The beads and/or spindles

per unitary fiber length (N_L) were analyzed via the following equation [96],

$$N_L = \frac{N_A}{L_A}, \quad (3.8)$$

Where, (N_A)=(number of beads and (or) spindles)/(area of the specimen) and (L_A)=((number of fiber intersects)/(total length of the line)) $\times \pi/2$. Outcomes of this analysis can be seen in sub-chapter 4.2.3.

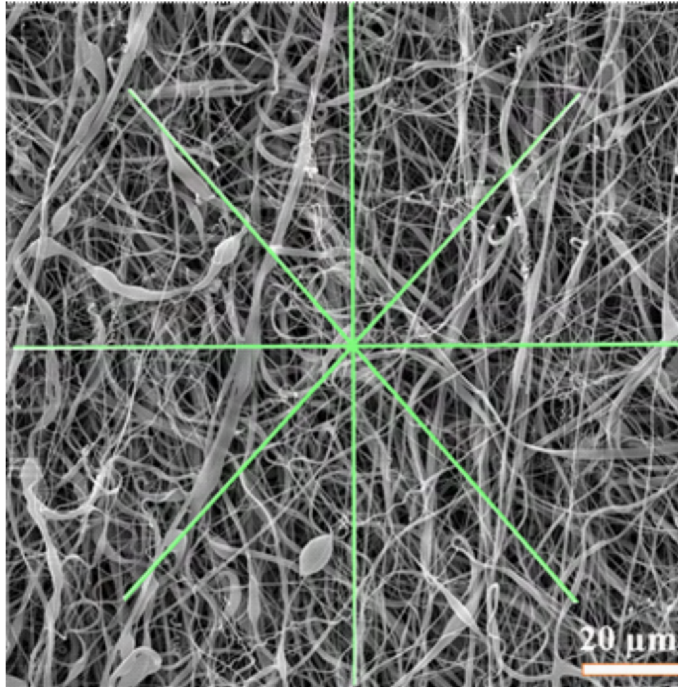


Figure 3.5: Model of a probe arrangement for the estimation of fiber/line intercepts.

Table 3.3: Total length of the probe and the sampling area of the image.

Number of lines	4
Length of the line	138 μm
Total length of the line	$4 \times 138 \mu\text{m} = 552 \mu\text{m}$
Area	$76176 \mu\text{m}^2$

3.2.12 Water contact angle analysis

The surface wettability of the PCL ENMs was analyzed at room temperature using a commercial Krüss Easy Drop system within 5 minutes after plasma treatment. Droplets of deionized water with a volume of 2 μL were placed at 5 randomly selected locations on each electrospun material. In the next step, the WCA values were obtained using the Laplace-Young curve fitting of the recorded images of the water drop profiles, and an

average WCA value was calculated and presented in Chapter 4.3.2 on page 88 (Fig. 4.18 on page 89).

3.2.13 X-ray photoelectron spectroscopy

The surface chemical composition and the nature of the surface functional groups of the PCL ENMs were determined using XPS. XPS analysis was executed on a PHI 5000 Versaprobe II system equipped with a monochromatic Al K_{α} X-ray source ($h\nu = 1486.6$ eV) operated at a power of 23.3 W. Pressure was maintained below 10^{-6} Pa in the high vacuum main chamber for all conducted measurements. The emitted photoelectrons were analyzed with the help of a hemispherical analyzer positioned at an angle of 45° with respect to the normal of the ENM surface. Survey spectra and high-resolution C1s spectra were recorded on three randomly selected analysis spots per sample using a pass energy of 187.9 eV and 23.5 eV respectively. From the XPS survey spectra, the elemental surface composition of the samples was determined by making use of Multipak (V 9.6.1) software. In addition, the C1s high-resolution spectra were also curve fitted using Multipak software to determine the type of the present surface functional groups. Prior to curve fitting, the binding energy scale was first calibrated with respect to the C-C bond (284.8 eV) of the detailed C1s spectra. In the next step, the calibrated C1s spectra were smoothed using a Savitzky-Golay smoothing procedure, after which a Shirley background was applied. Afterward, the C1s peaks were deconvoluted using Gaussian-Lorentzian shaped components and the full-width at half maximum of each line shape was maintained below 1.8 eV. XPS results is presented in Chapter 4.3.4 on page 91 (Table 4.7 on page 91, Fig. 4.21 on page 93, and Fig. 4.22 on page 94).

3.2.14 X-Ray Diffraction (XRD) characterization of the ENMs

The crystallinity of the PCL electrospun samples was studied using powder XRD (Thermo Scientific ARL X'TRA diffractometer) equipped with a Cu K_{α} ($\lambda = 1.5405\text{\AA}$) source and measuring in the range of 10° to 30° (step size: 0.02°). The integration time was set to 1.200 s and the scan rate was maintained at $1^{\circ} \text{ min}^{-1}$. The full-width at half maximum of the diffraction peaks was calculated by fitting XRD data with a Lorentzian function (Originpro 9 software), and the crystallite size (D) was estimated making use of the Scherrer equation [97]:

$$D = \frac{K\lambda}{\beta \cos \theta}, \quad (3.9)$$

where, K ($K = 0.9$) [98, 99] is the Scherrer constant that depends on lattice direction and crystallite morphology, λ is the X-ray wavelength, β is the full-width at half maximum of the diffraction peak and θ is the Bragg angle. The XRD results can be obtained from Chapter 4.3.5 (Fig. 4.23 on page 95 and Table 4.8 on page 96).

3.2.15 Differential scanning calorimetry analysis

DSC analysis was performed with a Mettler Toledo DSC1 calorimeter from 0 to 80 °C according to the following procedure: heating, followed by cooling, and finally a second heating step. The used heating and cooling rate were set to 5 °C min⁻¹. All experiments were conducted under a nitrogen atmosphere and samples were characterized at least twice. The crystallinity degree (X_c) was calculated from the obtained DSC graphs using the following equation:

$$X_c = \frac{\Delta H_{m1}}{\Delta H_{m1}^0} \times 100\% \quad (3.10)$$

where ΔH_{m1} is the melting enthalpy measured in the 1st heating run and ΔH_{m1}^0 the melting enthalpy of perfect PCL crystals (139.5 J/g) [100]. DSC results are explained in Chapter 4.3.5 on page 95 (Table 4.8 on page 96 and Fig. 4.25 on page 98).

3.2.16 Fourier-transform infrared spectroscopy analysis

Fourier-transform infrared spectra (FTIR) of pristine and plasma-treated PCL ENMs were collected using a Bruker Tensor 27 spectrometer equipped with a single reflection attenuated total reflection (ATR) accessory using a germanium crystal as internal reflection element. FTIR spectra were recorded in the wavenumber region from 3500 to 700 cm⁻¹ using liquid nitrogen cooled MCT (mercury-cadmium-telluride) detector and applying a resolution of 4 cm⁻¹. The outcomes of FTIR results is presented in Chapter 4.2.5 on page 85 (Fig. 4.17 on page 85), and 4.3.5 on page 95 (Fig. 4.24 on page 97).

3.2.17 Sterilization

Prior to sterilization, all the samples were cut into circular shape with a diameter of 1.4 cm. From each material, six samples were prepared; from these, three were washed (twice) with phosphate buffer saline (PBS, Lonza Biotech, Czech Republic), and the rest of them

were used without washing. All these samples were wrapped in a sterilization pouch (Sogeva RB54) and then subjected to an ethylene oxide sterilization at a temperature of 38 °C for 12 hours in an Anprolene AN-74i (Andersen Products) sterilizer. Subsequently, samples were aereated for 2 weeks to get rid of residual ethylene oxide.

3.2.18 Cytotoxicity

Cytotoxicity of F-PCL, FA-PCL, and FAA-PCL was evaluated on cell line 3T3-L1 mouse fibroblasts, which were cultured in Dulbecco's modified Eagle medium (DMEM) enriched with 5% fetal bovine serum (Biosera), 5% newborn culture serum (Sigma), 1% glutamine (Biosera), and 1% antibiotic—Pen / Strep Amphotericin B (Lonza). The cells were incubated in a humidified atmosphere containing 5% CO₂ at a temperature of 37 °C.

First (day 1), 3T3-L1 mouse fibroblast cells (from passage 17) were seeded at a density of 10000 cells/100 μ L in a 96-well plate and cultured for 24 hrs. For preparing the extracts of all samples that were washed in PBS and unwashed, a complete culture medium was added to the 24 well plates, which were preloaded with the sterilized samples, and subsequently incubated for 24 hrs at 37 °C. Next (day 2), the extract from each sample was added (100 μ L/well) to the cell-seeded wells by replacing the culture medium and incubated at 37°C in 5% CO₂ for 24 hrs. The cells in the complete medium (DMEM) were considered as a negative control (NC). In contrast, the addition of Triton-X-100 in the complete medium served as a positive control (PC). The PC and NC were also incubated (37°C in a 5% CO₂ for 24 hrs). Then (day 3), the biocompatibility in terms of cell viability was evaluated by a colorimetric MTT assay. The solution of MTT was added (200 μ L/well) into the DMEM of extract and control samples, which were subsequently incubated for 3 hours at 37°C in the 5% CO₂ environment. Then the MTT solution was removed; subsequently, 200 μ L of IPA (isopropyl alcohol) was added to the cells, and they were incubated for 15 minutes at room temperature. The absorbance of these solutions (10 wells of cells/sample) was assessed at 570 nm (reference was measured at 650 nm) using the Spark multimode microplate reader. The measured UV absorbance value (at the wavelength of 570 nm) of NC was considered as 100% cell viability. A material is considered cytotoxic when its extract exhibits cell viability lower than 70% of the NC. The in cytotoxicity evaluation of electrospun nanofibers is presented in Chapter 4.1.8 on page 71 (Fig. 4.10 on page 72).

3.2.19 In vitro experiment

Besides cytotoxicity evaluation of the materials, the viability and proliferation of 3T3-L1 mouse fibroblast cells (ATCC) were also performed on the F-PCL, FA-PCL, and FAA-PCL ENS. The cells were seeded onto the sterile materials at a density of 10000 cells/mL and subsequently incubated for 1, 3, and 7 days at 37 °C in a 5% CO₂ incubator. The adhesion and the following proliferation of the cells were quantified using the colorimetric MTT assay. In short, 250 μ L of MTT solution (0.2 g/100 mL) and 750 μ L of DMEM were added into each well that was preloaded by the material with the cells, and subsequently, these solutions were incubated in a 5% CO₂ incubator at 37 °C for 3 hrs. After the incubation, the MTT solution was removed and 500 μ L of IPA solution was added and incubated with the materials for 15 minutes at room temperature. Finally, these solutions were transferred to 96 well plates for quantifying the cell adhesion and proliferation by measuring the absorbance value at a wavelength of 570 nm (reference 650 nm) using the Spark multimode microplate reader. For visualizing the morphology of the cells, 3T3-L1 mouse fibroblast cells were fixed with 2.5% glutaraldehyde at the ambient temperature for 10 mins. These samples were washed twice with PBS. The cell membrane permeabilization was done with the 0.1% bovine serum albumin (BSA, Sigma Aldrich) and 0.1% Triton-X-100 in PBS (Sigma Aldrich). After permeabilization and washing, the samples were initially stained with phalloidin-fluorescein isothiocyanate (1 μ g/mL) at room temperature in the dark for 30 mins and subsequently stained by 4',6-diamidino-2-phenylindole (DAPI) solution at ambient temperature for 15 mins followed with PBS wash. The stained samples were stored in the fridge (4 °C) with PBS and used for analysis with a fluorescence microscope (Zeiss, Germany) to investigate the cell morphologies. Fluorescent images were processed in terms of contrast for better visualization. The in vitro evaluation results are presented in Chapter 4.1.8 on page 71 (Fig. 4.11 on page 73).

3.2.20 Statistical analysis

Quantitative data are presented as mean values with standard deviation (SD). The averaged values were determined from at least five independently prepared samples. The results were evaluated statistically using GraphPad Prism 9.1.1. (225). If the data passed the normality test and the test of equality of variances, statistical significance between a pair of groups was determined by the ANOVA test and Tukey's comparative test for post hoc analysis. If the data does not follow a normal distribution, statistical significance between a pair of groups is determined using Dunn's multiple comparisons test for post hoc analysis. Statistical difference between pairs of samples was determined using an unpaired t-test. All results were considered statistically significant for $p < 0.05$. The

value of p represents the probability of obtaining an ‘F’ statistics at least as extreme as that observed when the null hypothesis is true. Statistic ‘F’ means the ratio of two mean squares that forms the basis of a hypothesis test.

Principal component analysis (PCA) is also used to study the AC spinnability of PCL. PCA is a technique used to reduce the dimensionality of large datasets, increasing interpretability while minimizing information loss. It accomplishes this by generating new uncorrelated variables that successively maximize variance. Finding such new variables, the principal components reduces down to an eigenvalue/eigenvector problem. The new variables are defined by the data-set at hand rather than a prior, making PCA an adaptive data analysis technique. It is also adaptable in another way because variants of the technique have been developed that are tailored to various data types and structures. For the PCA, the software R (version 4.1.3) and the package ggfortify (version 0.4.14) were used. The solution properties (polymer–solvent interaction parameter, distance between polymer–solvent in the solubility space, viscosity, and surface tension) and the AC spinnability (fiber diameter at 25 and 35 kV, productivity at 25 and 35 kV, pore size, and porosity of ENSs) were used as variables. The details about this analysis is presented in the Table 3.4. The outcomes of PCA analysis is presented in Section 4.1.7 on page 70 (Fig. 4.9 on page 70).

Table 3.4: *Eigenvalues of the principal component analysis (PCA). This table presents the eigenvalues of each component of the PCA as well as the total variance which is accounted for by each component.*

PC	Eigen values	Proportion of variance	Cumulative proportion
PC1	2.213	0.445	0.44
PC2	1.720	0.269	0.71
PC3	1.220	0.135	0.84
PC4	1.116	0.113	0.96
PC5	0.476	0.020	0.98
PC6	0.295	0.007	0.99
PC7	0.265	0.006	0.99
PC8	0.133	0.001	0.99
PC9	0.060	0.0003	1

Chapter 4

Obtained results

The results of this Chapter 4 are published in the following international peer-reviewed journals:

(1). **Manikandan Sivan**, Divyabharathi Madheswaran, Sarka Hauzerova, Vit Novotny, Vera Hedvicakova, Vera Jencova, Eva Kuzelova Kostakova, Martin Schindler, David Lukas. “*AC electrospinning: impact of high voltage and solvent on the electrospinnability and productivity of polycaprolactone electrospun nanofibrous scaffolds*”

Materials Today Chemistry, 2022, 26, 101025, Impact Factor (2021): 7.61 (Q1)

(2). **Manikandan Sivan**, Divyabharathi Madheswaran, Jan Valtera, Eva Kostakova, David Lukas. “*Alternating current electrospinning: The impacts of various high-voltage signal shapes and frequencies on the spinnability and productivity of polycaprolactone nano fibers*”

Materials & Design, 2022, 213, 110308, Impact Factor (2021): 9.41 (Q1)

(3). **Manikandan Sivan**, Divyabharathi Madheswaran, Mahtab Asadian, Pieter Cools, Monica Thukkaram, Pascal Van Der Voort, Rino Morent, Nathalie De Geyter, David Lukas. “*Plasma treatment effects on bulk properties of polycaprolactone nanofibrous mats fabricated by uncommon AC electrospinning: A comparative study*”

Surface & Coatings Technology, 2020, 399, 126203, Impact Factor (2021): 4.86 (Q1)

4.1 Impact of AC high voltage and solvent systems on the spinnability of PCL electrospun nanofibers

The main objective of this sub-chapter is to fabricate the various PCL ENS for tissue engineering applications using low toxic potential solvents (Class 3) such as formic acid, acetic acid, acetone, and needleless AC electrospinning. To the author's knowledge, this is the first work in which 12 types of PCL solutions have been prepared using mono (F), di (FA), and ternary (FAA) solvent systems for studying the AC spinnability of PCL. Herein, initially, solubility parameters, viscosity, and surface tension of polymeric solutions are studied as a function of various solvent systems and polymer concentrations. Furthermore, PCL stability in the solvent systems in terms of molecular weight is also evaluated. Subsequently, solvents and applied AC voltage effects on the spinnability, morphology, and productivity of PCL nanofiber are discussed in great detail. Lastly, cytotoxicity and in vitro analysis are also examined on the PCL nanofibers.

4.1.1 Experimental conditions

All experimental details can be found in Chapter 3. The parameters that are specifically used in this chapter are summarized in Table 4.1.

Table 4.1: *Various spinning solutions and AC electrospinning processing parameters (F-PCL, FA-PCL and FAA-PCL means PCL dissolved in formic acid (F), formic acid/acetic acid (FA), and formic acid/acetic acid/acetone (FAA), respectively.)*

Precursor solution	F-PCL, FA-PCL and FAA-PCL
Polymer concentration	5, 10, 15, and 20 wt%
AC Electrospinning processing parameter	Spinneret's surface diameter: 2.5 cm Spinneret to collector distance: 22 cm Solution feeding rate: 14 – 18 mL/min Collector's peripheral speed: 40 m/min Applied voltage: 25 and 32 kV _{RMS} Waveform: Sine Frequency: 50 Hz Temperature: 22 – 24 °C Humidity: 40 – 42 %

4.1.2 Analysis of polymer–solvent interactions

The primary step of electrospinning is to prepare the ideal polymeric spinning solution, which depends on the polymer–solvent interactions. In general, a homogeneous polymer solution can be achieved when the solubility parameters of the polymer and solvent are similar. In other words, polymer chains swell and expand in a good solvent due to the better polymer–solvent interactions. Hence, these interactions exert influence on the solvation and the formation of a homogeneous polymer solution. The degree of interaction between the polymer and solvents also affects the chain conformation of the macromolecule [101], which significantly influences the viscoelasticity and the critical solution concentration required for stable electrospinning. From Fig. 4.1 and Table 4.2, it can be seen that FAA is almost close to those of PCL’s Hansen sphere, and its RED value is also smaller than the FA and F. According to the Hildebrand and Hansen solubility parameters, FAA is the good solvent system for PCL, followed by FA and F. In addition, according to the Flory–Huggins interaction parameter (χ), the FAA is a better solvent system for PCL than FA or F since χ value of FAA is less than 0.5 (If $\chi > 0.5$, the solvent considered as a poor solvent).

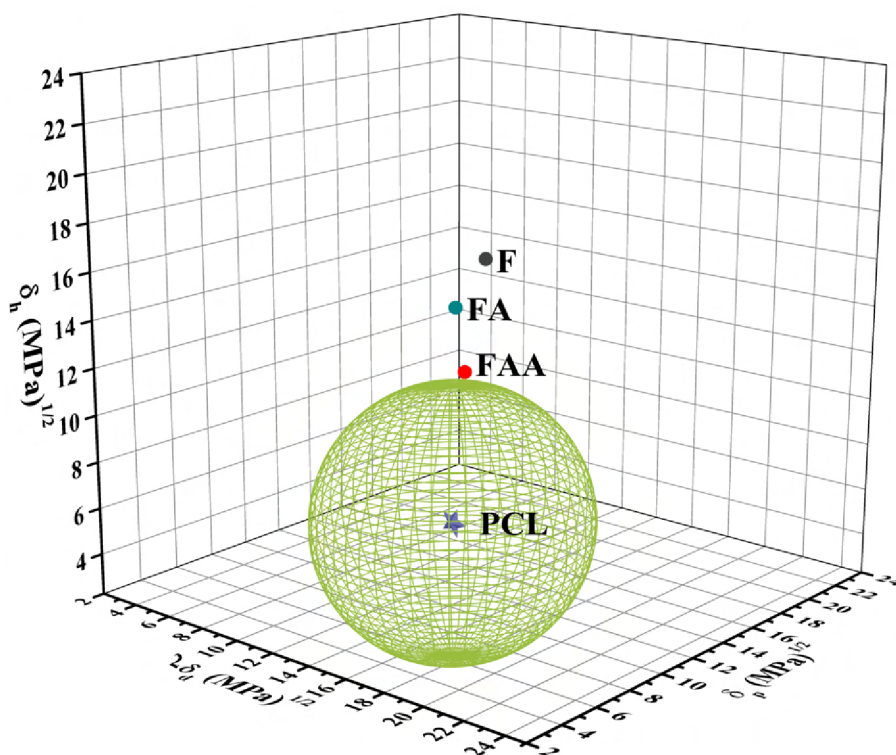


Figure 4.1: 3D representation of the Hansen solubility parameter and the solubility sphere of interactions.

Table 4.2: Dielectric constant (ϵ), the Hensen solubility parameters (δ_d , δ_p , and δ_h), total solubility parameters (δ_t), the distance between the solvent and the polymer in the solubility space (D_{P-S}), interaction radius of the Hansen sphere (R_a) (this value is corresponding to the PCL molecular weight of 65 kDa [89]), relative energy dispersion (RED), and Flory–Huggins interaction parameter (χ).

Solvent/ polymer	ϵ at 25 °C [102, 103]	δ_d	δ_p [\sqrt{MPa}]	δ_h	δ_t [\sqrt{MPa}]	D_{P-S} [\sqrt{MPa}]	RED [89]	χ
PCL	03.2	17.7	06.2	07.8	21.4	—	$R_a=5.5$	—
F	58.0	14.3	11.9	16.6	24.9	12.5	2.8	0.59
FA	34.9	14.4	10.0	15.0	23.1	10.5	1.9	0.52
FAA	28.2	14.8	10.0	12.4	21.8	08.3	1.5	0.32

4.1.3 Effects of the solvent system on the stability of PCL

Although the solvent systems F, FA, and FAA are more benign than the commonly used solvent system for PCL, it is well known that this acidic mixture degrades the PCL chains. Consequently results in the reductions of PCL molar mass and subsequent viscosity reduction of the PCL spinning solution. Hence, as discussed in sub-chapter 3.2.4 on page 42, 10 wt% PCL was dissolved in F, FA, and FAA solvent systems to obtain F-PCL, FA-PCL, and FAA-PCL spinning solutions. For analyzing the PCL stability in the solvent system as a function of the solvent system, time (storage time), and temperature, half of the solutions were kept at room temperature, whereas the remaining solutions were kept in the fridge. Surprisingly, the FAA-PCL solution, which was kept in the fridge, changed from a liquid phase to a gel state Fig. 4.2a. At the same time, F-PCL and FA-PCL solutions remained in the liquid state. Additionally, the FAA-PCL gel phase was transferred back to a liquid state over time at ambient temperature after being removed from the fridge (Fig. 4.2a–d), so it can be called a thermoreversible gel.

Furthermore, the FAA-PCL thermoreversible gel was analyzed by our group using the light microscope [104], it revealed an exciting structure that consisted of agglomerated PCL micro-spheres (Fig. 4.2e). According to the equilibrium between entropy and interaction energies, polymers take on the stretched coil and compact globule states [105]. Therefore, the authors hypothesize that when the FAA-PCL solution was kept in the fridge, the PCL macromolecular chains converted from an entropy-dominated coil shape to an energy-governed globular one. The coil-to-globule transition phenomenon will be studied in the future since it is not under the scope of the thesis. However, the stability

of PCL in these solutions and the solution kept at room temperature were discussed in the following paragraph.

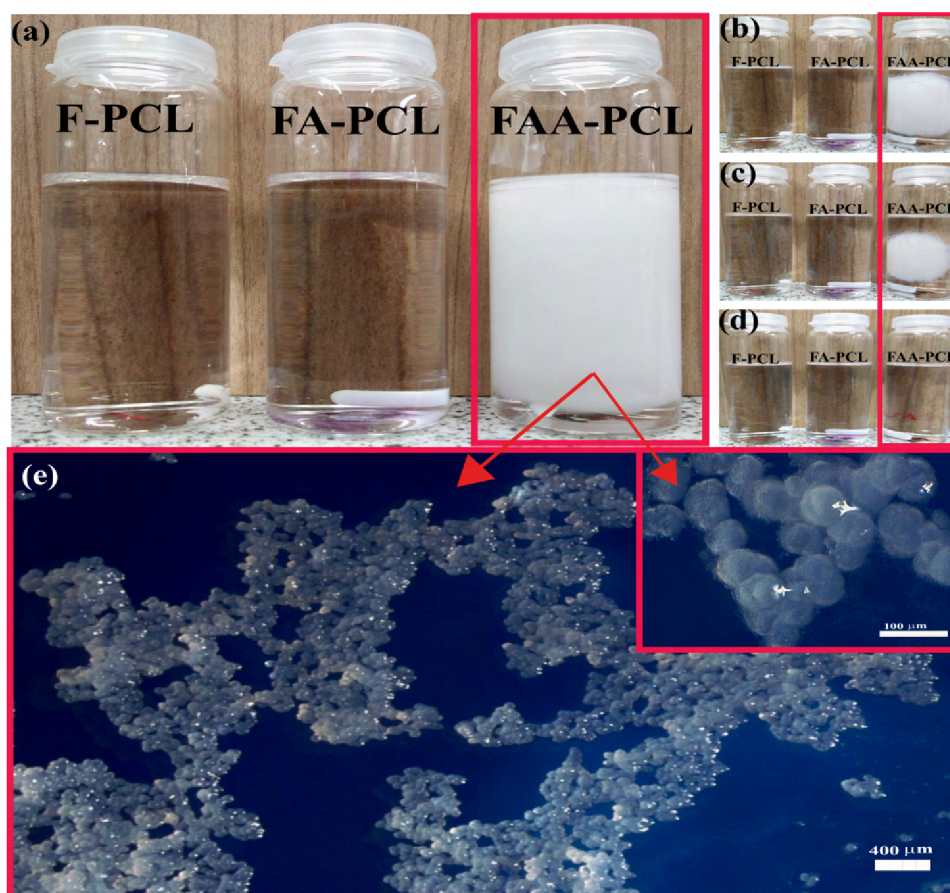


Figure 4.2: (a) Picture of F-PCL, FA-PCL, and FAA-PCL solutions after being immediately taken out from the fridge. (b – d) the transition of FAA-PCL thermoreversible gel to the liquid phase and (e) light microscope images of FAA-PCL thermoreversible gels. The red box represents the FAA-PCL thermoreversible gel [104].

The PCL's GPC chromatograms are depicted in Fig. 4.3. In all the cases, the solutions stored at room temperature reflected higher elution times (i.e., a lower molar mass) than those stored in the fridge (i.e., a higher molar mass). At the same time, the FAA-PCL solution stored at room temperature and in the refrigerator reflected lower elution time signifying a higher molecular weight. In contrast, F-PCL stored at room temperature and in the fridge showed higher elution time, representing a lower molecular weight, followed by FA-PCL. Hence, F-PCL and FA-PCL exhibited evidence of a higher degree of polymer degradation than the FAA-PCL due to a higher concentration of protic carboxylic acids, which promoted acid-catalyzed scission of ester bonds. However, in the case of FAA-PCL, the carboxylic acid concentration is reduced upon the addition of aprotic acetone, thus subsequently resulting in the lower degree of acid-catalyzed scission of ester

bonds. The molecular mass reduction over time is also reflected in the decrease of the solution's viscosity. As shown in Fig. A.1, the FAA stored in the refrigerator showed higher viscosity over time, followed by those stored at room temperature. As expected, F-PCL stored at room temperature exhibited lower viscosity. Thus it can be concluded that the used solvent system and the storage condition strongly influence the PCL stability.

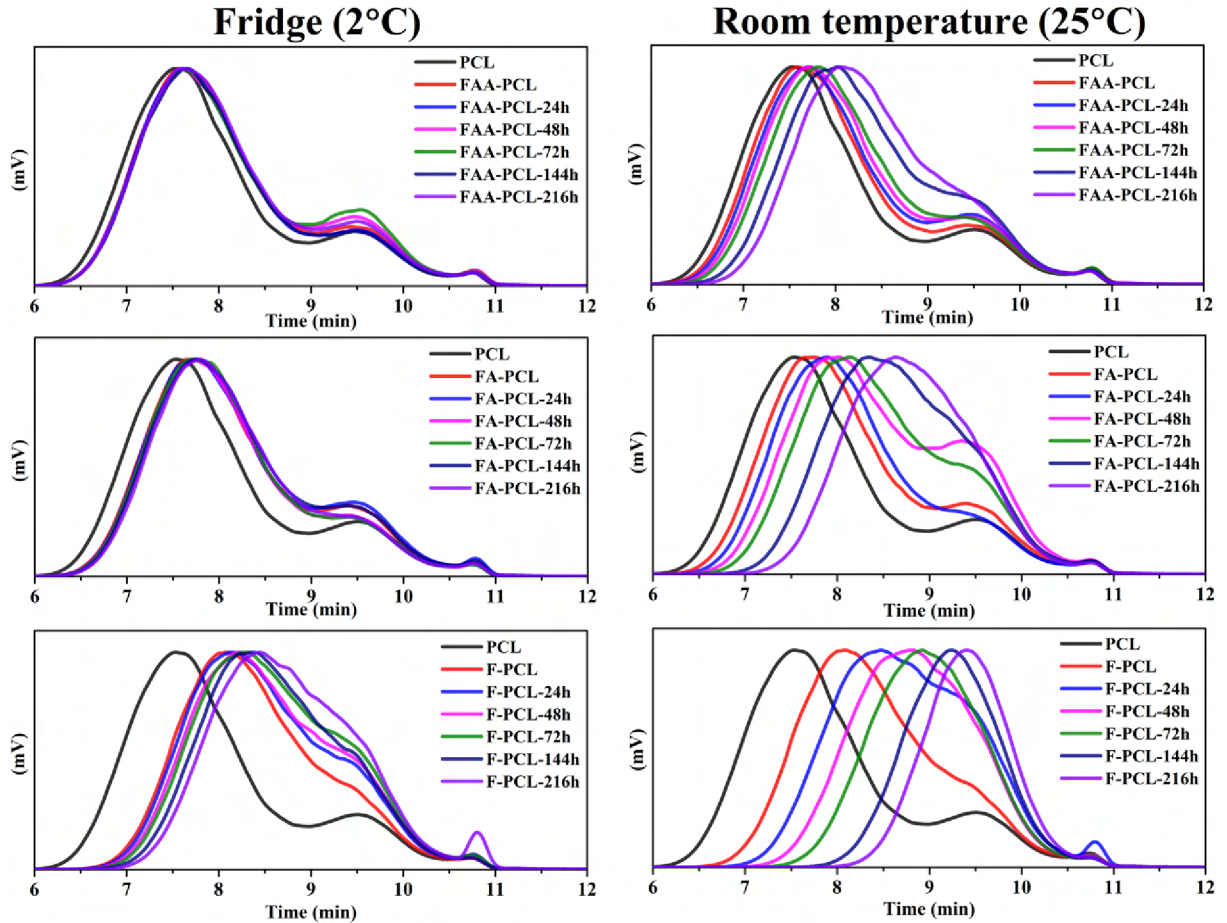


Figure 4.3: *Stability of PCL in FAA, FA, and F solvent systems. GPC chromatograms of FAA-PCL, FA-PCL, and F-PCL with respect to their storage condition (room temperature and fridge at 2°C) and storage time (24, 48, 72, 144, 216 hours).*

4.1.4 Effects of solvent system on the surface tension and viscosity of the solution

The combined contribution of the viscosity and surface tension significantly governs the ideal polymer solution for electrospinning. Therefore, we examined the surface tension and viscosity of F-PCL, FA-PCL, and FAA-PCL solutions to study the AC spinnability as described in the Chapter 3.2.3 on page 41. Whether the polymeric solution's surface tension is a defining parameter for AC electrospinning was examined at the first step using

the Wilhelmy plate method (as described in Chapter 3.2.3). It is clear from Fig. 4.4 that the used solvent system affects the surface tension of the polymeric solution regardless of the PCL's concentration. The statistically significant higher surface tension was noticed on F-PCL, followed by FA-PCL and FAA-PCL. The higher surface tension of F-PCL could be also attributed to the fact that F exhibits a higher δ_h value, which indicates a higher cohesive force between the solvent molecules (F). FAA exhibits a lower δ_h value than FA and F, and hence, there could be a weaker cohesive force between the ternary solvent molecules (FAA), and consequently, FAA-PCL could have obtained a lower surface tension. As shown in Fig. 4.4b, the inversely proportional relationship between the solvent's surface tension and the total solubility parameter was also observed.

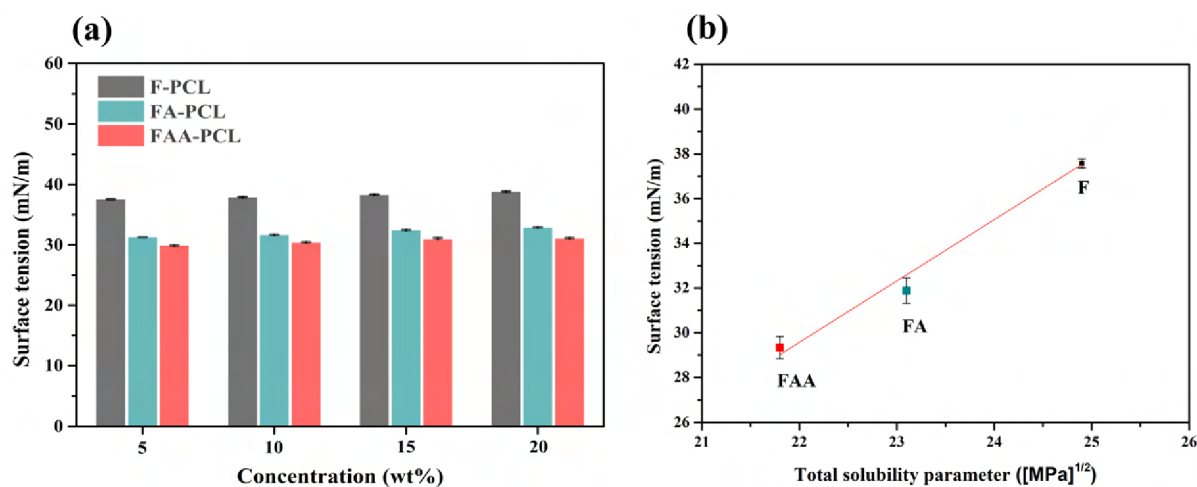


Figure 4.4: (a) The surface tension of FAA-PCL, FA-PCL, and F-PCL precursor solutions corresponding to precursor concentration and (b) The relationship between the solvent's total solubility parameter and the surface tension.

Apart from the surface tension, the solution's viscosity significantly influences the electrospinning process and the resultant electrospun fiber morphology. Since the viscosity of the solution is directly determined by the quality of solvent, concentration and molecular weight of the polymer in the solution, the viscosity was analyzed as a function of the solvent system and polymer concentration (Fig. 4.5). Although the polymer concentration does not affect the surface tension, it influences the solution's viscosity. Besides, the used solvent system critically affects the viscosity of the polymer solution.

As shown in Fig. 4.3, the molecular weight of PCL is also affected by the employed solvent system. The F-PCL shows a lower viscosity than the FA-PCL and FAA-PCL because of the efficient degree of acid catalyzed degradation of PCL's ester bonds during the dissolution of PCL (Fig.4.3) [106, 107]. As expected, the acidic nature of F promoted a greater degree of acid-catalyzed scission of the ester bonds (-COO-) of PCL, thereby

resulting in a decrease in the viscosity over time, followed by FA and FAA solvent systems (Fig. A.1). Previous studies have also shown a reduction of viscosity in an acidic medium over time due to PCL degradation [90, 106]. Plots of dynamic viscosity at different shear rates for various PCL solutions revealed a Newtonian and non-Newtonian behavior for lower concentration solutions (5 wt% of PCL) and higher concentration solutions (10, 15, and 20 wt% of PCL), respectively (Fig. 4.5b–d). As the shear rate increased (500 to 750 s^{-1}), the viscosity of 10 and 15 wt% precursor solutions slightly increased, indicating this non-Newtonian fluid’s shear-thickening behavior. In contrast, as shear rates increased (525 to 750 s^{-1}), the viscosity of 20 wt% FAA–PCL, FA–PCL, and F–PCL was decreased from 3750, 2937, and 1370 mPas to 3410, 2725, and 1345 mPas, respectively.

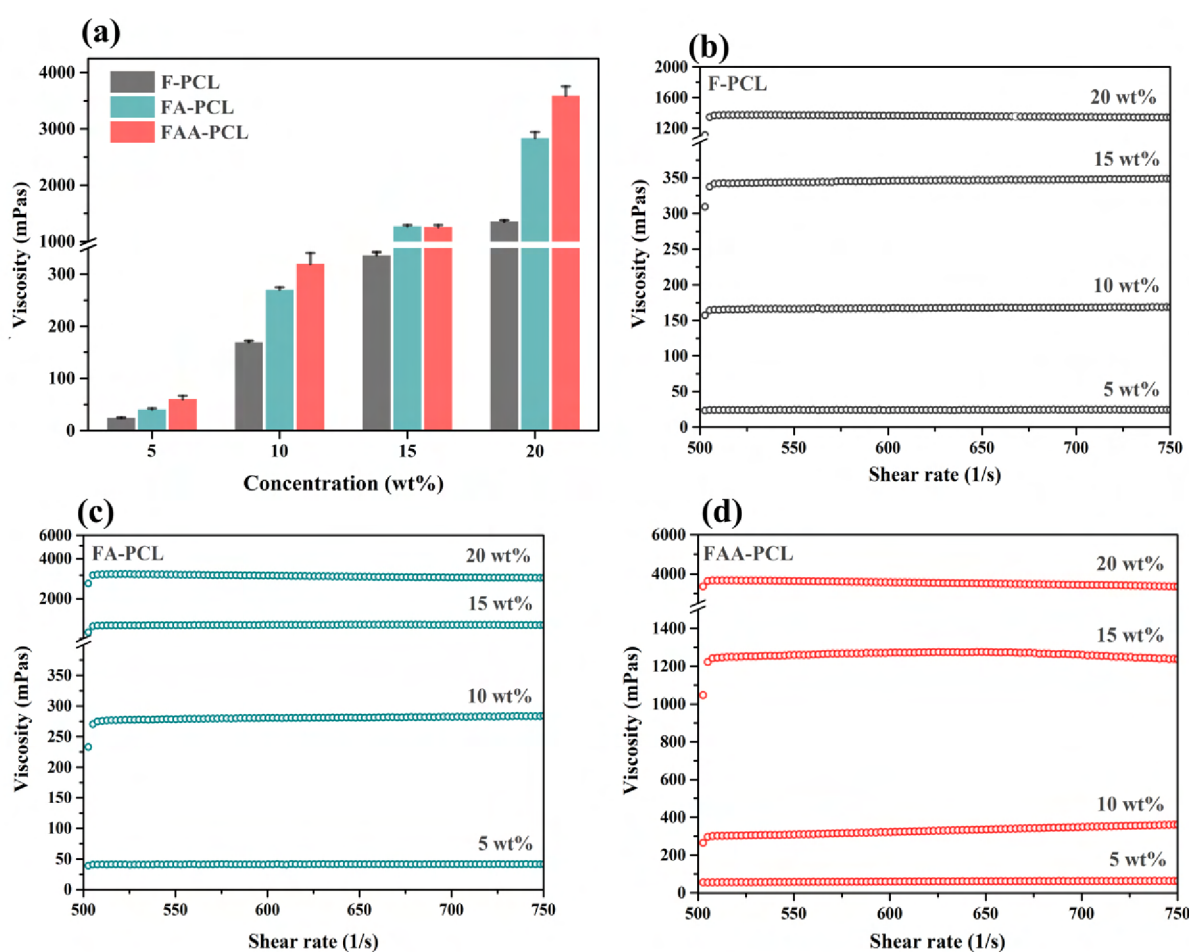


Figure 4.5: (a). The viscosity of FAA–PCL, FA–PCL, and F–PCL precursor solutions corresponding to precursor concentration and (b–d) the precursor solution viscosity as a function of shear rate (the dynamic viscosity values are shown in milli Pascal-second (mPas)).

This shear thinning or shear thickening effect can be associated with the confirmation of macromolecular chains in the solution. In other words, these behaviors significantly depend on the solvent systems, polymer-solvent interaction, molecular weight, and concentration of the polymers [108–111]. Lawson *et al.* also observed this shear-thinning behavior on 20 wt% PCL with sodium acetate in an acetic acid (AA) solvent system [54]. On the other hand, this behavior was not observed with pristine PCL/AA solutions. In addition, Nakano *et al.* reported the role of the solubility parameter on the intrinsic viscosity by revealing that when the solubility parameters of the polymer and the solvent are close to each other, a higher intrinsic viscosity of the solution was observed [110]. Hence, the higher viscosity of FAA–PCL was confirmed by the solubility parameters of the solvent and polymer.

4.1.5 AC spinnability of the polymeric solutions

In this section, AC spinnability of PCL has been extensively analyzed based on the solvent system (F, FA, and FAA), the polymer concentration (5, 10, 15, and 20 wt%), the solution properties (solubility parameter, viscosity, and surface tension), and the applied AC potential (25 and 32 kV_{RMS}). Electrospinning is not feasible when using the 5 and 20 wt% of F–PCL and FA–PCL due to the lower and higher viscosity of the solutions, respectively. At the same time, 10 and 15 wt% of F–PCL and FA–PCL solutions are well electrospinnable at the applied AC potential of 25 and 32 kV_{RMS}. Interestingly, the minimum and maximum concentrations for AC spinnability of FAA–PCL became 5 and 10 wt%, respectively. Previous studies demonstrated that the critical polymer concentration for producing the electrospun fiber could be lowered when the polymer is dissolved in the blends of bad (or theta) and good solvents than in the single good solvent [112] [113]. Hence the aforementioned phenomenon could be the reason for fabricating the nanofibers even at such a low concentration (5 wt%) of FAA–PCL. In addition, the author hypothesizes that since FAA has a higher vapor pressure than F or FA, the FAA–PCL jet could form much quicker gelation due to rapid solvent evaporation. This quicker gelation could restrict the Plateau–Rayleigh instability. Hence, unlike 5 wt% F–PCL and FA–PCL, 5 wt% FAA–PCL can form a stable jet under AC electric field and subsequently form electrospun fibers with beaded morphology.

From Fig. 4.7, it is clear that the average fiber diameter of F–PCL (10 and 15 wt%) was lesser than the FA–PCL (10 and 15 Wt%) and FAA–PCL (10 wt%). This could be attributed to the following factors: (i) the highly acidic nature of formic acid promotes the scission of ester bonds during the dissolution of PCL [106], [107]; (ii) due to the relatively

high dielectric constant of formic acid, the polymeric jets experience a strong repulsive electrostatic force resulting in the jets being stretched to a greater extent, which in turn encourages the formation of thinner fibers [102]; and (iii) the total solubility parameter of formic acid is larger than the PCL. In other words, the δ_h component of F is two times higher than that of PCL since the solubility parameter is derived from the second root of CED, which is directly linked to the latent heat of vaporization (see Table 4.2 on page 59). Hence, the evaporation rate of F is likely to be reduced from the F–PCL polymeric jet. Therefore, the F–PCL jet experiences greater stretching due to slow evaporation and a high dielectric constant value (ϵ) of 58 at 25 °C. Since the dielectric constant is linearly proportioned to electric pressure ($P_e = \epsilon E_t^2/2$), the F–PCL jet experiences higher electric pressure than FA-PCL and FAA-PCL. Thus, F–PCL eventually results in thinner PCL fibers [110]. In contrast, the FAA solvent system has a lower dielectric constant (28.2 at 25 °C) and higher vaporization pressure than the FA and F; hence the FAA–PCL jet experiences lesser stretching, and is thus encouraged to create thicker fibers.

In all the cases, lower concentrations of PCL result in thinner fibers compared to that at higher concentrations. During the electrospinning process, the evaporation of solvent molecules from the polymeric solution occurs at the surface of the electrode and, significantly, during the traveling of the polymeric jet through the electric field toward the collector. The solvent starts to evaporate from the polymeric jet in three stages: (i) emanation of the jet from the liquid surface, (ii) formation of straight jet, and (iii) whipping/bending instability. The solvent molecules tend to evaporate at a critical rate and a critical time at each stage of the jet movements. For instance, during stages (i) and (ii), solvent evaporation occurs merely by diffusion mechanism due to the lower velocity of the air in the vicinity of the polymer solution. In the case of the bending/whipping region (stage (iii)), the jet starts to stretch due to the whipping movements, thus leading to an increase in the surface area of the jet, and as a result, high air velocities are created in the vicinity of the jet. This promotes efficient evaporation of the solvent through the convection mechanism due to the whipping movements of the jet [114, 115]. As a consequence, solidified polymers are collected in the form of electrospun fibers. The solidification of the jet is much quicker in high viscous solutions since polymeric chain entanglements are higher than that in low viscous solutions [19]. When the solidification of the jet is rapid, the elongation process of the jet can continue only for a limited time. Thus, it results in the formation of thicker fibers for higher PCL concentrated solutions.

The effects of solvents and applied AC potentials on the electrospun morphology were analyzed by SEM (Fig. 4.6). The beads-free nanofibers were achieved for 10 and 15 wt%

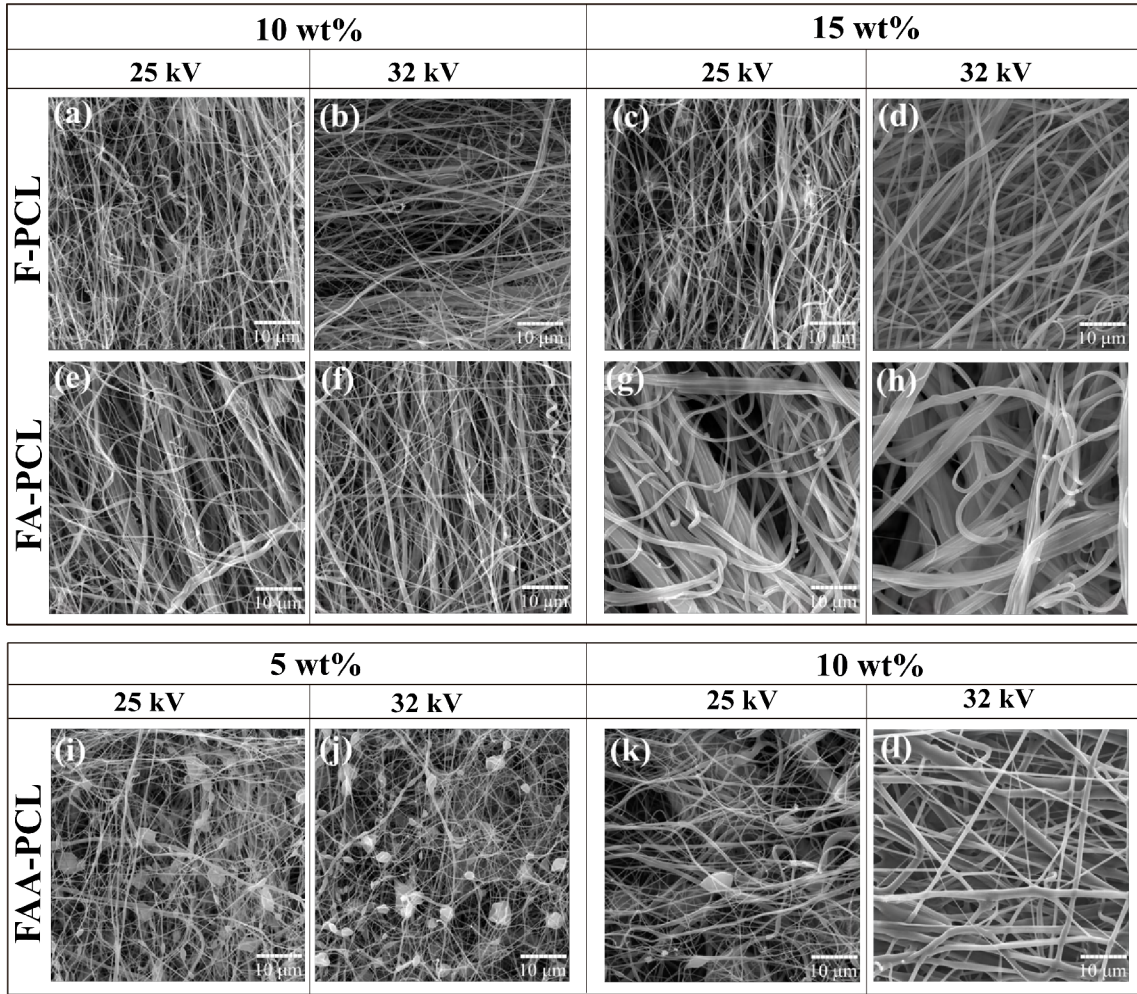


Figure 4.6: SEM micrographs of various PCL ENS as a function of the various solvent systems (*F*, *FA*, and *FAA*), polymer concentrations (5, 10, and 15 wt%), and applied high voltage (25 and 32 kV_{RMS}).

of F-PCL and FA-PCL at 25 and 32 kV_{RMS} , whereas, 5 wt% of FAA-PCL resulted in beaded nanofibers. The viscosity of 5 wt% FAA-PCL is not relatively high enough to overcome the Plateau-Rayleigh instability. Thus it encourages the formation of beads. On the other hand, the frequency of beads on the fiber was reduced for 10 wt% FAA-PCL at 25 kV_{RMS} , and there were almost no visible beads at 32 kV_{RMS} , as bead formation was suppressed by the solution's higher viscosity.

Apart from the solution properties, fiber morphology was determined by the applied AC high voltage. The results (Fig. 4.7) show that increasing applied voltage from 25 to 32 kV_{RMS} leads to a gradual increase (statistically significant) in the electrospun fiber diameter from (211.3 ± 74.7) nm to (239.4 ± 88.6) nm, (248.2 ± 147.9) nm to (281.9 ± 121.9) nm, and (488.6 ± 221.8) nm to (853.8 ± 464.0) nm for 10 wt% F-PCL, FA-PCL,

and FAA-PCL, respectively. Moreover, the same trends were observed for 15 wt% of F-PCL and FA-PCL, whereas not significantly on 5 wt% FAA-PCL. This tendency may be explained by the fact that a higher voltage favors the ejection of more of the polymeric solution from the electrode than a lower voltage. This higher voltage and consequent increase in ejection of polymeric solution gives rise to the formation of thicker fibers.

On the other hand, Lawson *et al.* reported that increasing AC high voltage results in thinner fiber diameter when glacial acetic acid is used as a solvent [54]. This contradiction could be attributed to the synergic effects of the following facts: (i) In this study, F, FA, and FAA solvents were used and reflected higher vapor pressure (42.6, 29.1, and 96.0 mm Hg at 25 °C, respectively) than the acetic acid (15.7 mm Hg at 25 °C); thus, the polymeric jet experiences lesser instability (whipping and/or stretching) in the electric field due to the faster solidification. (ii) Furthermore, increasing voltage favors the ejection of more of the polymeric solution while simultaneously accelerating the velocity of the polymeric jet [116]. Hence, the average fiber diameter of F-PCL, FA-PCL, and FAA-PCL increases when the applied voltage is increased from 25 to 32 kV_{RMS} . In this study, it is clear that the AC spinnability of F-PCL, FA-PCL, and FAA-PCL significantly depends on the precursor concentration, viscosity, and applied AC high voltage. However, the surface tensions of the corresponding precursor solutions did not significantly influence the AC spinnability of various PCL solutions regardless of the precursor concentrations.

Table 4.3: *Vapour pressure and diffusion coefficient of various solvents [117–119].*

Solvent or Solvent system	Vapour pressure Hg at 25 °C	Diffusion coefficient cm^2/s at 18 or 19 °C [117–119]
F	42.6	0.120
FA	29.1	0.126
FAA	96.0	0.119

4.1.6 Productivity of PCL electrospun nanofibers

The productivity of F-PCL, FA-PCL, and FAA-PCL electrospun fibers have been studied by means of various solvents and applied voltages (measurements method can be seen in Chapter 3.2.8 on page 47). For productivity evaluation, the applied high voltage was increased from 25 to 32 kV_{RMS} , while the concentration was kept constant (10 wt% of PCL). When the applied high voltage was increased from 25 to 32 kV_{RMS} , the productivity of electrospun fibers increased from $(1.1 \pm 0.1$ to $2.2 \pm 0.2)$ g/h, $(2.9 \pm 0.1$ to $6.9 \pm 0.1)$ g/h, and $(5.7 \pm 0.2$ to $12.4 \pm 0.3)$ g/h for F-PCL, FA-PCL, and FAA-PCL, respectively

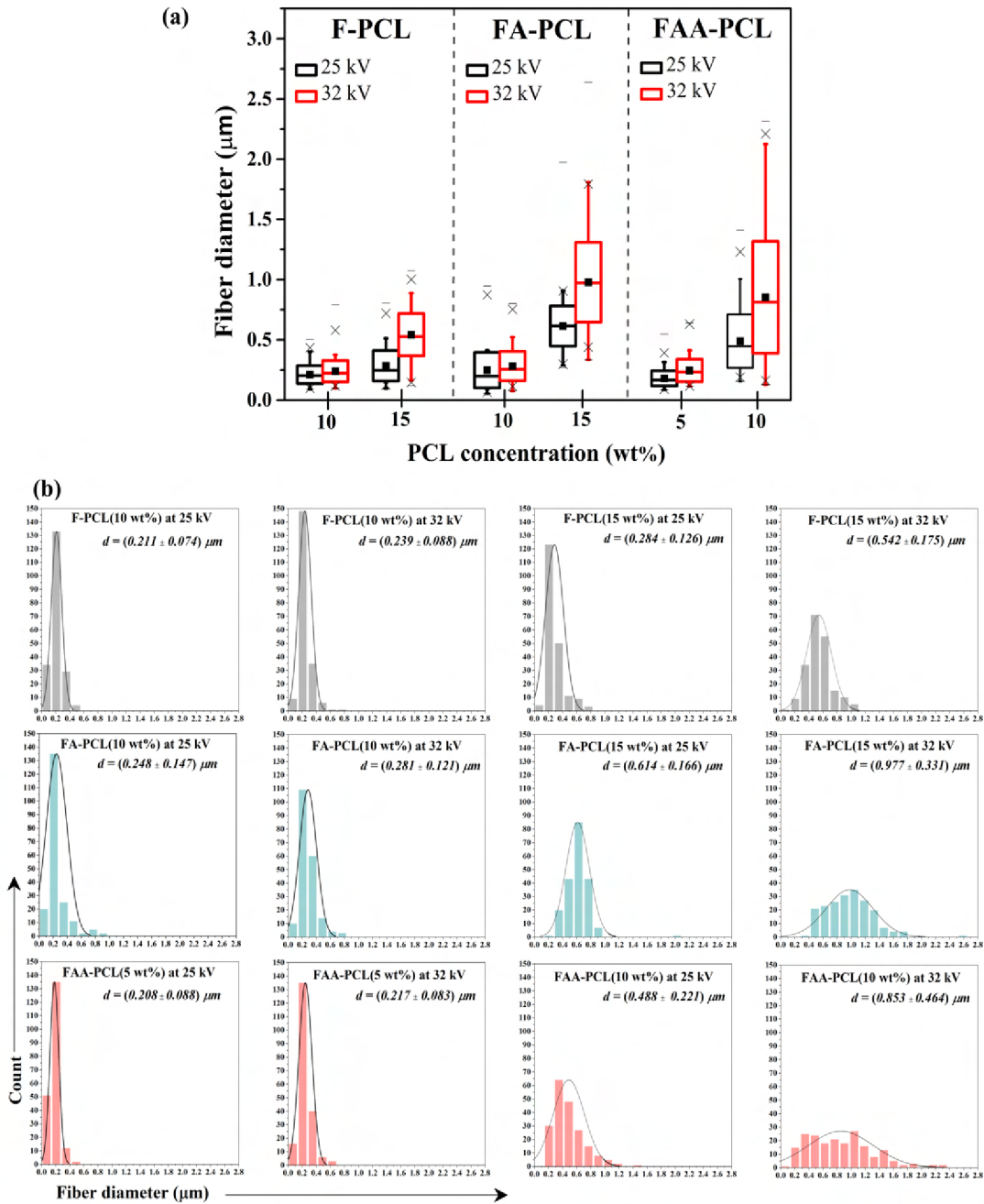


Figure 4.7: (a) Box plot of various PCL ENS's fiber diameter as a function of the polymer concentration and applied AC high-voltage, and (b) corresponding histograms with normal distribution curves. The solid squares in the box represent the mean values, while the lower, middle, and upper limits correspond to the first (25%), second (50%) and third (75%) quartiles, respectively. The lower and upper whiskers represent 5% and 95%. The minimum and maximum values are denoted as '—'. (d refers to diameter).

(Fig. 4.8a). As discussed in sub-chapter 2.4 on page 14, although AC and DC jets behave in quite different manners, in principle, both technologies are similar. Thus, the author hypothesis that the productivity of AC electrospinning can be explained using the

principles of DC electrospinning. In the case of DC electrospinning, Lukas *et al.*, [65], [66] established the equation for the relationship between the characteristic wavelength (λ) of fluid instabilities or distance between the adjacent jet and the charge density (additionally look Fig. 2.5 on page 20a as well):

$$\lambda = \frac{12\pi\gamma}{\left[(2\varepsilon E_0^2) + \sqrt{(2\varepsilon E_0^2)^2 - 12\gamma\rho g} \right]}, \quad (4.1)$$

where γ and ρ are corresponding to the surface tension and density of the fluid, g is gravitational acceleration, E_0 is the electric field strength, and ε corresponds to the electric permittivity of the ambient gas. According to Eq 4.1, as the magnitude of electric field strength increases, the distance between the adjacent jets will become shorter; consequently, more jets will emerge from the surface of the liquid. On the other hand, higher surface tension will increase the inter-jet distance. Furthermore, while increasing the applied voltage, the charged jet moves faster in the electric field since electric pressure is the critical factor for the velocity of the charged jet. In addition, as discussed in previous section (4.1.5), the higher voltage accelerates the ejection of more of the polymeric solution. Therefore, higher productivity with significantly thicker electrospun fibers was observed under a given constant polymer concentration while using a relatively higher applied voltage than when using a lower voltage. Furthermore, Fig. 4.8b shows the relationship between the fiber diameter and the productivity of electrospun fibers, which reflects that both were linearly proportional to each other.

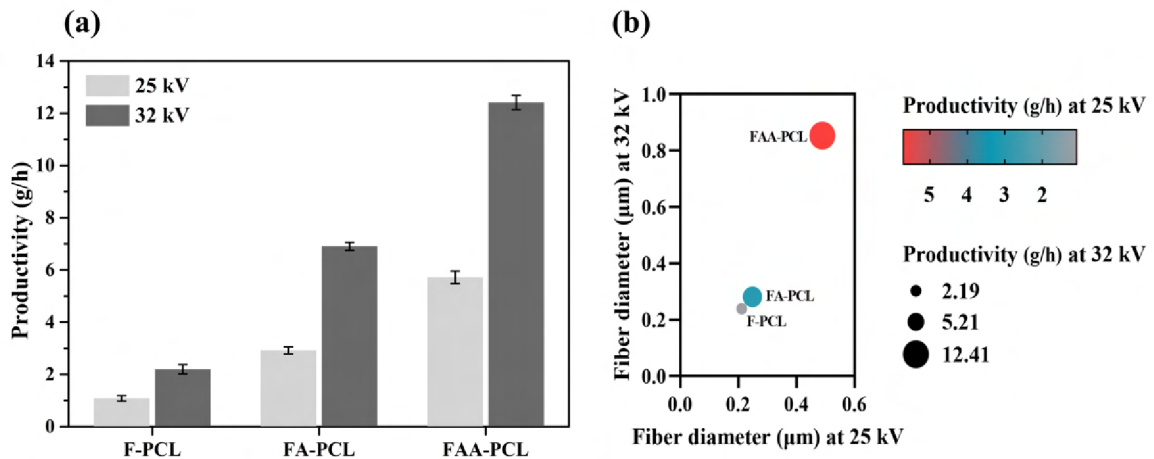


Figure 4.8: (a) Productivity of various PCL electrospun nanofibers (10 wt% of PCL at 25 and 32 kV_{RMS}), and (b) productivity of electrospun nanofibers as a function of average fiber diameter.

Our previous results have shown that AC high-voltage signal shape (or waveform) and/or frequency significantly affect the morphology and productivity of the electrospun PCL nanofibers regardless of their mean fiber diameter [20]. In addition to the applied high voltage, the throughput of electrospun fibers was also found to be influenced by the employed solvent system. The lower throughput of F–PCL electrospun fibers could be attributed to the higher surface tension and lower viscosity of the corresponding polymer solution (due to efficient acid-catalyzed degradation of PCL chains) as compared to the FA and FAA–PCL higher throughput.

4.1.7 Principal component analysis of AC spinnability of PCL

The principal component analysis was applied on the data with 11 variables (as denoted in red), which is shown in Fig. 4.9a and 4.9b. Analysis reveals that the first two principal components (PC1 and PC2) contain most of the variance (71%). An additional 25% of the variance is in PC3 and PC4 (Fig. 4.9b). The figures contain the loadings of the variables (arrow), the scores of the observations (sample name) for the two components, and an ellipse drawn around each group.

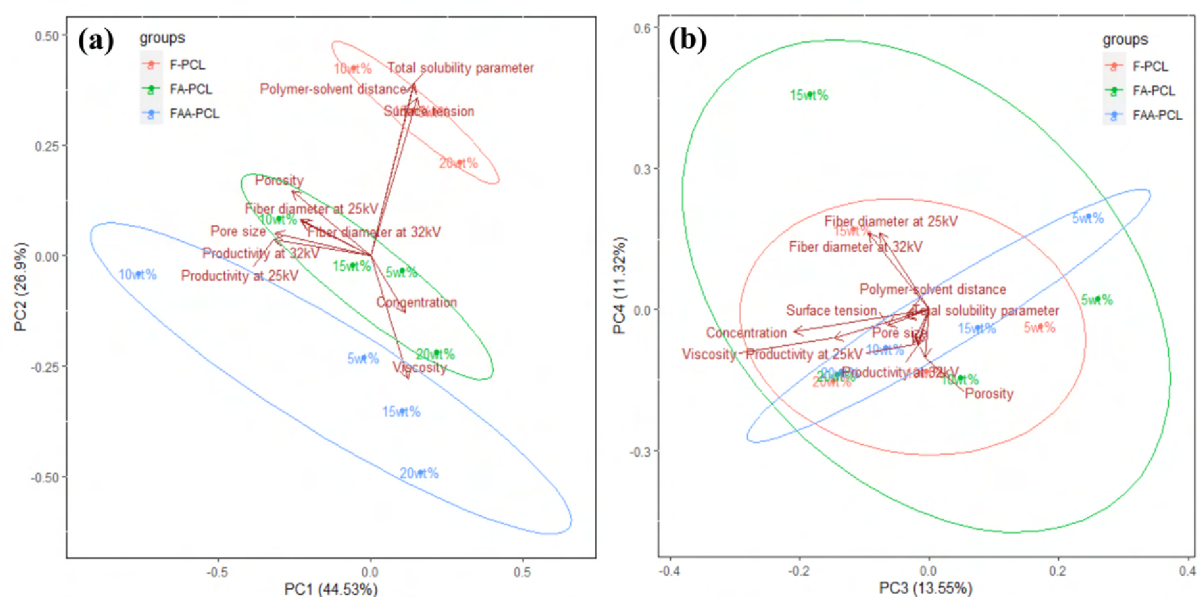


Figure 4.9: *Principal component analysis of AC spinnability of PCL. (a) PC2 as a function of PC1, and (b) PC4 as a function of PC3.*

The F–PCL, FA–PCL, and FAA–PCL formed distinct clusters (Fig. 4.9a), indicating that they differed, especially in terms of surface tension, total solubility parameter, and

polymer–solvent interaction parameter. In contradiction to observations in the previous section, the variables fiber diameter and productivity of electrospun fibers appear negatively correlated with viscosity and the precursor concentrations. This is, however, caused by the nature of the observed data. In other words, 5 and 20 wt% F and FA–PCL, as well as 15 and 20 wt% FAA–PCL, were not able to produce the electrospun fiber, which resulted in the lack of the subsequent variables (fiber diameter, productivity, pore size, and porosity). These variables were taken as zero while running the PCA. From PC1 vs. PC2, it is clearly visible that various 10 wt% PCL solutions were nicely separated from other samples (5, 15 and 20 wt%) in terms of higher productivity and fiber diameter. Apart from that PC3 vs. PC4 shows a higher fiber diameter for 15 wt% F and FA–PCL. The non-spinnable solutions, such as 5 and 20 wt% F–PCL and FA–PCL as well as 15 and 20 wt% FAA–PCL, were located on the opposite side of the loadings. This PCA analysis was in line with our previous findings.

4.1.8 Cytotoxicity and in vitro analysis of PCL ENS

Fibroblast cells play an essential role in the regeneration of functional tissues by producing ECM and collagen. It is also important in the wound healing process. Hence, the biocompatibility of F–PCL, FA–PCL, and FAA–PCL ENS was investigated using 3T3–L1 mouse fibroblast cells according to ČSN EN ISO 10993–5 (855220). Two groups of samples were used to analyze cytotoxicity, the first of which was washed with PBS (two minutes), and the second of which was used as fabricated. The biocompatibility of ENS by means of cell viability was examined by an MTT assay (Fig. 4.10). None of the tested extracts showed a detrimental effect on cell viability; all values for extracts were higher than 70% of the negative control (NC), which shows no cytotoxicity in the PCL ENS. All tested PCL ENS extracts and the NC group showed significantly higher cell viability compared to the positive control (PC) group. The only exceptions were the washed FA–PCL and unwashed FA–PCL, as the normality tested failed; therefore, $p \geq 0.05$. However, we could observe a trend that the FAA–PCL showed better cell viability, followed by F–PCL and FA–PCL (Fig. 4.10b). It is worth mentioning that the washed samples resulted in higher cell viability than the unwashed samples. A slight decrease in the cell viability of F–PCL and FA–PCL could be attributed to the presence of residual solvents in the ENS. This indicates that the residual solvent could be acetic acid and formic acid, both of which have lower vapor pressure than acetone. Hence, these organic acids may be trapped in the ENS as residual solvents during the fiber creation process. At the same time, the concentration of these acids is lower in FAA–PCL than in the FA–PCL and F–PCL; thus, it showed better biocompatibility. The quantification of residual solvent trapped in the

electrospun fibers was challenging since their concentration was below the detection limits of widely used chromatographic techniques for testing the residual solvent. Moreover, it is well known that these solvents are eliminated from the body by metabolic pathways. The metabolic MTT assay analysis thus showed that fabricated F-PCL, FA-PCL, and FAA-PCL ENS (washed and unwashed) did not show any cytotoxicity to the 3T3-L1 mouse fibroblast cells, which suggests that the fabricated PCL ENS could be suitable for a wide range of biomedical and tissue engineering applications.

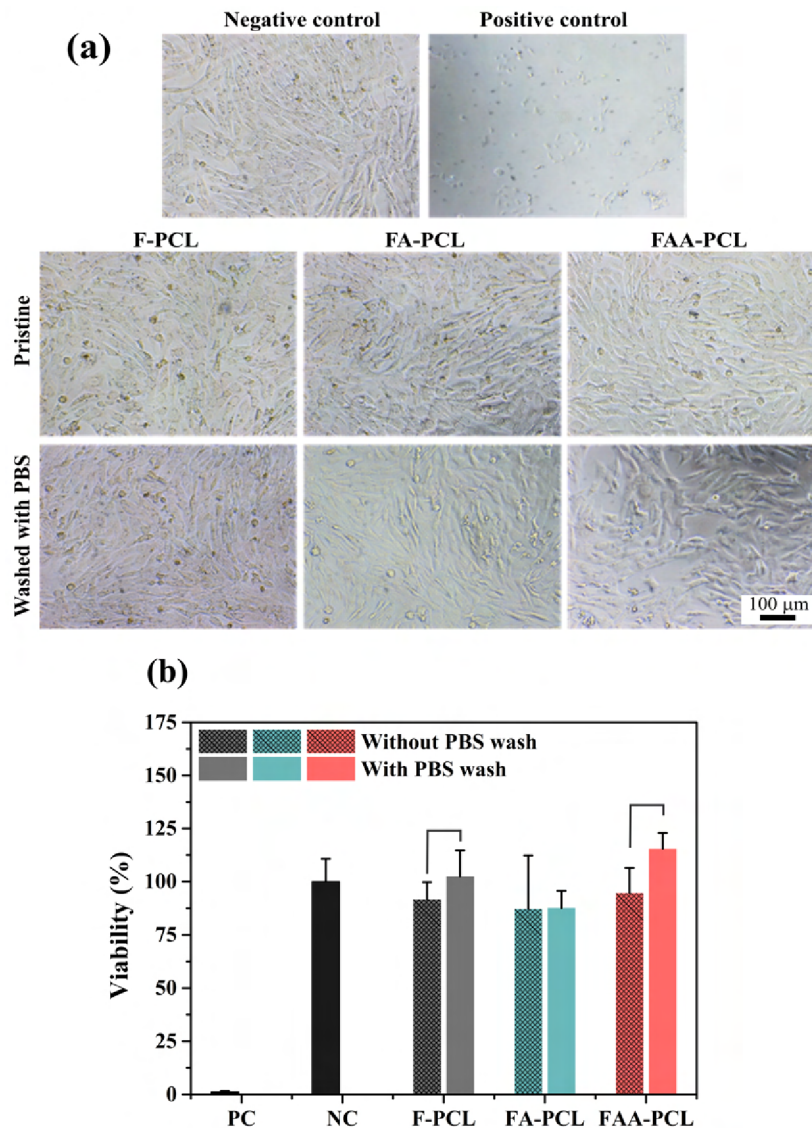


Figure 4.10: Cytotoxicity analysis of various ENS. (a) light microscopy images of the fibroblasts cells and (b) cell viability in the various material's extracts (MTT-assay).

After evaluating the cytotoxicity of the extracts, 3T3-L1 mouse fibroblast cellular behavior on the PCL ENS is evaluated in this part. MTT assay (Fig. 4.11b) and fluorescence microscopy (Fig. 4.11a) were utilized to investigate the adhesion (day 1), proliferation

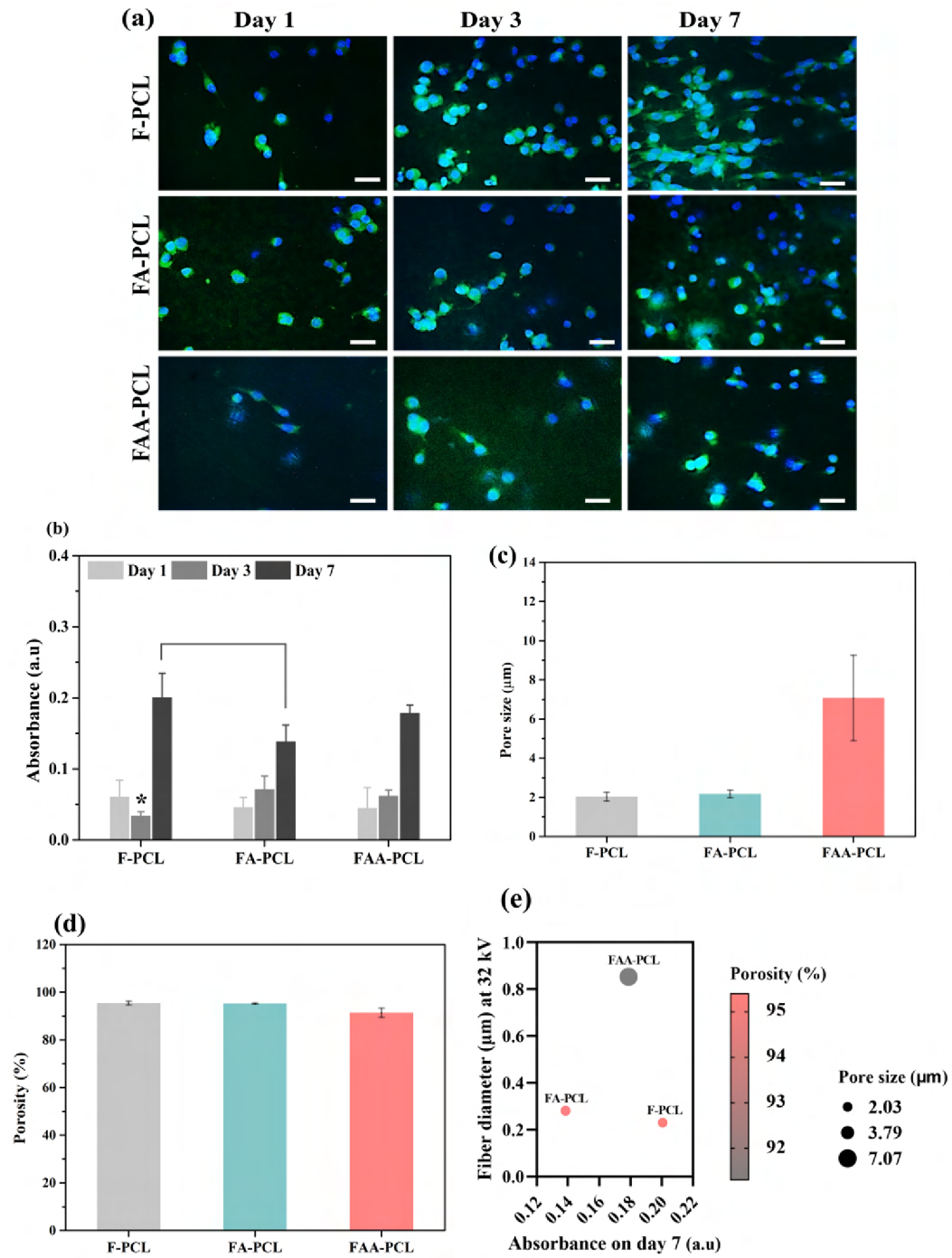


Figure 4.11: *In vitro* analysis of various PCL ENS: (a) fluorescent microscopy images of the cells and (scale bar 50 μm), (b) metabolic activity of cells on various PCL ENS, (c) The mean value of pore size (d) porosity of PCL ENS, and (e) relationship between the fiber diameter, pore size, porosity, and metabolic activity (*means statistically lowest value on day 3 for F-PCL group).

(day 3 and 7), and morphology of the cells, respectively. This metabolic activity test (day 1, MTT assay) shows comparable values for all tested groups. Subsequently, the prolifera-

tion of the cells at day seven was statistically higher on the F-PCL compared to FA-PCL and FAA-PCL ENS. These findings were further qualitatively confirmed by fluorescence images (Fig. 4.11a), which showed the morphology of adhered and proliferated 3T3-L1 cells (green and blue colors represent the cytoplasm and nuclei, respectively) on all PCL ENS. According to the MTT assay and fluorescence microscopy, it is evident that seven days after cell seeding, all PCL ENS exhibited a higher amount of proliferated cells with elongated shapes, followed by the amounts after three days and one day, respectively. It can be clearly seen that seven days after cell seeding, the cell proliferation was higher on the F-PCL ENS.

In general, cell adhesion to the biomaterial's surface includes specific and non-specific adhesion [120]. Specific adhesion occurs when the biologically active substance (e.g., extracellular and/or cytoskeletal proteins) is present on the surface of the biomaterial, whereas non-specific adhesion is caused by the physical forces (gravity, electrostatic, and van der Waals forces) between the material and the cells. As shown in Fig. 4.11e, the impacts of the porosity and pore size of F-PCL and FA-PCL on the metabolic activity of cells were minimal since their values are similar to each other (Fig. 4.11c and 4.11d). However, this difference in metabolic activity may instead be attributed to the significant variation in electrospun fiber size.

Previous studies have shown that adhesion and the subsequent proliferation of fibroblast cells increase on the smaller fibers rather than on larger fibers due to the larger surface-to-volume ratio [121], [122]. Hence, the smaller fiber diameter of F-PCL (239.4 ± 88.6)nm could have triggered cell adhesion and proliferation. However, the FAA-PCL fiber diameter (853.8 ± 464.0)nm is higher than FA-PCL ENS fiber diameter (281.87 ± 121.9)nm, resulting in better cell adhesion and proliferation than in the latter case. The decreased adhesion and proliferation of the cells on the FA-PCL ENS could be attributed to their intermediate fiber diameter, which could have slightly restricted the metabolic activity of cells. Furthermore, the average pore size of FAA-PCL (7.1 ± 2.1 μ m) was closely corresponding to the average diameter of the fibroblast cells (~ 10 μ m) [123], which consequently could result in more cellular infiltration regardless of its slightly lower surface-to-volume ratio ($91.3 \pm 1.9\%$) than FA-PCL ($95.2 \pm 0.2\%$) and F-PCL ($95.4 \pm 0.7\%$). From this work, in the case of F-PCL and FA-PCL, it is clear that observed cellular behavior is mainly influenced by the size of the electrospun fibers rather than the pore size and porosity of the ENS. Conversely, in the case of FAA-PCL, observed cellular behavior is dependent upon the synergistic effects of electrospun fiber's size, pore size, and porosity of ENS.

4.2 The impacts of various AC high-voltage signal waveforms and frequencies on the spinnability and productivity of PCL nanofibers

The morphology and diameter of the electrospun fibers are influenced primarily by the viscosity, surface tension and conductivity of the applied spinning solution, as well as by the processing and ambient conditions, including the strength of the high voltage applied, the shape of the electrode, the design of the collector, the ambient temperature and the humidity [63, 124–126]. In contrast to the aforementioned parameters, the impact of the waveform and/or frequency of AC high-voltage signal on the spinnability of polymers has been investigated only to a very limited extent. Hence, this chapter aims to provide an initial overview of the impacts of various waveforms and frequencies of AC high voltage signal on the spinnability, morphology and productivity of PCL ENF via the application of advanced collector-less free surface AC electrospinning.

•The waveform and/or applied frequency of AC high-voltage signal are able to affect the electrification of the liquid, jet initiation and termination, the length of the charged segments (either positive or negative), the whipping instability, and the formation of a virtual collector. Thus the waveform and frequency of AC high-voltage signal can be used as new technological parameters for controlling the AC spinnability of polymers•

It was evident from the previous section that 10 wt% FAA–PCL reflected better AC spinnability; hence the same spinning solution is used to study the spinnability as a function of AC high voltage signal's waveform and frequency. Various waveforms, including the square, sine, and triangle forms, were generated using a signal generator and a TREK signal amplifier over an optimized frequency range of 10 to 60 Hz at a fixed applied high voltage of 50 kV.

The electrospun fiber morphology, productivity, and chemical structure are studied by means of scanning electron microscopy (SEM), stereology, gravimetric methods, and Fourier-transform infrared spectroscopy (FTIR). The investigation of the generation of a steady fibrous plume of PCL was followed by the analysis of the morphology, fiber diameter, productivity, and chemical structure of the PCL ENF as a function of various waveforms and frequencies.

4.2.1 Experimental conditions

All experimental details can be found in Chapter 3. The parameters that are specifically used in this chapter are summarized in Table 4.4.

Table 4.4: *Various spinning solutions and AC electrospinning processing parameters (FAA-PCL means PCL dissolved in formic acid/ acetic acid/ acetone (FAA).)*

Precursor solution	FAA-PCL
Polymer concentration	10 wt%
AC Electrospinning processing parameter	Spinneret's surface diameter: 2.5 cm Spinneret to collector distance: 22 cm Solution feeding rate: 14 – 18 mL/min Collector's peripheral speed: 30 – 40 m/min Applied voltage: 50 kV _{RMS} Waveform: Square, sine and triangle Frequency: 10, 20, 30, 40, 50, and 60 Hz Temperature: 21 – 23 °C Humidity: 42 – 45 %

4.2.2 Effects of the AC high-voltage signal waveform and frequency on the electrospinnability of PCL

In order to focus only on the impacts of various waveforms and frequencies on the spinnability of 10 wt% FAA-PCL, the other parameters were almost set as constant (the applied voltage, and spinneret's geometry and position) (Table 4.4). Only in the case of feeding rate and the peripheral speed of the collector (rotating cylinder) was slightly adjusted to get a stable fibrous plume and subsequent fiber collection.

The initial investigation of the spinnability of 10 wt% FAA-PCL revealed that the waveform determines the minimum and maximum frequency range for the formation of a steady fibrous plume (10 – 60 Hz and 20 – 60 Hz for the sine and square, and the triangle waveforms, respectively). As previously mentioned, unlike in the case of DC electrospinning, AC jets appear at every half-cycle (positive and negative) when the voltage is increased. Subsequently, only a small number of the previously created jets are quenched at the end of the half-cycle following a decrease in the amplitude [23], [27]. The time interval (Δt)

between the change in the positive and negative sub-critical voltage is significantly longer at lower frequencies (i.e. higher wavelengths), thus acting to influence the creation of jets. This time interval is relatively more prominent in the triangle (Δt_T) than in the sine and square waveforms (instantaneous) (Fig. 4.12a). Consequently, the 10 Hz triangle waveform struggled to form jets, thus negatively affecting the degree of spinnability. In other words, if the frequency of the waveform is too low, the polymeric jet may become dominated by a single polarity (either positive or negative) over a longer time [26]. Conversely, if the frequency is relatively high, the polymeric jet is subjected to the rapid alteration of positive and negative charge polarities. Hence, the transfer of charges to the liquid may not be fast enough to create the critical electric pressure required for stable electrospinning, which could also be the reason for the cessation of the spinnability of PCL at higher frequencies.

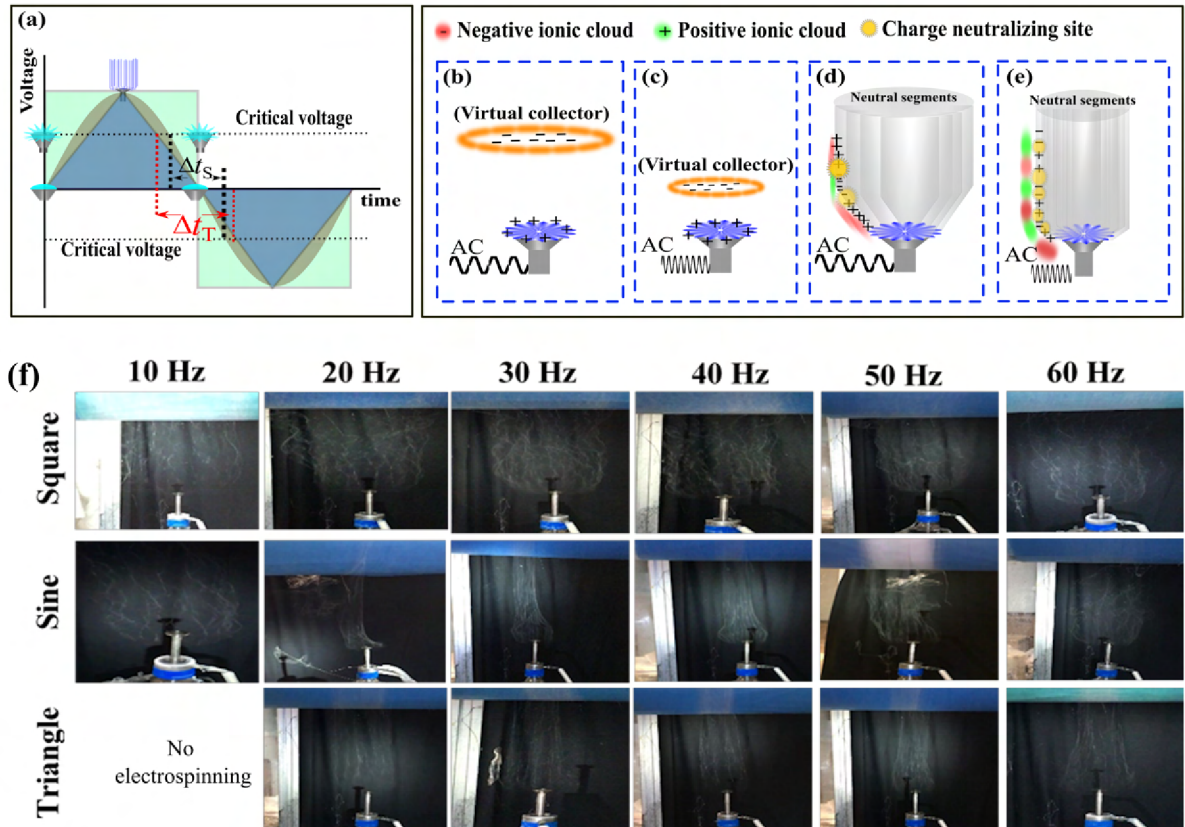


Figure 4.12: (a) *Electrohydrodynamic instability and jet ejection as a function of the time and voltage for various waveforms (Δt_S and Δt_T is the time interval between changes in the voltage polarity for the sine and triangle waveforms, respectively); (b) and (c), the generation of a virtual collector at lower and higher frequencies, respectively; (d) and (e), the formation of a fibrous plume and the charge neutralizing point at lower and higher frequencies, respectively; and (f), image of a nanofibrous plume with various waveforms and at various frequencies.*

One of the most critical parameters with regard to DC electrospinning spinnability and the fiber morphology concerns the distance between the spinneret and the collector since this distance directly influences a number of processes, e.g. the strength of the electric field, instability (whipping and stretching) and the evaporation of the solvent [126]. With concern to AC electrospinning, the placement of the virtual collector is primarily determined by the frequency of the waveform since it controls the length of the charged segments of the jet [23]. Charged segments following the application of lower frequencies are longer than those for higher frequencies. Thus, a virtual counter electrode (ionic cloud) is formed at a greater distance from the vicinity of the electrode at lower frequencies than at higher frequencies (Fig. 4.12b and 4.12c), thus resulting in the formation of a wider fibrous plume with a lower fiber density (Fig. 4.12d). In contrast, a smaller plume with a higher fiber density is initiated upon an increase in the frequency due to the shorter distance between the spinneret and the virtual collector (Fig. 4.12e). Moreover, the square waveform was found to result in the creation of a relatively larger fibrous plume than did the sine and triangle waveforms. (Fig. 4.12f). Therefore, in order to obtain a steady jet, it is essential that the critical distance be determined between the virtual collector and the spinneret. Since the critical distance is a function of the frequency, the formation of jets is inhibited below or above certain frequency intervals.

4.2.3 Impacts of the AC high-voltage signal waveform and frequency on the electrospun fibers morphology

The morphology of PCL ENF as a function of the waveform and frequency was analyzed by means of SEM, as illustrated in Fig. 4.13. All the triangle waveform frequencies resulted in smooth fibers, whereas just the 30 and 50 Hz sine waveforms led to the creation of spindles and beads on the fibers. Interestingly, the square waveform generated trimodal-structured ENF consisting of spherical beads, spindle-like beads and helical electrospun fibers (Fig. 4.13, 4.14 and Fig. A.3). As shown in Fig. 4.14e, spherical or spindle-like beads are defined depending on the aspect ratio of L/W . The gradual voltage variation of the triangle waveform facilitated the formation of smooth fibers, whereas concerning the square waveform, oscillations of the voltage polarity were instantaneous. Nevertheless, the maximum voltage was steady at certain time intervals for the square waveform at both the positive and negative amplitudes in contrast to the triangle and sine waveforms.

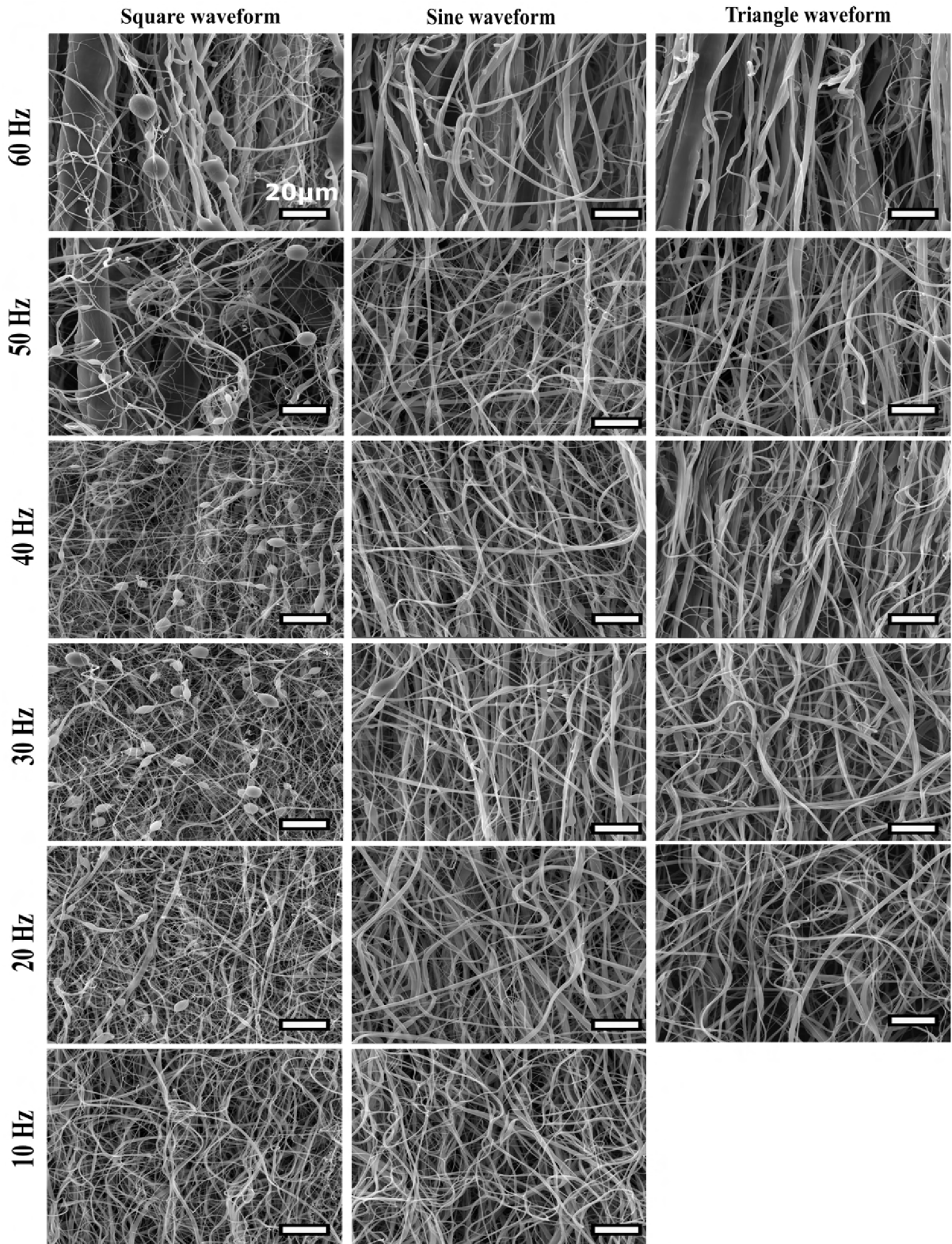


Figure 4.13: SEM images of the PCL ENF as a function of the various waveforms and frequencies of AC high voltage signal (50 kV_{RMS}).

The instantaneous alteration of the square waveform voltage polarity (i.e. the series of Heaviside jumps) led to sudden increases and decreases in the electric pressure. Thus, the capillary force dominates whenever the electric pressure drops, which causes the cylindrical jet to collapse, thereby encouraging the formation of a spherical shape so as to attain the smallest surface area. When the electric pressure subsequently increases, the spherical shape of the jet again changes to a cylindrical shape due to the charge repulsion, which results in the formation of beads along the string fibers. Due to its steady instantaneous voltage, the square waveform stimulates a greater number of charge densities on the jet than do the other two waveforms. Concerning the higher frequency square waveform, the maximum instantaneous voltage value lasts for a shorter time scale than for the lower frequency. Hence, increasing the frequency of the square waveform, which stimulates higher net charges, leads to the creation of a large number of charge neutralizing points in the jet (Fig. 4.12 on page 77e and Fig. 2.7 on page 26). Since most of the charges are neutralized, the jet is subjected to a lower degree of stretching during flight (Fig. 4.15b). Moreover, the charge neutralization of the jet leads to tension within the fiber, the extent of which depends on the repulsion or attraction of the net charge. In addition, the interaction between the electric field and the net charge also acts to increase the fiber tension, which stimulates the formation of a beaded nanofibrous structure [127]. Subsequently, curled or helical fibers are formed in an effort to minimize the surface energy once the tension in the fibers has been relieved [127].

The 10 Hz square waveform produced smooth fibers without beads due to the enhanced stretching of the jet during the application of single polarity over a longer time period (Fig. 4.15b). In addition, a decrease in the applied frequency of the square waveform led to behavior similar to that observed in DC electrospinning. Zolfagharlou et al. demonstrated a similar morphology following the application of an identical solvent system using the DC electrospinning approach for the production of PCL fibers [128]. Hence, all the afore-mentioned phenomena corresponded to the suggested hypothesis.

The stereological method (Eq 3.8 on page 50) was used to evaluate the number of beads and spindles per unitary length as a function of the frequency. Fig. 4.13 clearly shows that the applied frequency of the waveform is able to change the morphology of the electrospun fibers and, thus, the resulting number of beads and spindles (Fig. 4.14). Generally, the number of beads and spindles per unitary length initially increases and then gradually decreases with increases in the frequency of the square waveform; this transition occurs at 30 Hz and 40 Hz for beads and spindles, respectively. The increase may be due to the increase in the frequency, which favors less stretching and high charge neutralization, which

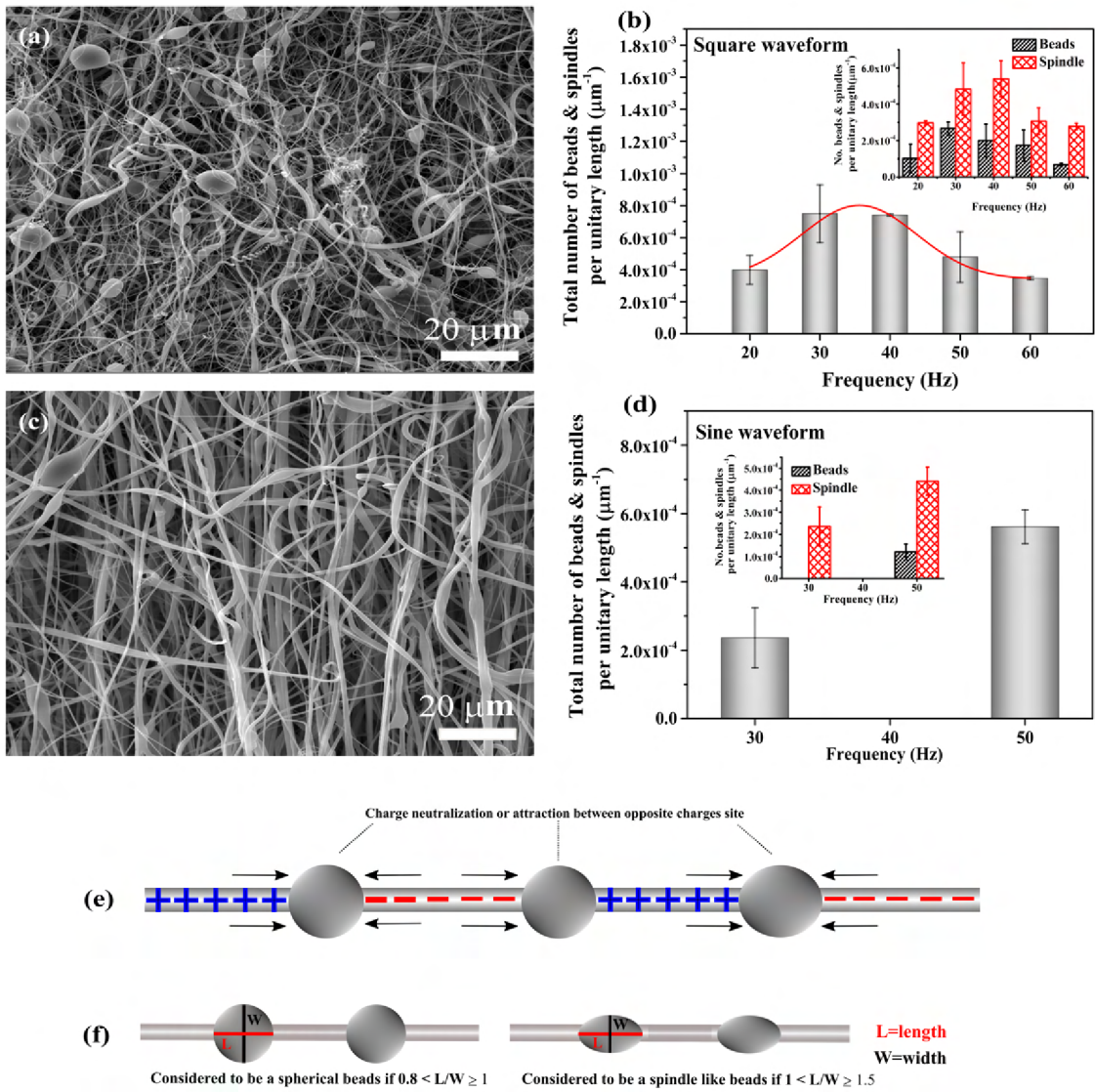


Figure 4.14: (a) and (c), SEM images of PCL ENMs at 30 Hz for the square and sine waveforms, respectively; (b) and (d), the total number of beads and spindles per unitary length with respect to the frequency of the square and sine waveforms, respectively. The inserts in (b) and (d) show the number of beads and/or spindles per unitary length as a function of the frequency; (e) mechanism of bead or spindle formation, and (f) Schematic illustration of spherical and spindle-like beads, which were defined using the aspect ratio of length (L) and width (W) of the beads.

in turn results in the presence of beads and spindles on the fiber. Above this frequency, the jet begins to struggle to stretch freely due to the presence of differing charges; as a result, a thicker fiber is formed, which inhibits the bead and spindle formation mechanism. In the case of the sine waveform, 30 Hz resulted in spindles only, while 50 Hz resulted in a combination of beads and spindles on the fiber. No explanation has yet been determined for this tendency.

The impact of the waveform and the frequency on the morphology of ENF was also reflected in the diameter distributions thereof (Fig. 4.15a and 4.15c). The mean fiber diameter of PCL ENF increased from 0.96 ± 0.4 to 2.1 ± 1.9 μm with an increase in the frequency of the triangle waveform from 20 to 60 Hz. On the other hand, the square waveform acted to reduce the fiber diameter from 0.55 ± 0.2 to 0.34 ± 0.25 μm for the range 10 to 30 Hz and, subsequently, it increased from 0.58 ± 0.33 to 1.27 ± 2.1 μm for the range 40-60 Hz. Interestingly, the fiber diameter oscillated periodically in the frequency range 10 to 60 Hz of the sine waveform; it increased from 0.98 ± 0.35 to 1.1 ± 0.4 μm for the 10 to 30 Hz range and subsequently decreased to 0.83 ± 0.38 μm at 40 Hz. From 40 Hz, the ENF diameter again increased to 0.86 ± 0.52 μm and 1.23 ± 0.52 μm at 50 and 60 Hz, respectively.

Higher frequencies supported the formation of thicker fibers; each increase in the frequency acted to shorten the time interval (or difference in the period) between every half cycle for the formation of the jet, which resulted in a reduction in the time available for the whipping motion. At higher frequencies, the reduction in the whipping instability was also caused by the formation of a virtual collector in the vicinity of the spinneret (Fig. 4.12c and 4.15b). The jet exhibited a limited whipping motion due to the short distance between the virtual collector and the electrode (Fig. 4.15b). Moreover, the restriction of the time for the complete evaporation of the solvent during the deposition of the fibers resulted in the thickening of some of the neighboring fibers as a result of coagulation [90]. With respect to DC electrospinning, it is evident that the electrode to collector distance plays a critical role in determining the diameter of ENF [129], [130].

The Box-Whisker plots (Fig. 4.15a) illustrates that the 95 percentile of the fiber diameter was below 2.25, 2.5 and 5.5 μm for the sine, square and triangle waveforms, respectively (see Fig. 4.15a at 60 Hz). However, the thicker fibers, which were fabricated using the square, triangle and sine waveforms (24, 16 and 3.25 μm , respectively) acted to increase the mean fiber diameters and standard deviations (see Fig. 4.15a at 60 Hz). He *et al.* studied the theoretical scaling relationship between the AC frequency (Ω) and the fiber radius (r), and demonstrated that $r \sim \Omega^{1/4}$ [131]. The experiments conducted did not confirm the relationship between the frequency and the fiber diameters, most likely due to the narrow range of frequencies. Nevertheless, this relationship was observed in the case of the triangle waveform. Mirek *et al.* conducted an experiment applying a pulsed voltage aimed at the study of the impacts thereof on the fiber diameter [132]. They concluded that increases in the frequency resulted in the reduction of the fiber diameter. However, their research was conducted applying a single polarity pulsed voltage or, in other words,

in contrast to this study, without changes in the polarity of the voltage.

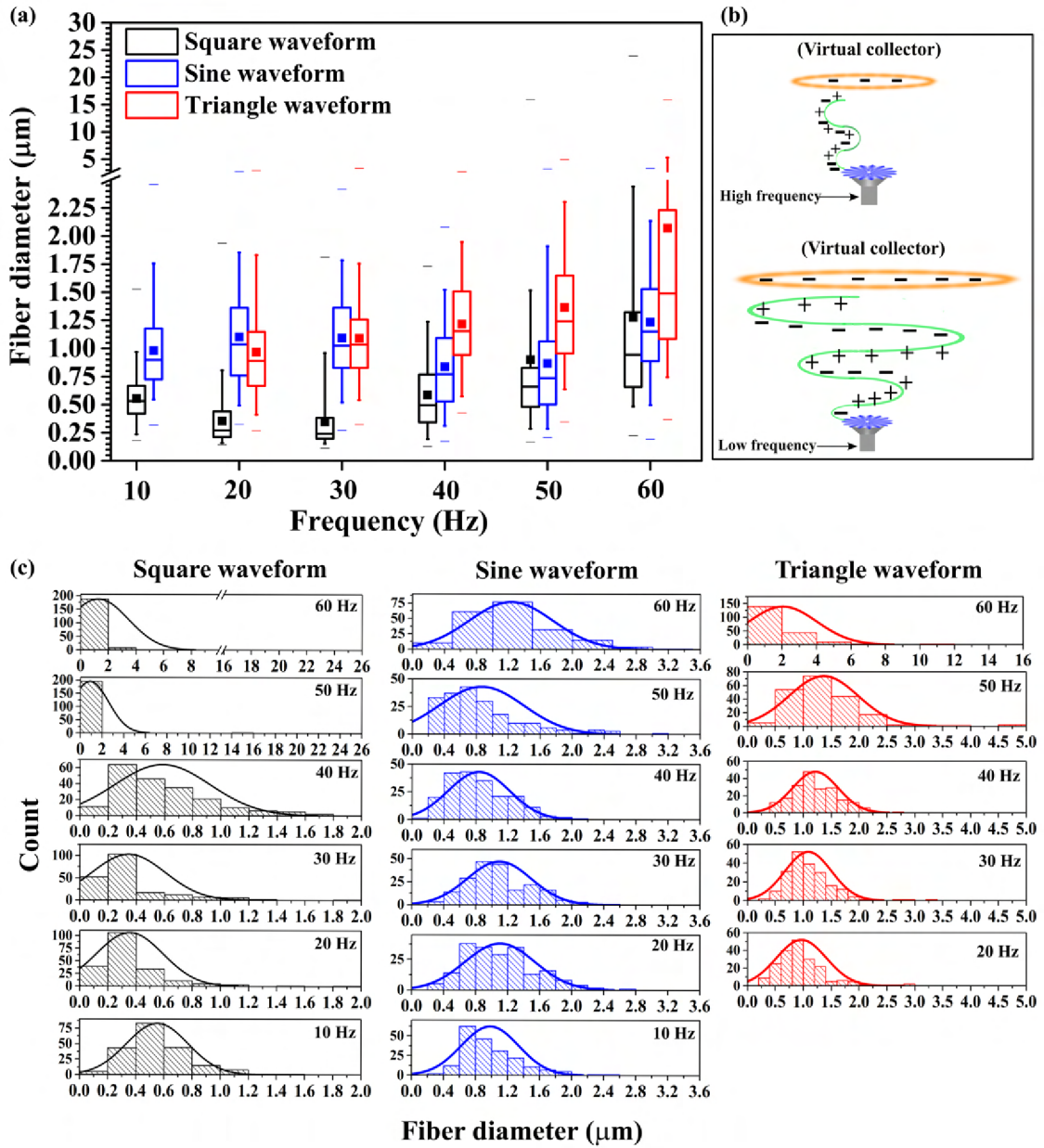


Figure 4.15: (a) Fiber diameter as a function of the various waveforms and frequencies of the AC high-voltage signal, (b) polymeric jet at lower and higher frequencies, and (c) histogram plots with normal distribution curve showing the PCL fiber diameter as a function of the various waveforms and frequencies of the AC high-voltage signal. The solid squares in the box represent the mean values, while the lower, middle, and upper limits correspond to the first (25%), second (50%) and third (75%) quartiles, respectively. The lower and upper whiskers represent 5% and 95%. The minimum and maximum values are denoted as '-'. (Since considerable variations in the fiber diameter between the samples, instead of using the same axis scale for all samples, they were auto-scaled for better visualizations).

4.2.4 Effects of the AC high-voltage signal waveform and frequency on productivity

The throughput of the PCL nanofibers as a function of the various waveforms and frequencies is illustrated in Fig. 4.16 (measurements method can be seen in Section 3.2.8 on page 47). The waveforms and frequencies exerted a significant impact on the productivity of the nanofibers. When the frequency was increased from 10 to 50 Hz, the corresponding nanofiber yield increased simultaneously from 7.9 ± 0.27 to 23.60 ± 0.43 g/h and 4.30 ± 0.11 to 16.52 ± 0.26 g/h for the square and sine waveforms, respectively. The same trend was observed for the triangle waveform; a frequency increase from 20 to 50 Hz resulted in a yield increase of 2.56 ± 0.31 to 6.89 ± 0.16 g/h. A higher throughput was attained at 50 Hz for all three waveforms. In contrast, the productivity of nanofibers decreased slightly above this value, i.e. from 23.60 ± 0.43 g/h to 21.83 ± 0.24 g/h, 16.52 ± 0.26 g/h to 15.47 ± 0.17 g/h, and 6.89 ± 0.16 g/h to 6.04 ± 0.17 g/h for the square, sine and triangle waveforms, respectively. This observation was attributed to the characteristic skin effects of the AC waveform [133], which acts to reduce productivity at higher frequencies ($60 \text{ Hz} \geq$) due to the accumulation of charge densities at the edges of the spinneret instead of over the entire surface which, in turn, acts to reduce the area of charge densities towards the edges.

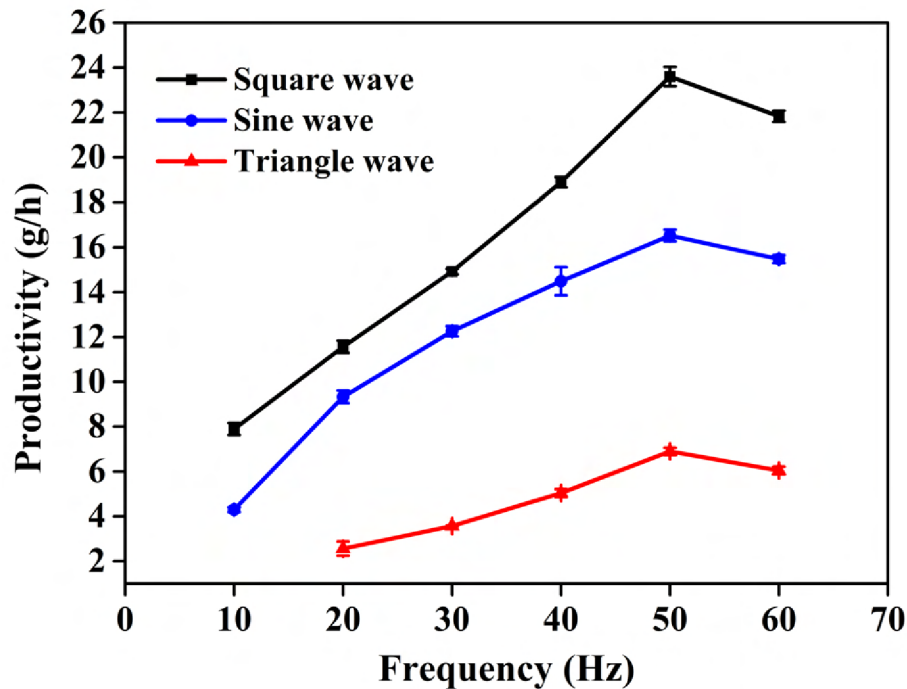


Figure 4.16: Productivity of the PCL ENF as a function of the various waveforms and frequencies of AC high voltage signal (50 kV_{RMS}).

The effects of the frequency on the skin depth (δ) are represented by the equation $\delta = \frac{1}{\sqrt{\sigma\pi f\mu}}$, where σ is the electrical conductivity, f corresponds to the frequency of the waveform, and μ is the permeability of the conductor [133]. The square waveform evinced a higher productivity rate, followed by the sine and then the triangle waveforms. As discussed previously, the polarity change time scale is instantaneous and steady with respect to the square waveform, which acts to encourage a higher degree of hydrodynamic instability on the surface of the liquid. Subsequently, more jets emerged when the frequency was increased from 10 to 50 Hz. The lower productivity at 60 Hz can be attributed to the shallow skin depth and the rapid extrusion of the liquid at the edges. In other words, the rapid movement of liquid molecules at the edges is less likely to be affected by the electric forces at higher frequencies due to the shallow/limited extent of the charge density area.

4.2.5 Effects of the AC high-voltage signal waveform and frequency on the chemical structure of PCL

The potential impacts of the waveform and frequency on the chemical structure and composition of PCL ENF was examined via the FTIR spectra (Fig. 4.17). Detailed information on the spectral bands of PCL can be found in Chapter 4.3.5 on page 97.

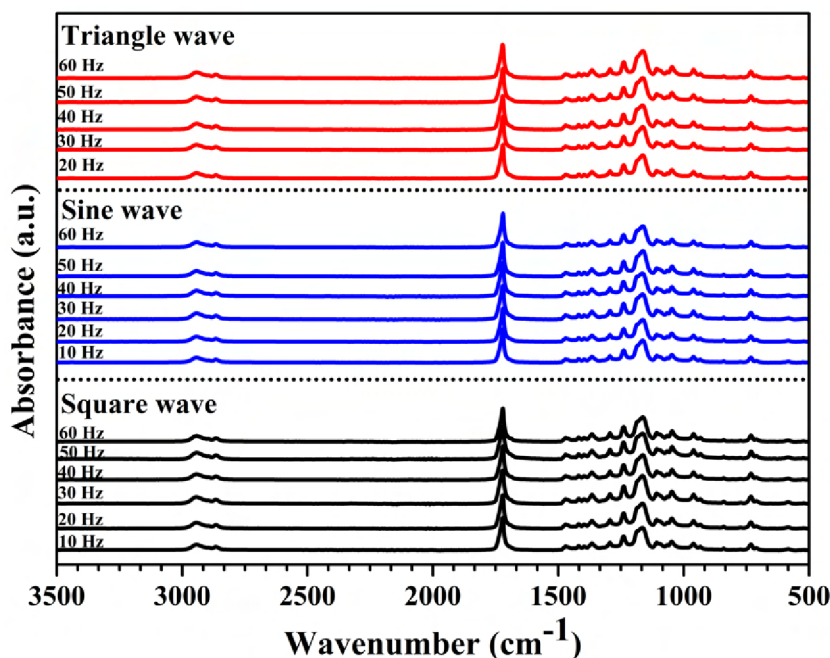


Figure 4.17: *FTIR spectra of PCL ENF as a function of the various waveforms and frequencies of AC high voltage signal (50 kV_{RMS}).*

The lack of apparent changes to the spectra indicated that the chemical structure of the PCL was not affected by either the waveform or the frequency. Hence, the FTIR spectra showed that while the waveform and the frequency are able to affect both the morphology and the productivity, they do so without compromising the original chemical structure of the PCL. Herein, interesting to point out that, although the polymeric liquid in the electric field continuously interacts with the surrounding ions, free electrons, as well as the X-ray [134, 135], the chemical structure of the polymer was not altered by them. This could be attributed to the following factors; (i) the concentration of these ions or free electrons is not sufficient enough to react with polymer, and (ii) there is very limited time for interaction between the polymeric liquid and the surrounding ions due to faster acceleration of jet and rapid solvent evaporation in the electric field. The FTIR spectra thus support the hypothesis that electrospinning technology did not alter the chemical structure of the polymer; however, it affects only the conformation of the macromolecule. Next section will discuss about how the high energy particles are affecting chemical groups of the PCL electrospun membranes as well as its bulk properties.

4.3 Plasma treatment effects on the bulk properties of PCL nanofibrous mats

This sub-chapter aims to investigate the effects of plasma treatment on the fabricated PCL ENMs morphology, wettability, surface functional groups, crystallite size, crystallinity, crystallization temperature, and melting temperature. In this study, three different types of PCL ENMs resulting from different solvent systems (F, FA and FAA) is plasma-treated at medium pressure using a dielectric barrier discharge (DBD) with adjusted treatment time and discharge gases (argon and nitrogen). Changes in surface and bulk properties of the PCL ENMs due to the performed plasma treatments are analyzed using water contact angle (WCA) analysis, scanning electron microscopy (SEM), X-ray photoelectron spectroscopy (XPS), X-ray diffraction (XRD), Fourier-transform infrared (FTIR) spectroscopy, and differential scanning calorimetry (DSC).

4.3.1 Experimental conditions

All experimental details can be found in Chapter 3. The parameters that are specifically used in this chapter are summarized in Table 4.5 and 4.6.

Table 4.5: *Various spinning solutions and AC electrospinning processing parameters (F-PCL, FA-PCL and FAA-PCL means PCL dissolved in formic acid (F), formic acid/acetic acid (FA), and formic acid/acetic acid/acetone (FAA), respectively.)*

Precursor solution	F-PCL, FA-PCL and FAA-PCL
Polymer concentration	10 wt%
AC Electrospinning processing parameter	Spinneret's surface diameter: 2 cm Spinneret to collector distance: 22 cm Solution feeding rate: 18 mL/min Collector's peripheral speed: 40 m/min Applied voltage: 35 kV _{RMS} Waveform: Sine Frequency: 50 Hz Temperature: 21 – 23 °C Humidity: 42 – 45 %

Table 4.6: *Plasma treatment parameters*

Plasma treatment	Sample	Discharge power	Treatment time
		[W]	[s]
Argon plasma treatment	F-PCL	2.2	65
	FA-PCL	2.2	55
	FAA-PCL	2.2	60
Nitrogen plasma treatment	F-PCL	2.6	63
	FA-PCL	2.6	64
	FAA-PCL	2.6	61

4.3.2 Water contact angle (WCA) analysis

Water contact angle values of F-PCL, FA-PCL, and FAA-PCL ENMs before and after plasma treatment in argon and nitrogen were measured as a function of applied energy density to determine the effect of the used plasma treatments on the ENMs surface wettability (Fig. 4.18). Water droplets on nanofibers or any rugged hydrophobic surfaces usually exhibit one of the following states [136]: (1) the Wenzel state, in which water droplets are completely in contact with the rough surface [137] or (2) the Cassie state, in which water droplets are in contact with the rugged surface's peak as well as the air pockets which were trapped between the surface grooves [138]. Initially, the Cassie-Baxter state is observed when the water droplet is placed on the untreated ENMs as the water droplet is in contact both with the ENM surface as well as air pockets entrapped between the nanofibers [138]. The untreated PCL ENMs show WCA values of $135.6 \pm 3.2^\circ$, $132.7 \pm 3.4^\circ$, and $130.0 \pm 2.2^\circ$ which thus reveals the hydrophobicity of the pristine F-PCL, FA-PCL, and FAA-PCL ENMs respectively. The small difference in WCA values between the samples is due to changes in the electrospun fiber morphology and diameter, which significantly influence the surface roughness and the volume of the present air pockets [139]. Indeed, it is known from the literature that the WCA is inversely proportional to the fiber diameter. Consequently, the higher FAA-PCL diameter results in a larger contact area between the water droplet and the ENM surface, hence, a lower WCA value. Additionally, the FA-PCL sample shows a slightly higher WCA value because of its smaller fiber diameters, while the F-PCL ENM possesses the highest WCA due to the fact that it consists out of the smallest fibers. Fig. 4.18 reveals that after plasma treatments in argon and nitrogen, the WCA however strongly decreases with increasing energy density for all PCL ENMs under study. Nevertheless, at a particular energy density, a saturation effect of the plasma treatment on the ENMs is noticed, after which the WCA remains unchanged as a function of energy density. In other words, the water droplets on the

plasma-treated ENMs are in the Wenzel state as the water can penetrate the pores of the ENMs due to the incorporation of polar groups on the ENM surface as a result of plasma exposure [137].

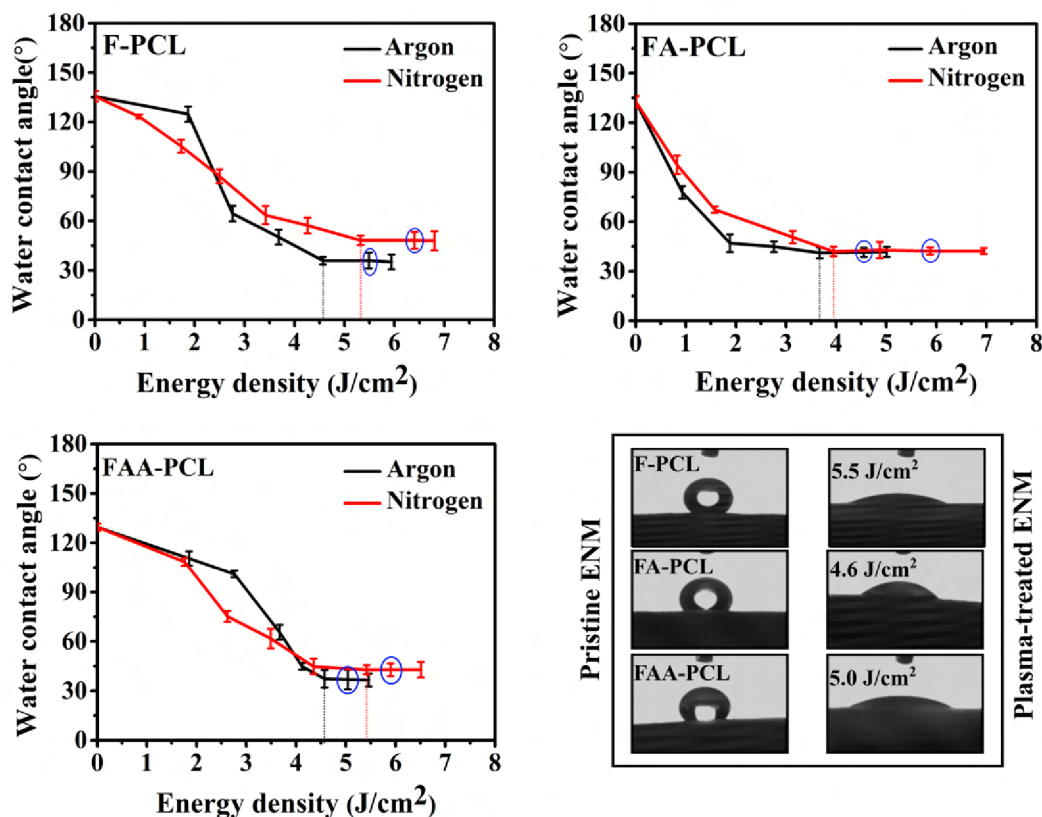


Figure 4.18: Evolution of the WCA on PCL ENMs surfaces as a function of energy density for Ar and N_2 plasma and images of water droplets placed on pristine and plasma-treated. The black and red lines indicate the starting saturation point of WCA for Ar and N_2 plasma-treated ENMs, respectively. The blue circle indicates the samples which were used for further analysis.

In the case of argon plasma, the lowest attainable WCA values on the plasma-modified F-PCL, FAA-PCL, and FA-PCL are $35 \pm 4.4^\circ$, $37 \pm 4^\circ$, and $41 \pm 2.8^\circ$ respectively, and these values are reached using an energy density of 4.6 J/cm^2 , 4.6 J/cm^2 , and 3.7 J/cm^2 respectively. The applied nitrogen plasma exposure also results into similar changes in WCA values on FA-PCL, FAA-PCL, and F-PCL where saturated WCA values of $42 \pm 2.9^\circ$, $43 \pm 2.8^\circ$, and $48 \pm 3.0^\circ$ are obtained at an energy density of 4.9 J/cm^2 , 5.4 J/cm^2 , and 5.3 J/cm^2 respectively. These results thus reveal that the argon plasma treatment is more effective in increasing the PCL ENM hydrophilicity and requires a lower energy density to reach this high wettability in comparison to nitrogen plasma exposure.

4.3.3 Surface morphological analysis of pristine and plasma-treated ENMs

The effect of argon and nitrogen plasma treatment on the F-PCL, FA-PCL, and FAA-PCL ENM surface morphology is examined and analyzed using SEM micrographs (Fig. 4.19).

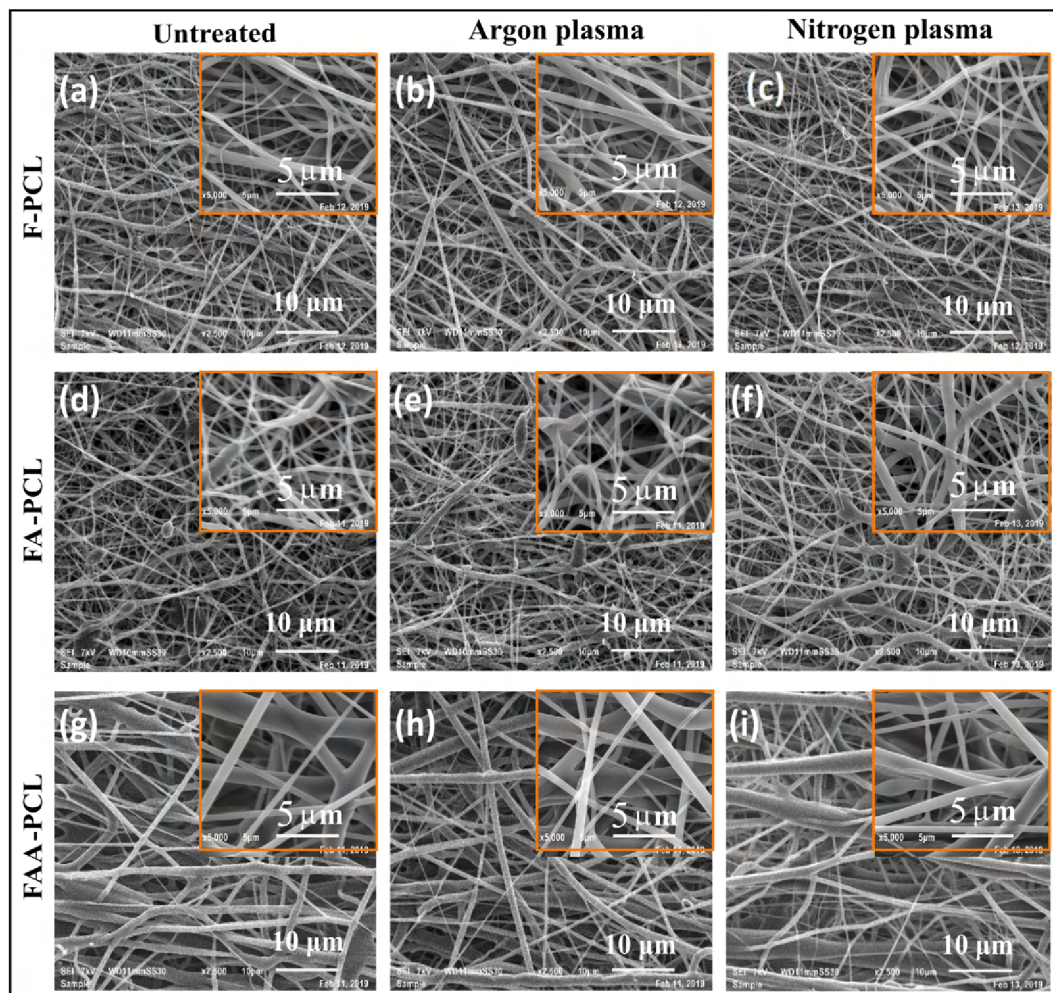


Figure 4.19: SEM images of untreated F-PCL (a), argon plasma-treated F-PCL (b), nitrogen plasma-treated F-PCL (c) at an energy density of 5.5 J/cm^2 & 6.4 J/cm^2 ; untreated FA-PCL (d), argon plasma-treated FA-PCL (e), nitrogen plasma-treated FA-PCL (f) at an energy density of 4.6 J/cm^2 & 5.6 J/cm^2 ; untreated FAA-PCL (g), argon plasma-treated FAA-PCL (h), nitrogen plasma-treated FAA-PCL (i) at an energy density of 5.0 J/cm^2 & 5.9 J/cm^2 ($X2500$ magnification for large images and $X5000$ magnification for small images).

The morphology of the pristine F-PCL, FA-PCL, and FAA-PC ENMs indicates interconnected and randomly oriented fibers with diameters in the nanoscale range. The observed SEM micrographs reveal smooth and beadless fibers for the F-PCL and FAA-PCL ENMs with an average fiber diameter of $248 \pm 95 \text{ nm}$ and $605 \pm 347 \text{ nm}$ respectively. On the

other hand, the FA-PCL ENM consists out of fibers with the presence of some beads and shows an average fiber diameter of 354 ± 118 nm. SEM micrographs of the PCL ENMs after argon and nitrogen DBD plasma treatment at saturation energy density are also presented in Fig. 4.19. These images clearly reveal that the original ENM surface topographies are maintained on the plasma-treated F-PCL, FA-PCL, and FAA-PCL samples as there are no obvious surface damages visible on the plasma-treated PCL ENMs. The SEM images thus clearly indicate that the applied argon and nitrogen plasma treatments can strongly increase the PCL ENMs surface wettability without compromising the ENMs morphology.

4.3.4 Surface chemical composition analysis

A similar set of saturated plasma-modified PCL ENM samples used to examine the surface morphology was also prepared in this study for further surface chemistry analysis by means of XPS (analyzing depth is upto 10 nm) [42]. In a first step, the surface atomic composition of pristine and plasma-treated PCL ENMs was quantified from the gathered XPS survey spectra (Fig. 4.20), and the obtained results are presented in Table 4.7. The surface atomic compositions of pristine F-PCL, FA-PCL, and FAA-PCL ENMs were dominated by carbon ($74.3 \pm 0.3\%$, $74.8 \pm 0.7\%$, and $75.2 \pm 0.1\%$ respectively) and oxygen ($24.7 \pm 0.3\%$, $25.2 \pm 0.7\%$, and $24.8 \pm 0.1\%$ respectively), which are all relatively close to the theoretically expected values (carbon 75% and oxygen 25%) for PCL.

Table 4.7: *The surface atomic composition of PCL ENMs before and after Ar or N₂ plasma treatment.*

Sample	C[%]	O[%]	N[%]
F-PCL	74.3 ± 0.3	24.7 ± 0.3	–
Ar-F-PCL	69.1 ± 0.4	30.9 ± 0.4	–
N ₂ -F-PCL	67.0 ± 0.3	20.0 ± 0.9	12.9 ± 1.2
FA-PCL	74.8 ± 0.7	25.2 ± 0.7	–
Ar-FA-PCL	69.9 ± 0.6	30.0 ± 0.5	–
N ₂ -FA-PCL	64.2 ± 0.9	25.5 ± 0.2	10.3 ± 1.1
FAA-PCL	75.2 ± 0.1	24.8 ± 0.1	–
Ar-FAA-PCL	72.0 ± 0.3	27.9 ± 0.3	–
N ₂ -FAA-PCL	65.0 ± 0.7	20.8 ± 0.9	14.2 ± 1.7

From Table 4.7, it is also clear that, after argon plasma treatment, a considerable increase in oxygen content on the F-PCL, FA-PCL, and FAA-PCL ENMs occurs. Due to the incorporation of oxygen, the relative carbon content also decreases upon argon

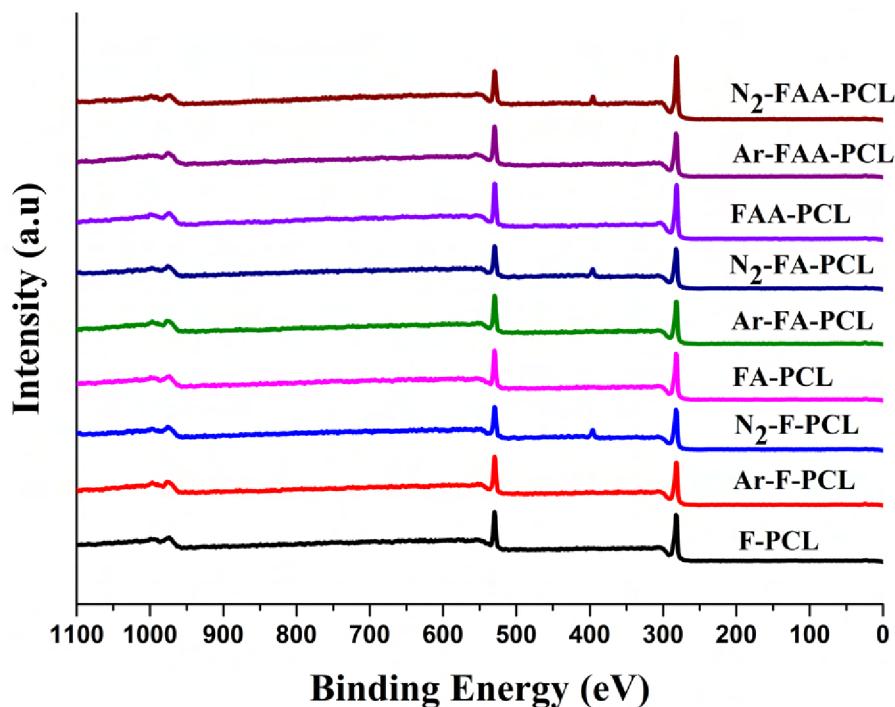


Figure 4.20: XPS survey spectra of pristine and plasma-treated PCL ENMs.

plasma treatment. In the case of nitrogen plasma treatment, the nitrogen content on F-PCL, FA-PCL, and FAA-PCL ENMs is strongly increased from 0% to $12.9 \pm 1.2\%$, $10.3 \pm 1.1\%$, and $14.2 \pm 1.7\%$ respectively showing the large incorporation of nitrogen atoms to the ENMs surface during nitrogen plasma exposure. At the same time, nitrogen plasma treatment decreases the relative carbon and oxygen content on the PCL ENMs due to the incorporation of a significant amount of nitrogen. From these results, it can thus be concluded that the applied argon plasma treatment results in the incorporation of oxygenated surface groups to the PCL surface, while nitrogen plasma treatment incorporates nitrogen-containing functional groups.

To evaluate how the surface functional groups were exactly modified on the PCL ENMs by the conducted argon and nitrogen plasma treatments, XPS high-resolution C1s spectra were deconvoluted. Images of these deconvoluted high-resolution C1s spectra and the calculated relative amounts of the carbon-containing functional surface groups are presented in Fig. 4.21 and 4.22 respectively. As seen from Fig. 4.21, the high-resolution C1s spectra of the pristine PCL ENMs are fitted by three peaks: (1) a peak at a binding energy of 284.8 eV corresponding to carbon-carbon and hydrocarbon bonds (C-C/C-H), (2) a peak at 286.4 eV corresponding to carbon single bonded to oxygen (C-O), and (3) a peak at 288.8 eV attributed to esters or carboxylic acids (O-C=O). Among the three pristine PCL ENM samples, only in F-PCL also a small peak at 290.4 eV related to C-Cl con-

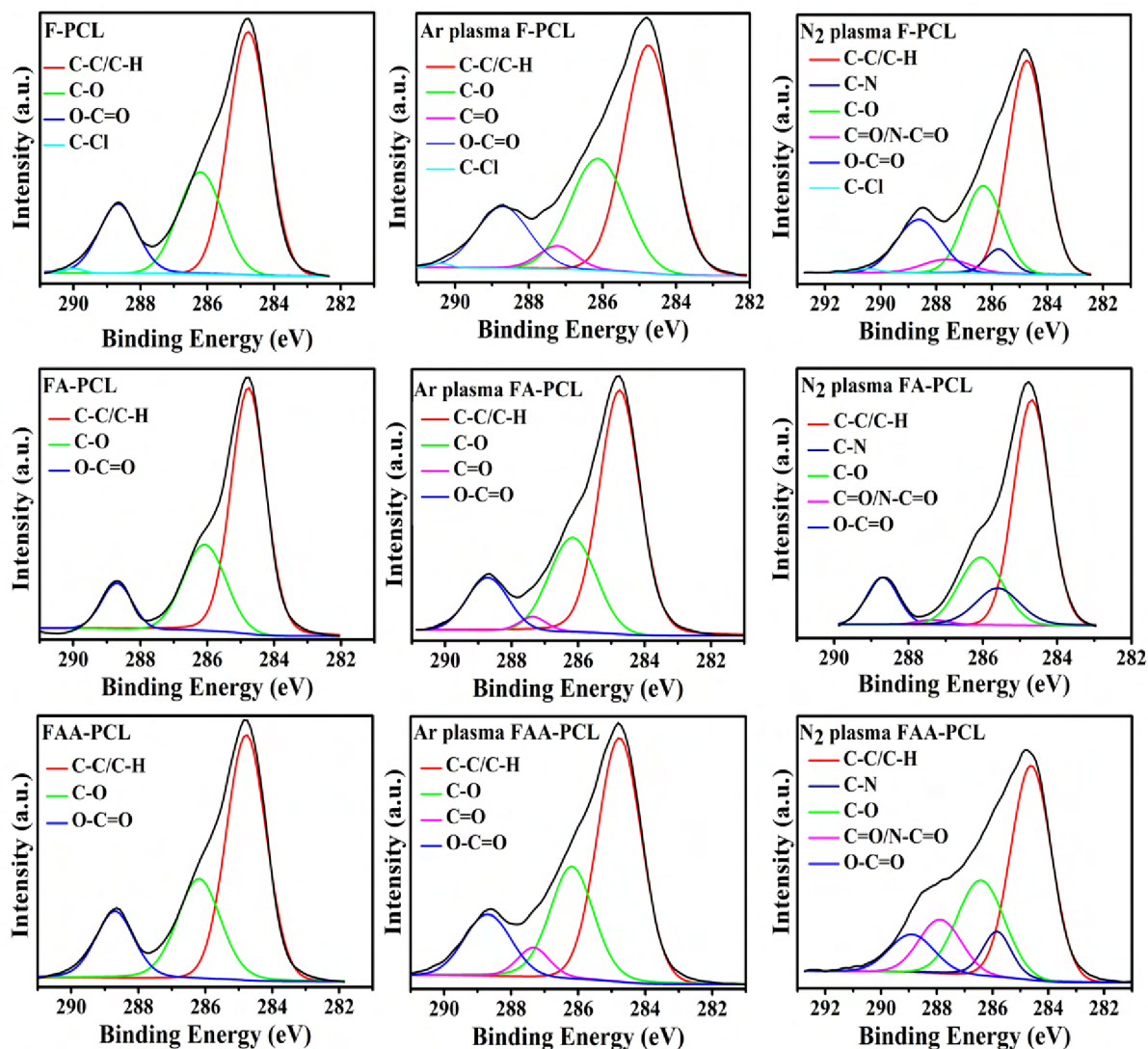


Figure 4.21: *Deconvolution of high-resolution $C1s$ peaks of PCL ENMs before and after plasma treatments.*

tamination could be observed, however, its relative concentration was typically less than 0.5%. After argon plasma treatment of all PCL samples under study, similar peaks as for the untreated PCL samples are visible, while also a new peak at 287.6 eV assigned to C=O bonds could be observed. Fig. 4.22 also shows that argon plasma treatment results in a decrease in the relative concentration of the C-C/C-H peak after plasma exposure of all PCL samples under study in combination with an increase in the amount of C-O and C=O bonds. At the same time, the O-C=O peak also increases on the FAA-PCL sample, while this peak decreases on the F-PCL and FA-PCL samples after argon plasma treatment. It can thus be concluded that the conducted argon plasma treatments result in the incorporation of C-O and C=O bonds on all PCL ENMs and the additional incorporation of O-C=O groups on the FAA-PCL sample. It is also important to mention

that due to the hydrolytic behavior of the F and FA solvent system, the relative O–C=O concentrations in F–PCL and FA–PCL are higher and the C–C peak concentration is lower than in the case of FAA–PCL [106].

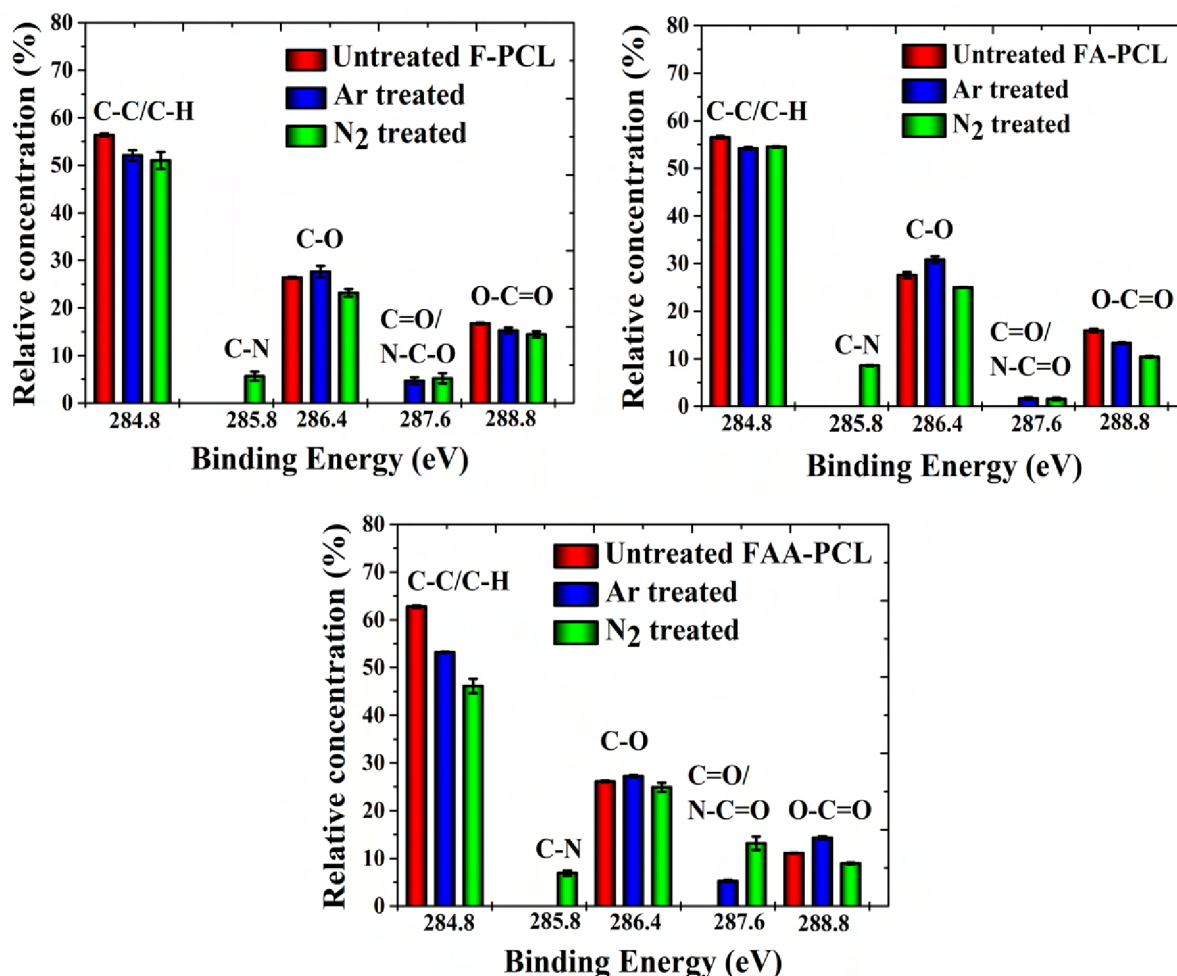


Figure 4.22: *Relative concentrations of the carbon-containing functional groups on untreated and plasma-treated PCL ENMs, as quantified from deconvoluted C1s high-resolution XPS spectra.*

To investigate the effect of the nitrogen plasma treatment, the high-resolution C1s spectra of the nitrogen plasma-treated ENMs are deconvoluted into five distinct peaks (see Fig. 4.21): the three peaks used for the pristine PCL samples and two additional peaks at a binding energy of 285.8 eV and 287.6 eV which are assigned to C–N bonds and N–C=O/C=O bonds respectively. As the difference in chemical shifts between N–C=O and C=O groups is relatively small, it is very difficult to differentiate between N–C=O and C=O. Fig. 4.22 reveals that after nitrogen plasma treatment, the relative concentrations of the C–C/C–H, C–O, and O–C=O bonds decrease for all PCL samples. However, nitrogen plasma treatment also results in the incorporation of new C–N and N–C=O/C=O

groups on the ENMs surfaces. Taking into account the fact that the nitrogen content increases and the oxygen content decrease upon nitrogen plasma treatment, it is most likely that mainly C–N and N–C=O groups are incorporated on the PCL samples instead of C=O groups. It is thus evident from the gathered XPS results that the improved wettability of plasma-treated PCL ENMs is due to the incorporation of nitrogen-containing functional groups (C–N & N–C=O) by nitrogen plasma treatment and oxygen-containing functional groups (C–O & C=O) by argon plasma treatment.

4.3.5 Crystal size and crystallinity analysis of PCL ENMs

XRD patterns of PCL ENMs were determined to investigate the crystallite size of F–PCL, FA–PCL, and FAA–PCL ENMs before and after plasma treatments, and the obtained results are shown in Fig. 4.23.

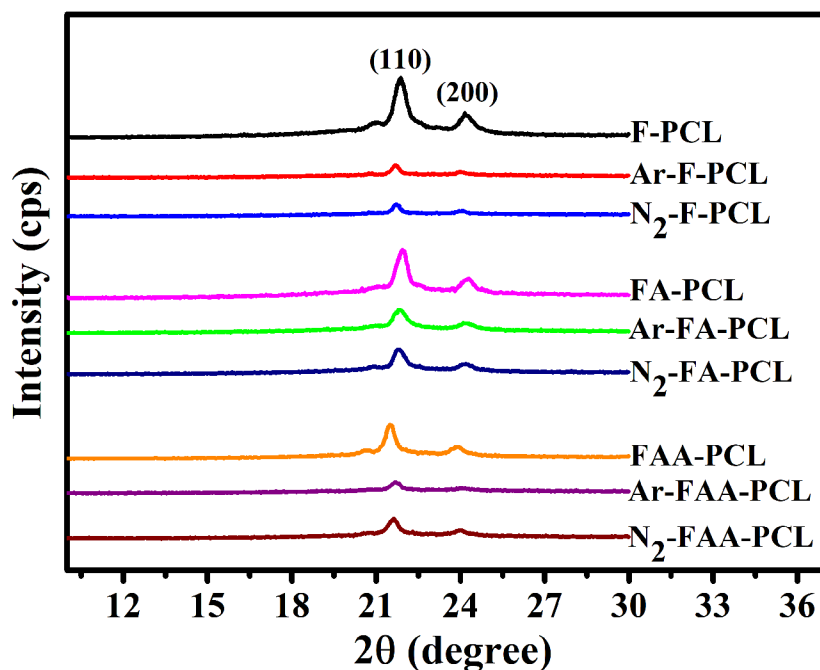


Figure 4.23: XRD patterns of untreated and plasma-treated PCL ENMs ((110) and (200) represents the diffraction planes).

The XRD patterns of PCL ENMs reflect two distinct sharp peaks at $\sim 21.4^\circ$ and $\sim 24^\circ$, which were indexed to be (110) and (200) diffraction planes of an orthorhombic crystalline of PCL [140–142]. However, as there were no extra peaks observed after the plasma treatment it can be concluded that the plasma treatments do not significantly affect the crystalline structure of PCL. From the XRD patterns, the crystallite size D was determined using Eq. 3.9 on page 51 and the calculated values are shown in Table 4.8 on the

next page. It can be observed that the conducted plasma treatments do not significantly affect the crystallite size of F-PCL and FA-PCL. In contrast, the FAA-PCL crystallite size is increased from 19.2 nm for the untreated sample to 24.0 nm, and 23.3 nm for the argon and nitrogen plasma-treated samples respectively (Table 4.8). We conjecture that the crystal size increases due to the following factors: (i) the crystallization temperature of FAA-PCL $23.9 \pm 1.6^\circ\text{C}$ is nearly close to room temperature. Hence, PCL molecular chains might have the opportunity to rearrange either during plasma treatment or after plasma treatment; and (ii) the newly incorporated surface functional groups act as nucleating sites for crystal growth which further leads to lamellar thickening or an increase in crystal size [114, 143–149].

Table 4.8: XRD diffraction peaks of PCL electrospun [2θ], crystallite size [D], crystallization temperature [T_c], melting temperature [T_m], crystallinity calculated from DSC [X_c], and crystallinity calculated from FTIR [χ_c].

Sample	2θ [$^\circ$]	D [nm]	T_c [$^\circ\text{C}$]	T_m [$^\circ\text{C}$]	X_c [%]	χ_c [%]
F-PCL	21.9	17.5	32.9 ± 0.2	63.4 ± 1.0	57.7 ± 1.7	55.4 ± 2.5
Ar-F-PCL	21.7	18.5	33.5 ± 0.3	62.6 ± 2.2	58.3 ± 1.8	56.1 ± 0.1
N ₂ -F-PCL	21.6	17.0	33.9 ± 0.2	62.2 ± 1.0	58.9 ± 1.9	55.9 ± 0.1
FA-PCL	21.9	16.5	25.2 ± 2.9	62.9 ± 1.3	55.8 ± 0.7	55.0 ± 1.7
Ar-FA-PCL	21.9	14.2	35.1 ± 1.3	63.7 ± 0.5	58.7 ± 1.8	56.6 ± 0.2
N ₂ -FA-PCL	21.9	16.1	33.2 ± 0.9	62.6 ± 0.2	57.8 ± 0.3	55.3 ± 1.9
FAA-PCL	21.5	19.2	23.9 ± 1.6	62.9 ± 0.4	53.9 ± 0.9	54.0 ± 3.5
Ar-FAA-PCL	21.7	24.0	33.9 ± 0.9	61.0 ± 0.1	54.1 ± 2.1	51.9 ± 0.1
N ₂ -FAA-PCL	21.7	23.3	23.4 ± 0.4 34.2 ± 0.2	61.7 ± 0.4	53.2 ± 1.9	55.3 ± 0.1

The FTIR spectra of pristine and plasma treated PCL ENMs prepared with different solvent systems are presented in Fig. 4.24. The functional group region of the FTIR spectra shows peaks attributed to asymmetric and symmetric stretching of C–H bonds in methylene groups at 2947 and 2867 cm^{-1} and a sharp peak at 1725 cm^{-1} due to stretching of ester carbonyl groups (O–C=O) in the amorphous and crystalline regions of PCL. Fig. 4.24 also reveals that the FTIR spectra of the plasma-modified PCL ENMs are not different from the FTIR spectra of the pristine PCL samples, which is due to the fact that

plasma treatment only modifies the top surface nanolayers of the samples. As the penetration depth of FTIR is significantly larger (~ 600 nm), changes in the top surface layers cannot be detected with this technique [42]. To obtain more information on the crystallinity of the PCL ENMs, the sharp FTIR peak at 1725 cm^{-1} can be deconvoluted into two peaks: a peak at 1735 cm^{-1} corresponding to the amorphous PCL phase and a peak at 1725 cm^{-1} attributed to the crystalline phase. The intensities of these two peaks (I_{1735} & I_{1725}) are further used to predict the crystallinity ($\chi_c = [I_{1725}/I_{1725} + I_{1735}] \times 100\%$) of the PCL ENMs and the obtained results are shown in Table 4.8 [150]. The gathered data reveal that the conducted plasma treatments do not significantly affect the degree of crystallinity (χ_c) of the PCL ENMs.

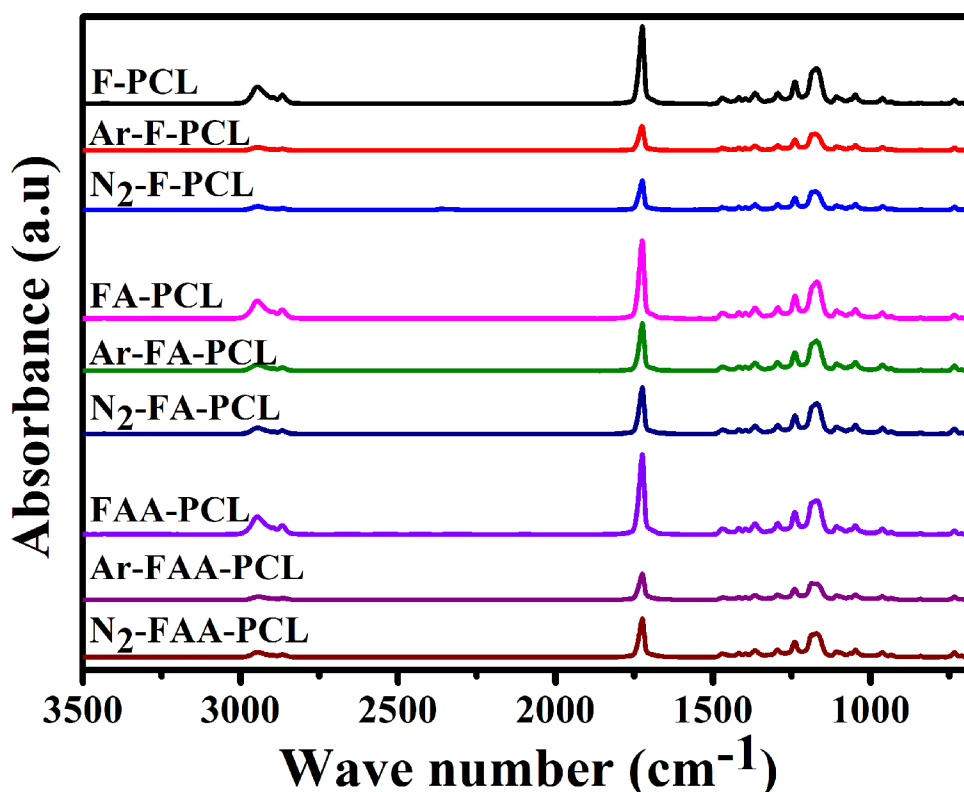


Figure 4.24: *FTIR spectra of pristine and plasma-treated PCL ENMs.*

Besides FTIR, also DSC analysis of the PCL ENMs has been performed and the DSC thermograms of the 1st heating and cooling scans of PCL ENMs are illustrated in Fig. 4.25. From these thermographs, the melting temperature (T_m) can be determined and the results are depicted in Table 4.8. As shown, the T_m values of F-PCL and FA-PCL ENMs are not significantly affected by the conducted plasma treatments nor by the used solvent system. On the other hand, performing plasma treatments on FAA-PCL ENMs slightly decreases the T_m value, as can be seen from the data presented in Fig. 4.25 and Table 4.8. This small decrease in T_m after plasma treatment could be attributed to the increase

in crystallite size observed for this sample (see Table 4.8) [143, 151, 152]. The fact that the T_m values were not affected by the plasma treatments in the case of the F-PCL and FA-PCL samples can also be explained by their unchanged crystallite size.

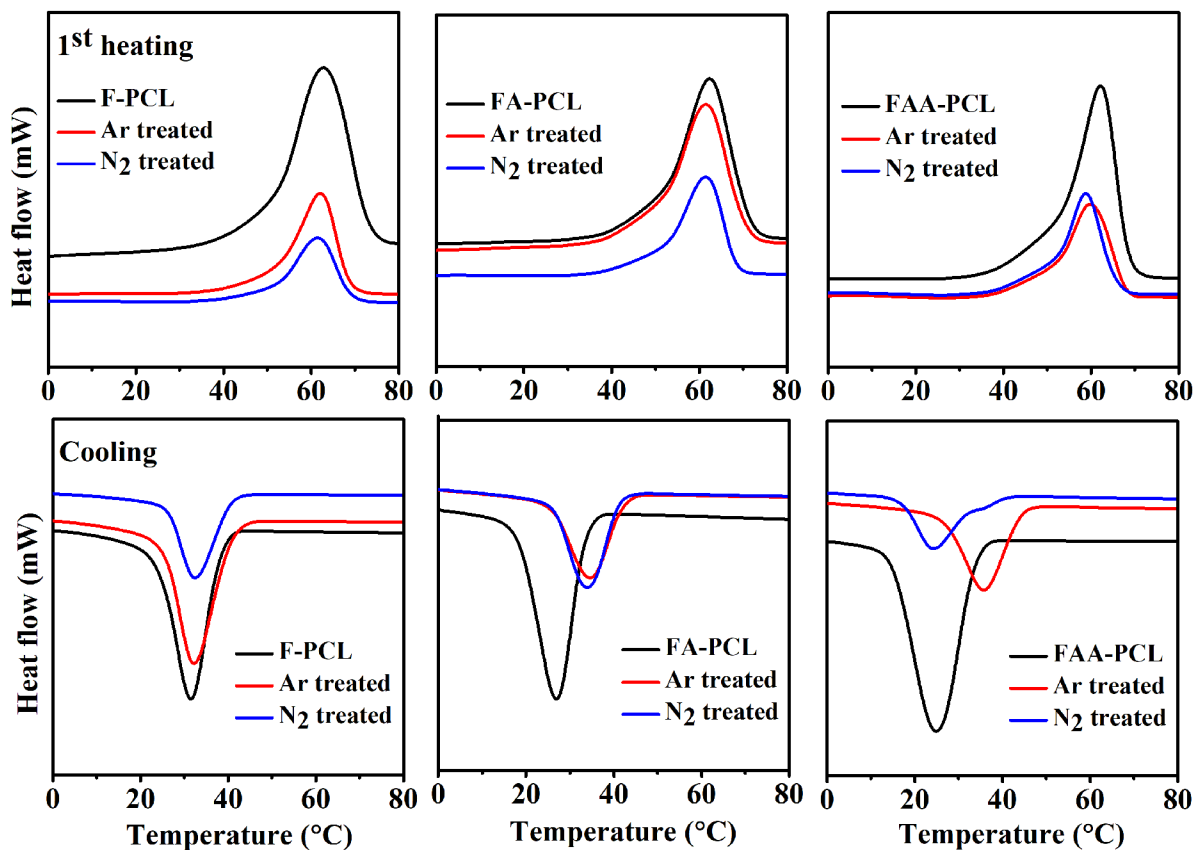


Figure 4.25: DSC curves of 1st heating and cooling scans for untreated and plasma-treated PCL ENMs.

The crystallization temperature (T_c) is directly related to the polymer molar mass [153]. Hence, it is interesting to note that the crystallization temperature of pristine F-PCL $32.9 \pm 0.2^\circ\text{C}$ is higher than the crystallization temperature of FA-PCL $25.2 \pm 2.9^\circ\text{C}$ and FAA-PCL $23.9 \pm 1.6^\circ\text{C}$ which can be attributed to hydrolytic degradation during the dissolution of PCL pellets in formic and acetic acid [90, 107, 154]. Indeed, an increase in T_c is also noticed in other studies due to enhanced mobility of shorter polymer chains in the hydrolytic solvent system, which in turn increases the degree of crystallinity and T_c [106]. Fig. 4.25 and Table 4.8 also reveal that the performed plasma treatments increase the T_c of F-PCL from $32.9 \pm 0.2^\circ\text{C}$ for the untreated sample to $33.5 \pm 0.3^\circ\text{C}$ and $33.9 \pm 0.2^\circ\text{C}$ for argon and nitrogen plasma-treated F-PCL respectively. Similar, even more pronounced increases in T_c values after plasma treatment are also observed for the FA-PCL samples. In the case of FAA-PCL, the argon plasma-treated sample is found to possess a higher T_c value: $33.9 \pm 0.9^\circ\text{C}$ versus $23.9 \pm 1.6^\circ\text{C}$ for untreated FAA-PCL.

On the other hand, nitrogen plasma-treated FAA-PCL shows one distinct crystallization peak at $23.4 \pm 0.4^\circ\text{C}$ and a small peak at $34.2 \pm 0.2^\circ\text{C}$ due to the presence of various crystals with different modes of assembly of macromolecular chains formed during cooling [146]. The increases in T_c observed on the plasma-treated samples are in agreement with other reports [147]. It is believed that the new functional groups generated by plasma treatment act as nucleating sites, apparently leading to a higher nuclei density. This higher nuclei density may in turn lead to a crystallization process at higher temperatures [145–149, 155]. Ivanova *et al.* reported that nucleation is directly proportional to the type and number of active groups on plasma-treated PCL ENMs [148].

From the DSC thermographs shown in Fig. 4.25, the crystallinity (X_c) can also be determined using Eq 3.10 on page 52 and the calculated values are presented in Table 4.8. It was found that the degree of crystallinity values of pristine F-PCL, FA-PCL, and FAA-PCL are $57.7 \pm 1.7\%$, $55.8 \pm 0.7\%$, and $53.9 \pm 0.9\%$ respectively. The reason for the higher degree of crystallinity of F-PCL and FA-PCL in comparison to FAA-PCL might be caused by the following factors: (i) the formic acid and acetic acid solvent system promotes the cleavage of the ester bonds (acid-catalyzed scission), which results in a low viscosity (Fig. 4.5 on page 63) due to a loss of molar mass [90, 107, 154]; (ii) shorter molecular chains have a higher mobility rate than longer polymeric chains [106]; and (iii) due to the slow evaporation rate of the F and FA solvent system, PCL molecular chains have enough time to rearrange themselves thereby increasing the crystallization process [106, 141].

It can also be observed from Table 4.8 that the conducted plasma treatments do not significantly affect the X_c value of F-PCL and FAA-PCL ENMs. On the other hand, in the case of FA-PCL ENMs, both investigated plasma treatments slightly increase the X_c value. Considering the crystallinity degree obtained from DSC and FTIR, it can thus be concluded that conducted plasma treatment do not significantly influence the crystallinity degree of PCL ENMs. A linear relationship was obtained between X_c and χ_c (Fig. A.4). The DSC analysis thus generally conformed the FTIR data, although some minor differences in absolute values could be observed (for example, X_c is larger than χ_c). These small differences might be caused by the different sampling areas and depth of analysis of both techniques [148]. Moreover, crystallization is a thermally-induced process in DSC. In general, the conducted plasma treatments do not affect the crystallinity degree of the PCL ENMs. In contrast, the crystal size, crystallization temperature, and melting temperature are for some PCL ENMs affected by the performed plasma treatments.

Chapter 5

Conclusions

Most researchers have been using the DC high-voltage in the electrospinning process, which means that a constant high voltage is delivered to the spinning electrode to produce the electrospun fibers. However, Until now, very few studies on the utilization of AC high voltage in the electrospinning process. When AC high voltage is used, the voltage can be supplied to the spinneret in various waveforms and frequencies. As a result, better control over the delivery of the electric charges to the spinning solution. In addition, AC electrospinning does not require an electrically active collector for collecting the electrospun fibers. Therefore, the main goal of this PhD dissertation was to study the impacts of AC high voltage on the spinnability of PCL electrospun nanofibers. In addition, plasma surface treatment effects on the PCL ENFs's bulk properties were also studied. To do so, a series of objectives and hypotheses were constructed (Chapter 1).

The first experimental part (sub-chapter 4.1) of the thesis was dedicated to studying the impacts that various less-toxic solvents and applied AC-potential have on PCL's spinnability, morphology, and productivity. The polymer-solvent interaction parameters and GPC results revealed that the formic acid/acetic acid/acetone (FAA) solvent system was a stable and better solvent system for PCL than the formic acid/acetic acid (FA) and the formic acid (F) since the acid-catalyzed degradation of ester bonds was substantially reduced in the former solvent system. In contrast, F and FA were the hydrolytic acids, which reduced the molecular weight of PCL during the dissolution as well as while storing the precursor solution. In addition, viscosity results also confirmed these findings. Interestingly, the used solvent system significantly impacts the critical polymer concentration for the stable AC electrospinnability. For instance, 10 and 15 wt% of F-PCL and FA-PCL produced the electrospun fibers at AC high voltage of 25 and 32 kV_{RMS}, whereas electrospinning was not possible at 5 and 20 wt%. In contrast, 5 and 10 wt%

of FAA–PCL were AC spinnable at 25 and 32 kV_{RMS} ; at the same time, 15 and 20 wt% impeded the electrospinning process. A linear relationship was observed between polymer concentration and fiber diameter, applied AC high voltage and fiber diameter, as well as applied AC high voltage and productivity of PCL ENS. At any constant concentration of PCL, owing to the PCL stability in the FAA solvent system, FAA–PCL reflects higher fiber diameter and higher productivity of PCL ENS followed by FA–PCL and F–PCL. Also, when increasing the applied AC high voltage from 25 to 32 kV_{RMS} , the productivity of ENS increased from $(1.1 \pm 0.1$ to $2.2 \pm 0.2)$ g/h, $(2.9 \pm 0.1$ to $6.9 \pm 0.1)$ g/h, and $(5.7 \pm 0.2$ to $12.4 \pm 0.3)$ g/h for F–PCL, FA–PCL, and FAA–PCL, respectively. The *in vitro* experiment showed that all PCL ENS are noncytotoxic and biocompatible materials. Higher cell viability was detected on day seven on F–PCL, followed by FAA–PCL and FA–PCL ENS. The cytotoxicity and *in vitro* results thus confirmed that the fabricated ENS could be used as a biomaterial in various biomedical and tissue engineering fields. In summary, FAA is a better solvent system than FA and F in terms of PCL’s stability and higher throughput of PCL ENS. Also, the obtained results support the hypothesis: the carboxylic acids could be used as a solvent system for improving the AC spinnability of PCL rather than common highly toxic organic solvents.

The second experimental part (sub–chapter 4.2) was dedicated to studying the impacts of the various waveforms and frequencies of AC high–voltage signals on the spinnability, morphology, fiber diameter, and productivity of PCL ENF. This study hypothesized that the waveform and/or applied frequency of AC high–voltage signal are able to affect the electrification of the liquid, jet initiation and termination, the length of the charged segments, the whipping instability, and the formation of a virtual collector. Thus the waveform and frequency of AC high–voltage signal can be used as new technological parameters for controlling the AC spinnability of polymers. The obtained results revealed that the waveform and the frequency comprise additional technological parameters with respect to the AC spinnability and the productivity of PCL ENF. The waveform strongly influences the formation of a stable fibrous plume. For example, the square and sine waveforms created plumes at 10 Hz. In contrast, the triangle waveform acted to inhibit spinnability at 10 Hz since it required more time to attain the critical voltage and the switching of the voltage polarity. The waveform exerts a significant impact on the morphological features of PCL ENF. In addition, various fiber diameter distributions were determined as a function of the waveform and applied frequency. The triangle and sine waveforms (with the exception of 50 and 30 Hz) can be used for the fabrication of smooth fibers without the presence of beads or spindles. The production of a trimodal fibrous morphology consisting of beads, spindle and helical fibers is possible via the application of the square waveform.

The minimum and maximum mean fiber diameters (0.34 ± 0.2 and 2.05 ± 1.9) μm were obtained for the square and triangle waveforms at 30 Hz and 60 Hz, respectively. Higher frequency waveforms encouraged the formation of thicker fibers. All the 50 Hz waveforms evinced the three-fold higher mass production of nanofibers than did lower frequencies (10 or 20 Hz). The square waveform exhibited the highest productivity (23.6 ± 0.4)g/h followed by the sine (16.5 ± 0.3)g/h and the triangle (6.9 ± 0.2)g/h waveforms at 50 Hz. In addition, the original chemical structure of the PCL was not influenced by either the waveform or the frequency. The square waveform at 50 Hz thus comprises a high throughput technological parameter concerning PCL.

The third experimental part (sub-chapter 4.3) was shifted towards the surface plasma treatment of PCL ENMs using a DBD reactor at medium pressure with various discharge gas (argon and nitrogen). Argon and nitrogen plasma treatments effects on wettability, morphology, surface functional groups, crystallite size, and crystallinity of F-PCL, FA-PCL, and FAA-PCL ENMs were investigated for the first time. Argon and nitrogen DBD plasma treatments were observed to incorporate polar oxygen- or nitrogen-containing functional groups on the ENM surfaces respectively without modifying the morphological properties of the PCL samples. This functional group grafting in turn resulted into a significant increase in the surface wettability of F-PCL, FA-PCL, and FAA-PCL ENMs with WCA values decreasing from $130^\circ - 136^\circ$ to $35^\circ - 48^\circ$ depending on the used discharge gas and solvent system. DSC and FTIR analysis also revealed that the crystallinity degree of PCL ENMs was not significantly affected (except for the X_c value of FA-PCL) by the performed plasma treatments. On the other hand, the crystallinity degree of the pristine PCL ENMs was influenced by the used solvent system. The F-PCL and FA-PCL crystallinity degree were higher than in the case of FAA-PCL due to the hydrolytic behavior of formic acid and acetic acid. The melting temperature of F-PCL and FA-PCL was not changed upon plasma treatment nor by the used solvent system which could be attributed to the unchanged crystallite size. In contrast, the melting temperature of FAA-PCL was slightly altered by the performed plasma treatments due to an increasing crystallite size. The gathered results thus reveal that the performed plasma treatments can strongly enhance the surface wettability of PCL ENMs without strongly affecting their bulk properties.

5.1 Significant output from the research and future work

Since traditionally used organic solvents in DC electrospinning for the fabrication of PCL nanofibers were unable to create the electrospun nanofibers from AC electrospinning, this study finds various the alternative solvent systems for PCL. Attaining a high PCL ENF production rate as a function of the waveform and frequency of the AC high-voltage signal represents a significant breakthrough in the field of electrospinning technology and the attainment of various fiber morphologies and fiber diameter distributions comprised additional advantages.

It is pleasing to say that for the first time, this work has introduced a new technological parameter for controlling the electrospun fiber morphology and productivity using free surface AC electrospinning. Furthermore, this paper will inspire the academic and industrial communities to fabricate the various polymeric electrospun nanofibers as well as composite nanofibrous yarns on an industrial scale using the collector less AC electrospinning technique. Also, this study has shown that plasma treatment did not impact the crystallinity degree and crystal size of PCL electrospun nanofibers.

The author believes that in the near future, AC high voltage will be used as a power source for electrospinning technology by the academic and industrial communities to fabricate multi-dimensional electrospun nanofiber-based materials, i.e., composite yarns, nanofiber coated surgical sutures, nanofiber coated dental flosses and bulky nanofibrous materials.

The study presented herein will be extended in the future so as to include the study of the physical principles which govern the onset of AC electrospinning and the effects of the waveform and frequency on the physico-chemical and mechanical properties of PCL ENF.

Appendix A

First Appendix

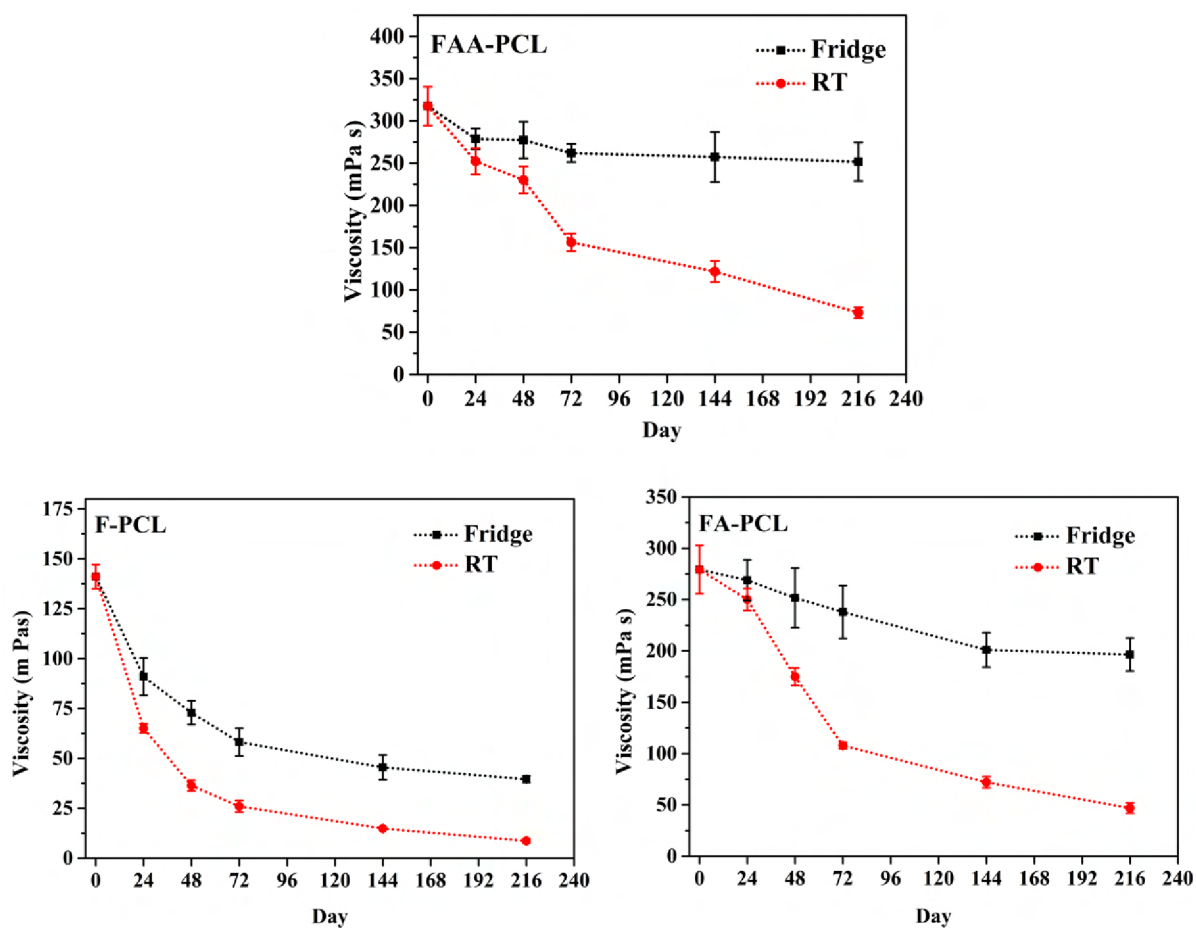


Figure A.1: Viscosity of various PCL solution as a function of storage condition and time.

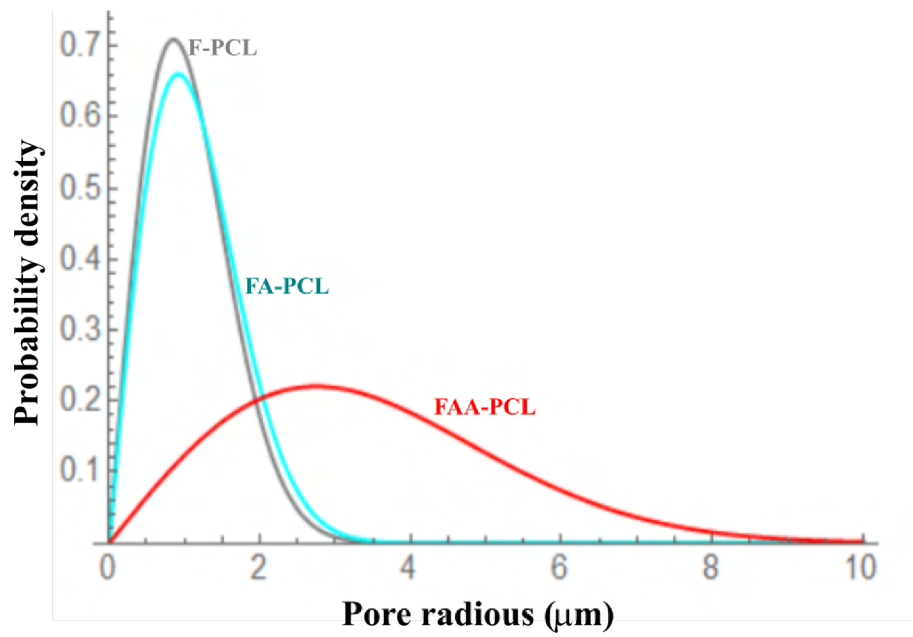


Figure A.2: Pore radius distribution probability.

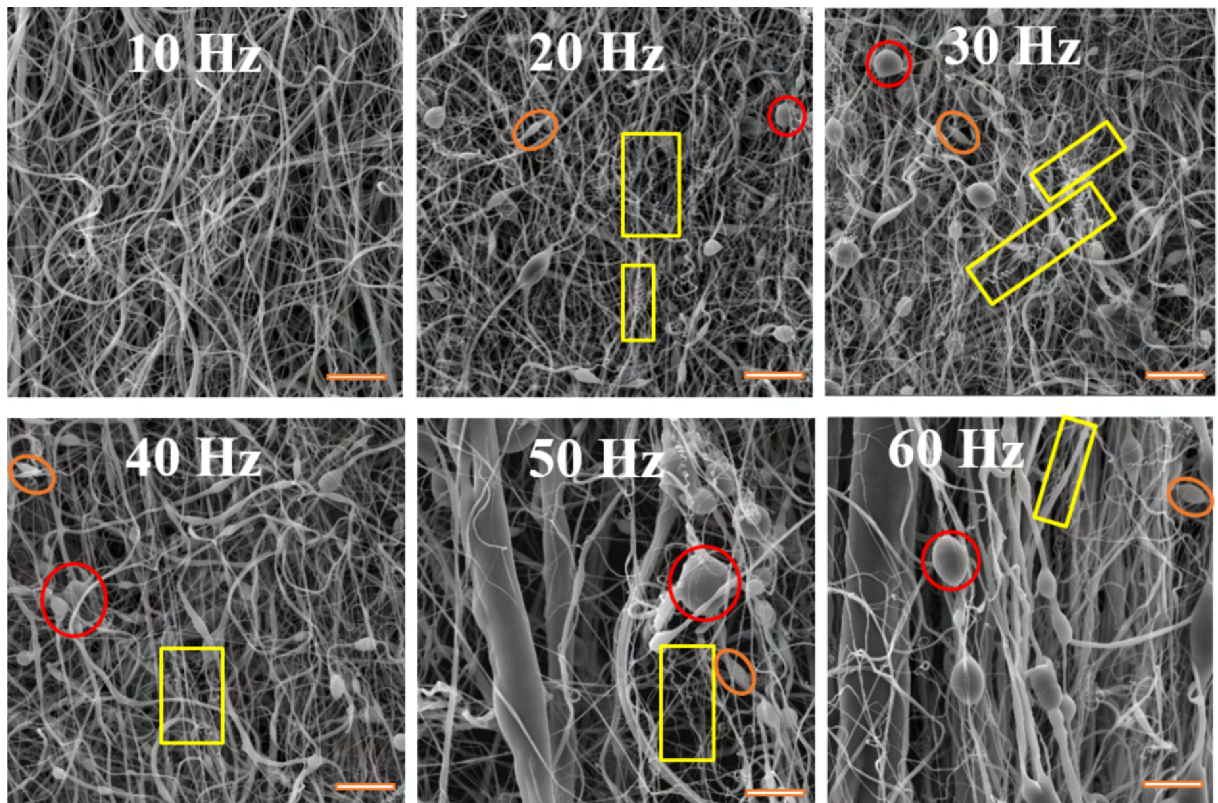


Figure A.3: SEM images of PCL ENF as a function of the square waveform's various frequencies (beads, spindles, and helical structures are highlighted in red, orange, and yellow, respectively).

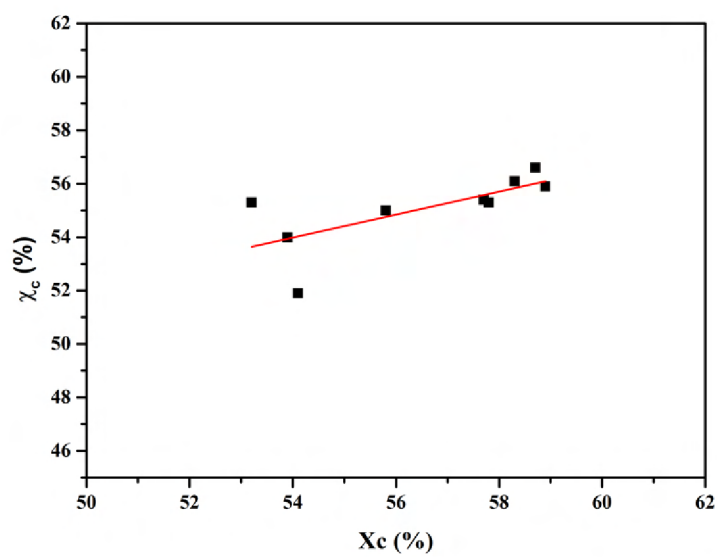


Figure A.4: A linear relationship between χ_c and X_c

Bibliography

- [1] James M Adovasio, Olga Soffer, and Bohuslav Klima. Upper palaeolithic fibre technology: interlaced woven finds from pavlov i, czech republic, c. 26,000 years ago. *Antiquity*, 70(269):526–534, 1996.
- [2] Jiří Svoboda, Miroslav Králík, Věra Čulíková, Šárka Hladilová, Martin Novák, Miriam Nývltová Fišáková, Daniel Nývlt, and Michaela Zelinková. Pavlov vi: an upper palaeolithic living unit. *Antiquity*, 83(320):282–295, 2009.
- [3] Oldrich Jirsak, Filip Sanetrnik, David Lukas, Vaclav Kotek, Lenka Martinova, and Jiri Chaloupek. Method of nanofibres production from a polymer solution using electrostatic spinning and a device for carrying out the method, September 8 2009. US Patent 7,585,437.
- [4] Jaroslav Beran, Jan Valtera, Martin BILEK, Josef SKRIVANEK, Ondrej BATKA, David Lukas, Pavel Pokorny, Tomas KALOUS, Julie SOUKUPOVA, Eva Kostakova, et al. Method for producing polymeric nanofibers by electrospinning a polymer solution or melt, a spinning electrode for performing the method and a device for producing polymeric nanofibers equipped with at least one such spinning electrode, 2017.
- [5] Lubomir Kocis, Pavel Pokorny, David Lukas, Petr Mikes, Jiri Chvojka, Eva Kostakova, Jaroslav Beran, Martin Bilek, Jan Valtera, Evzen Amler, et al. Method for production of polymeric nanofibers by spinning of solution or melt of polymer in electric field, August 7 2018. US Patent 10,041,189.
- [6] Jaroslav Beran, Jan Valtera, Martin Bilek, Ondrej Batka, Josef Skrivanek, Petr Zabka, Jiri Komarek, David Lukas, Pavel Pokorny, Eva Kuzelova-Kostakova, et al. Linear fibrous formation with a coating of polymeric nanofibers enveloping a supporting linear formation constituting a core, a method and a device for producing it, February 23 2021. US Patent 10,927,480.

- [7] Jaroslav Beran, David Lukas, Pavel Pokorný, Tomas Kalous, and Jan Valtera. Method for producing polymeric nanofibres by electric or electrostatic spinning of a polymer solution or melt, a spinning electrode for the method, and a device for the production of polymeric nanofibres equipped with at least one such spinning electrode, October 26 2021. US Patent 11,155,934.
- [8] Darrell H Reneker, Alexander L Yarin, Hao Fong, and Sureeporn Koombhongse. Bending instability of electrically charged liquid jets of polymer solutions in electrospinning. *Journal of Applied physics*, 87(9):4531–4547, 2000.
- [9] Alexander L Yarin, Sureeporn Koombhongse, and Darrell Hyson Reneker. Bending instability in electrospinning of nanofibers. *Journal of applied physics*, 89(5):3018–3026, 2001.
- [10] George Collins, John Federici, Yuki Imura, and Luiz H Catalani. Charge generation, charge transport, and residual charge in the electrospinning of polymers: A review of issues and complications. *Journal of Applied Physics*, 111(4):044701, 2012.
- [11] Adel Mohammed Al-Dhahebi, JinKiong Ling, Syam G Krishnan, Maryam Yousefzadeh, Naveen Kumar Elumalai, Mohamed Shuaib Mohamed Saheed, Seeram Ramakrishna, and Rajan Jose. Electrospinning research and products: The road and the way forward. *Applied Physics Reviews*, 9(1):011319, 2022.
- [12] Ziqian Liu, Seeram Ramakrishna, and Xiaoling Liu. Electrospinning and emerging healthcare and medicine possibilities. *APL bioengineering*, 4(3):030901, 2020.
- [13] Brabu Balusamy, Omer Faruk Sarioglu, Anitha Senthamizhan, and Tamer Uyar. Rational design and development of electrospun nanofibrous biohybrid composites. *ACS Applied Bio Materials*, 2(8):3128–3143, 2019.
- [14] Kanakaraj Aruchamy, Ashesh Mahto, and SK Nataraj. Electrospun nanofibers, nanocomposites and characterization of art: Insight on establishing fibers as product. *Nano-Structures & Nano-Objects*, 16:45–58, 2018.
- [15] Jie Liang, Haitao Zhao, Luchao Yue, Guangyin Fan, Tingshuai Li, Siyu Lu, Guang Chen, Shuyan Gao, Abdullah M Asiri, and Xuping Sun. Recent advances in electrospun nanofibers for supercapacitors. *Journal of Materials Chemistry A*, 8(33):16747–16789, 2020.
- [16] Fatma Yener and Oldřich Jirsák. Comparison between the needle and roller electrospinning of polyvinylbutyral. *Journal of Nanomaterials*, 2012, 2012.

- [17] Hanna Sofia SalehHudin, Edzrol Niza Mohamad, Wan Nor Liza Mahadi, and Amlina Muhammad Affi. Multiple-jet electrospinning methods for nanofiber processing: A review. *Materials and Manufacturing Processes*, 33(5):479–498, 2018.
- [18] Nandana Bhardwaj and Subhas C Kundu. Electrospinning: a fascinating fiber fabrication technique. *Biotechnology advances*, 28(3):325–347, 2010.
- [19] Royal Kessick, John Fenn, and Gary Tepper. The use of ac potentials in electro-spraying and electrospinning processes. *Polymer*, 45(9):2981–2984, 2004.
- [20] Manikandan Sivan, Divyabharathi Madheswaran, Jan Valtera, Eva Kuzelova Kostakova, and David Lukas. Alternating current electrospinning: The impacts of various high-voltage signal shapes and frequencies on the spinnability and productivity of polycaprolactone nanofibers. *Materials & Design*, 213:110308, 2022.
- [21] Divyabharathi Madheswaran, Manikandan Sivan, Jan Valtera, Eva Kuzelova Kostakova, Tim Egghe, Mahtab Asadian, Vit Novotny, Nhung HA Nguyen, Alena Sevcu, Rino Morent, et al. Composite yarns with antibacterial nanofibrous sheaths produced by collectorless alternating-current electrospinning for suture applications. *Journal of Applied Polymer Science*, 139(13):51851, 2022.
- [22] Manikandan Sivan, Divyabharathi Madheswaran, Mahtab Asadian, Pieter Cools, Monica Thukkaram, Pascal Van Der Voort, Rino Morent, Nathalie De Geyter, and David Lukas. Plasma treatment effects on bulk properties of polycaprolactone nanofibrous mats fabricated by uncommon ac electrospinning: A comparative study. *Surface and Coatings Technology*, 399:126203, 2020.
- [23] Pavel Pokorny, E Kostakova, Filip Sanetnik, Petr Mikes, Jiri Chvojka, Tomas Kalous, Martin Bilek, Karel Pejchar, Jan Valtera, and David Lukas. Effective ac needleless and collectorless electrospinning for yarn production. *Physical Chemistry Chemical Physics*, 16(48):26816–26822, 2014.
- [24] Jan Valtera, Tomas Kalous, Pavel Pokorny, Ondrej Batka, Martin Bilek, Jiri Chvojka, Petr Mikes, Eva Kuzelova Kostakova, Petr Zabka, Jana Ornstova, et al. Fabrication of dual-functional composite yarns with a nanofibrous envelope using high throughput ac needleless and collectorless electrospinning. *Scientific reports*, 9(1): 1–10, 2019.
- [25] Balázs Farkas, Attila Balogh, Attila Farkas, György Marosi, and Zsombor Kristóf Nagy. Frequency and waveform dependence of alternating current electrospinning and their uses for drug dissolution enhancement. *International Journal of Pharmaceutics*, 586:119593, 2020.

- [26] Siddharth Maheshwari and Hsueh-Chia Chang. Assembly of multi-stranded nanofiber threads through ac electrospinning. *Advanced Materials*, 21(3):349–354, 2009.
- [27] Tomas Kalous, Pavel Holec, Jakub Erben, Martin Bilek, Ondrej Batka, Pavel Pokorný, Jiri Chaloupek, and Jiri Chvojka. The optimization of alternating current electrospun pa 6 solutions using a visual analysis system. *Polymers*, 13(13):2098, 2021.
- [28] Radek Jirkovec, Tomas Kalous, and Jiri Chvojka. The modification of the wetting of polycaprolactone nanofibre layers via alternating current spinning. *Materials & Design*, 210:110096, 2021.
- [29] Siddharth Maheshwari and Hsueh-Chia Chang. Effects of bulk charge and momentum relaxation time scales on ac electrospinning. *Journal of applied physics*, 102(3):034902, 2007.
- [30] M Sivan, D Madheswaran, S Hauzerova, V Novotny, V Hedvicakova, V Jencova, EK Kostakova, M Schindler, and D Lukas. Ac electrospinning: impact of high voltage and solvent on the electrospinnability and productivity of polycaprolactone electrospun nanofibrous scaffolds. *Materials Today Chemistry*, 26:101025, 2022.
- [31] Radek Jirkovec, Alzbeta Samkova, Tomas Kalous, Jiri Chaloupek, and Jiri Chvojka. Preparation of a hydrogel nanofiber wound dressing. *Nanomaterials*, 11(9):2178, 2021.
- [32] Balázs Farkas, Attila Balogh, Richárd Cselkó, Kolos Molnár, Attila Farkas, Enikő Borbás, György Marosi, and Zsombor Kristóf Nagy. Corona alternating current electrospinning: A combined approach for increasing the productivity of electrospinning. *International journal of pharmaceutics*, 561:219–227, 2019.
- [33] S Anju, N Prajitha, VS Sukanya, and PV Mohanan. Complicity of degradable polymers in health-care applications. *Materials Today Chemistry*, 16:100236, 2020.
- [34] Maria Ann Woodruff and Dietmar Werner Hutmacher. The return of a forgotten polymer—polycaprolactone in the 21st century. *Progress in polymer science*, 35(10):1217–1256, 2010.
- [35] Orawan Suwantong. Biomedical applications of electrospun polycaprolactone fiber mats. *Polymers for Advanced Technologies*, 27(10):1264–1273, 2016.
- [36] I Shepa, E Mudra, and J Dusza. Electrospinning through the prism of time. *Materials Today Chemistry*, 21:100543, 2021.

- [37] Shanta Raj Bhattarai, Narayan Bhattarai, Ho Keun Yi, Pyong Han Hwang, Dong Il Cha, and Hak Yong Kim. Novel biodegradable electrospun membrane: scaffold for tissue engineering. *Biomaterials*, 25(13):2595–2602, 2004.
- [38] Council of Europe. European Department for the Quality of Medicines and European Directorate for the Quality of Medicines & Healthcare. *European Pharmacopoeia: Published in Accordance with the Convention on the Elaboration of a European Pharmacopoeia (European Treaty Series No. 50)*, volume 8. Council of Europe, 2013.
- [39] Albino Martins, Elisabete D Pinho, Susana Faria, Iva Pashkuleva, Alexandra P Marques, Rui L Reis, and Nuno M Neves. Surface modification of electrospun polycaprolactone nanofiber meshes by plasma treatment to enhance biological performance. *small*, 5(10):1195–1206, 2009.
- [40] Mahtab Asadian. *Plasma treatment of nanofibrous meshes for tissue engineering applications*. PhD thesis, Ghent University, 2019.
- [41] Sharmila M Mukhopadhyay, Pratik Joshi, S Datta, and J Macdaniel. Plasma assisted surface coating of porous solids. *Applied Surface Science*, 201(1-4):219–226, 2002.
- [42] Rino Morent, Nathalie De Geyter, Christophe Leys, L Gengembre, and E Payen. Comparison between xps-and ftir-analysis of plasma-treated polypropylene film surfaces. *Surface and Interface Analysis: An International Journal devoted to the development and application of techniques for the analysis of surfaces, interfaces and thin films*, 40(3-4):597–600, 2008.
- [43] Alexandra Løvdaal, Jakob Vange, Lene Feldskov Nielsen, and Kristoffer Almdal. Mechanical properties of electrospun pcl scaffold under in vitro and accelerated degradation conditions. *Biomedical Engineering: Applications, Basis and Communications*, 26(03):1450043, 2014.
- [44] Lord Rayleigh. Xx. on the equilibrium of liquid conducting masses charged with electricity. *The London, Edinburgh, and Dublin Philosophical Magazine and Journal of Science*, 14(87):184–186, 1882.
- [45] Charles Vernon Boys. On the production, properties, and some suggested uses of the finest threads. *Proceedings of the Physical Society of London (1874-1925)*, 9(1): 8, 1887.

- [46] Yuris Dzenis. Spinning continuous fibers for nanotechnology. *Science*, 304(5679):1917–1919, 2004.
- [47] John F Cooley. Apparatus for electrically dispersing fluids., February 4 1902. US Patent 692,631.
- [48] William James Morton. Method of dispersing fluids., July 29 1902. US Patent 705,691.
- [49] John Zeleny. The electrical discharge from liquid points, and a hydrostatic method of measuring the electric intensity at their surfaces. *Physical Review*, 3(2):69, 1914.
- [50] Formhals Anton. Process and apparatus for preparing artificial threads, October 2 1934. US Patent 1,975,504.
- [51] Geoffrey Ingram Taylor. Electrically driven jets. *Proceedings of the Royal Society of London. A. Mathematical and Physical Sciences*, 313(1515):453–475, 1969.
- [52] Darrell H Reneker and Hao Fong. Polymeric nanofibers: introduction. ACS Publications, 2006.
- [53] YM Shin, MM Hohman, Michael P Brenner, and GC Rutledge. Electrospinning: A whipping fluid jet generates submicron polymer fibers. *Applied physics letters*, 78(8):1149–1151, 2001.
- [54] Caitlin Lawson, Andrei Stanishevsky, Manikandan Sivan, Pavel Pokorny, and David Lukáš. Rapid fabrication of poly (ϵ -caprolactone) nanofibers using needleless alternating current electrospinning. *Journal of Applied Polymer Science*, 133(13), 2016.
- [55] Pavel Holec, Radek Jirkovec, Tomáš Kalous, Ondřej Bat’ka, Jiří Brožek, and Jiří Chvojka. The potential for the direct and alternating current-driven electrospinning of polyamides. *Nanomaterials*, 12(4):665, 2022.
- [56] Radek Jirkovec, Tomas Kalous, W Anthony Brayer, Andrei V Stanishevky, and Jiri Chvojka. Production of gelatin nanofibrous layers via alternating current electrospinning. *Materials Letters*, 252:186–190, 2019.
- [57] Amanda Kennell, Mark MacEwen, Micah Armstrong, Teodora Nicola, Brian Haloran, Namasivayam Ambalavanan, and Andrei Stanishevsky. Fish skin gelatin nanofibrous scaffolds spun using alternating field electrospinning and in-vitro tested with tdtomato mice fibroblasts. *Materials Today Communications*, 31:103417, 2022.

- [58] Andrei Stanishevsky, Courtney Severino, Stacy Ross, Riley Yager, Micah Armstrong, Michał Binczarski, Waldemar Maniukiewicz, and Izabela Witońska. Nanofibrous glass/ceramic porous structures using high-temperature interface bonding. *Materials Today Communications*, 27:102218, 2021.
- [59] Andrei Stanishevsky, W Anthony Brayer, Pavel Pokorny, Tomáš Kalous, and David Lukáš. Nanofibrous alumina structures fabricated using high-yield alternating current electrospinning. *Ceramics International*, 42(15):17154–17161, 2016.
- [60] Jakub Erben, Tomas Kalous, and Jiri Chvojka. Ac bubble electrospinning technology for preparation of nanofibrous mats. *ACS omega*, 5(14):8268–8271, 2020.
- [61] Siddharth Maheshwari and Hsueh-Chia Chang. Anomalous conical menisci under an ac field-departure from the dc taylor cone. *Applied physics letters*, 89(23):234103, 2006.
- [62] Alexander L Yarin, Sureeporn Koombhongse, and Darrell Hyson Reneker. Taylor cone and jetting from liquid droplets in electrospinning of nanofibers. *Journal of applied physics*, 90(9):4836–4846, 2001.
- [63] Karel Havlíček, Lucie Svobodová, Totka Bakalova, and Tomáš Lederer. Influence of electrospinning methods on characteristics of polyvinyl butyral and polyurethane nanofibres essential for biological applications. *Materials & Design*, 194:108898, 2020.
- [64] A Vaseashta. Controlled formation of multiple taylor cones in electrospinning process. *Applied Physics Letters*, 90(9):093115, 2007.
- [65] David Lukas, Arindam Sarkar, and Pavel Pokorny. Self-organization of jets in electrospinning from free liquid surface: A generalized approach. *Journal of Applied Physics*, 103(8):084309, 2008.
- [66] David Lukáš, A Sarkar, L Martinova, K Vodsed'álková, D Lubasová, J Chaloupek, P Pokorný, P Mikeš, J Chvojka, and M Komárek. Physical principles of electrospinning (electrospinning as a nano-scale technology of the twenty-first century). *Textile progress*, 41(2):59–140, 2009.
- [67] SN Reznik, AL Yarin, A Theron, and E Zussman. Transient and steady shapes of droplets attached to a surface in a strong electric field. *Journal of Fluid Mechanics*, 516:349–377, 2004.

-
- [68] Jiajia Xue, Tong Wu, Yunqian Dai, and Younan Xia. Electrospinning and electrospun nanofibers: Methods, materials, and applications. *Chemical reviews*, 119(8):5298–5415, 2019.
- [69] Ji-Huan He, Yue Wu, and Wei-Wei Zuo. Critical length of straight jet in electrospinning. *Polymer*, 46(26):12637–12640, 2005.
- [70] W Jones. Earnshaw’s theorem and the stability of matter. *European Journal of Physics*, 1(2):85, 1980.
- [71] Jayesh Doshi and Darrell H Reneker. Electrospinning process and applications of electrospun fibers. *Journal of electrostatics*, 35(2-3):151–160, 1995.
- [72] Xiang-Fa Wu, Yury Salkovskiy, and Yuris A Dzenis. Modeling of solvent evaporation from polymer jets in electrospinning. *Applied Physics Letters*, 98(22):223108, 2011.
- [73] Goki Eda, James Liu, and Satya Shivkumar. Solvent effects on jet evolution during electrospinning of semi-dilute polystyrene solutions. *European polymer journal*, 43(4):1154–1167, 2007.
- [74] Martin Urbanski, Catherine G Reyes, JungHyun Noh, Anshul Sharma, Yong Geng, Venkata Subba Rao Jampani, and Jan PF Lagerwall. Liquid crystals in micron-scale droplets, shells and fibers. *Journal of Physics: Condensed Matter*, 29(13):133003, 2017.
- [75] Andreas Greiner and Joachim H Wendorff. Electrospinning: a fascinating method for the preparation of ultrathin fibers. *Angewandte Chemie International Edition*, 46(30):5670–5703, 2007.
- [76] Soumayajit Sarkar, Seetharama Deevi, and Gary Tepper. Biased ac electrospinning of aligned polymer nanofibers. *Macromolecular rapid communications*, 28(9):1034–1039, 2007.
- [77] Radek Jirkovec, Jakub Erben, Petr Sajdl, Jiri Chaloupek, and Jiri Chvojka. The effect of material and process parameters on the surface energy of polycaprolactone fibre layers. *Materials & Design*, 205:109748, 2021.
- [78] Tomas Kalous, Pavel Holec, Radek Jirkovec, David Lukas, and Jiri Chvojka. Improved spinnability of pa 6 solutions using ac electrospinning. *Materials Letters*, 283:128761, 2021.

- [79] Sarah L Nealy, Courtney Severino, W Anthony Brayer, and Andrei Stanishevsky. Nanofibrous tio 2 produced using alternating field electrospinning of titanium alkoxide precursors: crystallization and phase development. *RSC advances*, 10(12):6840–6849, 2020.
- [80] Andrei Stanishevsky, Riley Yager, Jolanta Tomaszewska, Michał Binczarski, Waldemar Maniukiewicz, Izabela Witońska, and David Lukas. Structure and mechanical properties of nanofibrous zro2 derived from alternating field electrospun precursors. *Ceramics International*, 45(15):18672–18682, 2019.
- [81] Andrei Stanishevsky and Justin Tchernov. Mechanical and transport properties of fibrous amorphous silica meshes and membranes fabricated from compressed electrospun precursor fibers. *Journal of Non-Crystalline Solids*, 525:119653, 2019.
- [82] Nathalie De Geyter, Rino Morent, Tim Desmet, Martine Trentesaux, Léon Gengembre, Peter Dubruel, Christophe Leys, and Edmond Payen. Plasma modification of polylactic acid in a medium pressure dbd. *Surface and Coatings Technology*, 204(20):3272–3279, 2010.
- [83] Young Il Yoon, Hyun Sik Moon, Won Seok Lyoo, Taek Seung Lee, and Won Ho Park. Superhydrophobicity of cellulose triacetate fibrous mats produced by electrospinning and plasma treatment. *Carbohydrate polymers*, 75(2):246–250, 2009.
- [84] Ita Junkar, Uroš Cvelbar, Alenka Vesel, Nina Hauptman, and Miran Mozetič. The role of crystallinity on polymer interaction with oxygen plasma. *Plasma Processes and Polymers*, 6(10):667–675, 2009.
- [85] Rouba Ghobeira, Charlot Philips, Heidi Declercq, Pieter Cools, Nathalie De Geyter, Ria Cornelissen, and Rino Morent. Effects of different sterilization methods on the physico-chemical and bioresponsive properties of plasma-treated polycaprolactone films. *Biomedical Materials*, 12(1):015017, 2017.
- [86] Kwang Soo Kim, Chang Mo Ryu, Chan Sup Park, Gil Soo Sur, and Chan Eon Park. Investigation of crystallinity effects on the surface of oxygen plasma treated low density polyethylene using x-ray photoelectron spectroscopy. *Polymer*, 44(20):6287–6295, 2003.
- [87] Helen Cui and Patrick J Sinko. The role of crystallinity on differential attachment/proliferation of osteoblasts and fibroblasts on poly (caprolactone-co-glycolide) polymeric surfaces. *Frontiers of Materials Science*, 6(1):47–59, 2012.

- [88] Charles M Hansen. *Hansen solubility parameters: a user's handbook*. CRC press, 2007.
- [89] C Bordes, V Fréville, E Ruffin, P Marote, JY Gauvrit, S Briançon, and P Lantéri. Determination of poly (ϵ -caprolactone) solubility parameters: Application to solvent substitution in a microencapsulation process. *International journal of pharmaceuticals*, 383(1-2):236–243, 2010.
- [90] Rouba Ghobeira, Mahtab Asadian, Chris Vercruyse, Heidi Declercq, Nathalie De Geyter, and Rino Morent. Wide-ranging diameter scale of random and highly aligned pcl fibers electrospun using controlled working parameters. *Polymer*, 157: 19–31, 2018.
- [91] Pieter Cools, Nathalie De Geyter, Els Vanderleyden, Peter Dubruel, and Rino Morent. Surface analysis of titanium cleaning and activation processes: non-thermal plasma versus other techniques. *Plasma Chemistry and Plasma Processing*, 34(4): 917–932, 2014.
- [92] H-E Wagner, R Brandenburg, KV Kozlov, A Sonnenfeld, P Michel, and JF Behnke. The barrier discharge: basic properties and applications to surface treatment. *Vacuum*, 71(3):417–436, 2003.
- [93] J Masounave, AL Rollin, and R Denis. Prediction of permeability of non-woven geotextiles from morphometry analysis. *Journal of Microscopy*, 121(1):99–110, 1981.
- [94] RA Krasnoperov and D Stoyan. Second-order stereology of spatial fibre systems. *Journal of microscopy*, 216(2):156–164, 2004.
- [95] JM Haynes. Stereological analysis of pore structure. *Matériaux et Construction*, 6 (3):175–179, 1973.
- [96] John C Russ and Robert T Dehoff. *Practical stereology*. Springer Science & Business Media, 2012.
- [97] AL Patterson. The scherrer formula for x-ray particle size determination. *Physical review*, 56(10):978, 1939.
- [98] Daiwon Choi, Kacey G Marra, and Prashant N Kumta. Chemical synthesis of hydroxyapatite/poly (ϵ -caprolactone) composites. *Materials Research Bulletin*, 39 (3):417–432, 2004.
- [99] Ping Huang, Joseph X Zheng, Siwei Leng, Ryan M Van Horn, Kwang-Un Jeong, Ya Guo, Roderic P Quirk, Stephen ZD Cheng, Bernard Lotz, Edwin L Thomas, et al.

- Poly (ethylene oxide) crystal orientation changes in an inverse hexagonal cylindrical phase morphology constructed by a poly (ethylene oxide)-block-polystyrene diblock copolymer. *Macromolecules*, 40(3):526–534, 2007.
- [100] Eva Kuzelova Kostakova, Laszlo Meszaros, Gabriela Maskova, Lenka Blazkova, Tamas Turcsan, and David Lukas. Crystallinity of electrospun and centrifugal spun polycaprolactone fibers: a comparative study. *Journal of Nanomaterials*, 2017, 2017.
- [101] Eleftheria Antoniou and Paschalis Alexandridis. Polymer conformation in mixed aqueous-polar organic solvents. *European Polymer Journal*, 46(2):324–335, 2010.
- [102] Suzette M Aguilar, Jacob D Shea, Mudar A Al-Joumayly, Barry D Van Veen, Nader Behdad, and Susan C Hagness. Dielectric characterization of pcl-based thermoplastic materials for microwave diagnostic and therapeutic applications. *IEEE transactions on biomedical engineering*, 59(3):627–633, 2011.
- [103] CJ Luo, E Stride, and M Edirisinghe. Mapping the influence of solubility and dielectric constant on electrospinning polycaprolactone solutions. *Macromolecules*, 45(11):4669–4680, 2012.
- [104] Juan Pablo Perez Aguilera. Study and analysis of a polycaprolactone polymeric solution to produce a nanofibrous coating for medical stitching threads via electrospinning. Master’s thesis, Technical University of Liberec, 2020.
- [105] Kenta Odagiri and Kazuhiko Seki. Coil–globule transition of a polymer involved in excluded-volume interactions with macromolecules. *The Journal of Chemical Physics*, 143(13):10B606_1, 2015.
- [106] O Gil-Castell, JD Badia, Emma Strömberg, Sigbritt Karlsson, and A Ribes-Greus. Effect of the dissolution time into an acid hydrolytic solvent to tailor electrospun nanofibrous polycaprolactone scaffolds. *European Polymer Journal*, 87:174–187, 2017.
- [107] Nicolas Lavielle, Ana-Maria Popa, Matthijs de Geus, Anne Hébraud, Guy Schlatter, Linda Thöny-Meyer, and René M Rossi. Controlled formation of poly (ϵ -caprolactone) ultrathin electrospun nanofibers in a hydrolytic degradation-assisted process. *European Polymer Journal*, 49(6):1331–1336, 2013.
- [108] Xiaohong Qin and Dequn Wu. Effect of different solvents on poly (caprolactone)(pcl) electrospun nonwoven membranes. *Journal of thermal analysis and calorimetry*, 107(3):1007–1013, 2012.

- [109] Juliano Oliveira, Glaúcia Silveira Brichi, José Manoel Marconcini, Luiz Henrique Capparelli Mattoso, Gregory Melvin Glenn, and Eliton Souto Medeiros. Effect of solvent on the physical and morphological properties of poly (lactic acid) nanofibers obtained by solution blow spinning. *Journal of Engineered Fibers and Fabrics*, 9(4):155892501400900414, 2014.
- [110] Atsushi Nakano, Norihisa Miki, Koichi Hishida, and Atsushi Hotta. Solution parameters for the fabrication of thinner silicone fibers by electrospinning. *Physical Review E*, 86(1):011801, 2012.
- [111] Rita Kol, Tobias De Somer, Dagmar R D’hooge, Fabian Knappich, Kim Ragaert, Dimitris S Achilias, and Steven De Meester. State-of-the-art quantification of polymer solution viscosity for plastic waste recycling. *ChemSusChem*, 14(19):4071–4102, 2021.
- [112] CJ Luo, M Nangrejo, and M Edirisinghe. A novel method of selecting solvents for polymer electrospinning. *Polymer*, 51(7):1654–1662, 2010.
- [113] Suresh L Shenoy, W Douglas Bates, Harry L Frisch, and Gary E Wnek. Role of chain entanglements on fiber formation during electrospinning of polymer solutions: good solvent, non-specific polymer–polymer interaction limit. *Polymer*, 46(10):3372–3384, 2005.
- [114] Yunshen Cai and Michael Gevelber. The effect of relative humidity and evaporation rate on electrospinning: fiber diameter and measurement for control implications. *Journal of Materials Science*, 48(22):7812–7826, 2013.
- [115] Domitille Mailley, Anne Hebraud, and Guy Schlatter. A review on the impact of humidity during electrospinning: From the nanofiber structure engineering to the applications. *Macromolecular Materials and Engineering*, 306(7):2100115, 2021.
- [116] Koyal Garg and Gary L Bowlin. Electrospinning jets and nanofibrous structures. *Biomicrofluidics*, 5(1):013403, 2011.
- [117] Mohammad Yousef Younes, Hasan Al-aji, Mohammad Al-Bajhan, Ahmed Al-Saif, and Ali Al-Abdulaziz. Integration a design of experiment in the mass transfer laboratory to investigate the effect of temperature change on diffusion coefficient of acetone in air. *Integration*, 1(10):9–12, 2017.
- [118] LT Gibson, BG Cooksey, D Littlejohn, and NH Tennent. A diffusion tube sampler for the determination of acetic acid and formic acid vapours in museum cabinets. *Analytica Chimica Acta*, 341(1):11–19, 1997.

- [119] WILLIAM J LAUTENBERGER, ELBERT V KRING, and JOSEPH A MORELLO. A new personal badge monitor for organic vapors. *American Industrial Hygiene Association Journal*, 41(10):737–747, 1980.
- [120] Catalina Wong, Elisabeth Inman, Reiner Spaethe, and Sam Helgerson. Fibrin-based biomaterials to deliver human growth factors. *Thrombosis and haemostasis*, 89(03): 573–582, 2003.
- [121] Ming Chen, Prabir K Patra, Steven B Warner, and Sankha Bhowmick. Role of fiber diameter in adhesion and proliferation of nih 3t3 fibroblast on electrospun polycaprolactone scaffolds. *Tissue engineering*, 13(3):579–587, 2007.
- [122] Deok-Ho Kim, Paolo P Provenzano, Chris L Smith, and Andre Levchenko. Matrix nanotopography as a regulator of cell function. *Journal of Cell Biology*, 197(3): 351–360, 2012.
- [123] Joseph L Lowery, Neha Datta, and Gregory C Rutledge. Effect of fiber diameter, pore size and seeding method on growth of human dermal fibroblasts in electrospun poly (-caprolactone) fibrous mats. *Biomaterials*, 31(3):491–504, 2010.
- [124] Haijun He, Yimeng Wang, Balazs Farkas, Zsombor Kristof Nagy, and Kolos Molnar. Analysis and prediction of the diameter and orientation of ac electrospun nanofibers by response surface methodology. *Materials & Design*, 194:108902, 2020.
- [125] Alysha P Kishan and Elizabeth M Cosgriff-Hernandez. Recent advancements in electrospinning design for tissue engineering applications: A review. *Journal of Biomedical Materials Research Part A*, 105(10):2892–2905, 2017.
- [126] Jian Xiong, Ye Liu, Ailin Li, Liang Wei, Liming Wang, Xiaohong Qin, and Jianyong Yu. Mass production of high-quality nanofibers via constructing pre-taylor cones with high curvature on needleless electrospinning. *Materials & Design*, 197:109247, 2021.
- [127] Hao Fong, Iksoo Chun, and Darrel H Reneker. Beaded nanofibers formed during electrospinning. *Polymer*, 40(16):4585–4592, 1999.
- [128] Mohsen Zolfagharlou Kouhi, Tayebeh Behzad, Laleh Ghasemi-Mobarakeh, Alireza Allafchian, Zahra Moazzami Goudarzi, and Mohammad Saeid Enayati. Proceeding toward the development of poly (-caprolactone)/cellulose microfibrils electrospun biocomposites using a novel ternary solvent system. *The Journal of The Textile Institute*, 111(2):249–259, 2020.

- [129] Adnan Haider, Sajjad Haider, and Inn-Kyu Kang. A comprehensive review summarizing the effect of electrospinning parameters and potential applications of nanofibers in biomedical and biotechnology. *Arabian Journal of Chemistry*, 11(8):1165–1188, 2018.
- [130] Tianyu Yao, Honglin Chen, Pinak Samal, Stefan Giselbrecht, Matthew B Baker, and Lorenzo Moroni. Self-assembly of electrospun nanofibers into gradient honeycomb structures. *Materials & Design*, 168:107614, 2019.
- [131] Ji-Huan He, Yue Wu, and N Pang. A mathematical model for preparation by ac-electrospinning process. *International Journal of Nonlinear Sciences and Numerical Simulation*, 6(3):243–248, 2005.
- [132] Adam Mirek, Paulina Korycka, Marcin Grzeczkwicz, and Dorota Lewińska. Polymer fibers electrospun using pulsed voltage. *Materials & Design*, 183:108106, 2019.
- [133] J Corcoran and PB Nagy. Compensation of the skin effect in low-frequency potential drop measurements. *Journal of Nondestructive Evaluation*, 35(4):1–12, 2016.
- [134] P Pokorný, P Mikeš, and D Lukáš. Electrospinning jets as x-ray sources at atmospheric conditions. *EPL (Europhysics Letters)*, 92(4):47002, 2010.
- [135] Aaron M Drews, Ludovico Cademartiri, George M Whitesides, and Kyle JM Bishop. Electric winds driven by time oscillating corona discharges. *Journal of applied physics*, 114(14):143302, 2013.
- [136] Takahiro Koishi, Kenji Yasuoka, Shigenori Fujikawa, Toshikazu Ebisuzaki, and Xiao Cheng Zeng. Coexistence and transition between cassie and wenzel state on pillared hydrophobic surface. *Proceedings of the National Academy of Sciences*, 106(21):8435–8440, 2009.
- [137] Robert N Wenzel. Resistance of solid surfaces to wetting by water. *Industrial & Engineering Chemistry*, 28(8):988–994, 1936.
- [138] ABD Cassie and SJToTFS Baxter. Wettability of porous surfaces. *Transactions of the Faraday society*, 40:546–551, 1944.
- [139] Silvia Grande, Pieter Cools, Mahtab Asadian, Joachim Van Guyse, Iuliia Onyshchenko, Heidi Declercq, Rino Morent, Richard Hoogenboom, and Nathalie De Geyter. Fabrication of peot/pbt nanofibers by atmospheric pressure plasma jet treatment of electrospinning solutions for tissue engineering. *Macromolecular Bioscience*, 18(12):1800309, 2018.

- [140] Juliano E Oliveira, Luiz HC Mattoso, William J Orts, and Eliton S Medeiros. Structural and morphological characterization of micro and nanofibers produced by electrospinning and solution blow spinning: a comparative study. *Advances in Materials Science and Engineering*, 2013, 2013.
- [141] Xiaofeng Wang, Haibin Zhao, Lih-Sheng Turng, and Qian Li. Crystalline morphology of electrospun poly (ϵ -caprolactone)(pcl) nanofibers. *Industrial & Engineering Chemistry Research*, 52(13):4939–4949, 2013.
- [142] H Bittiger, RH Marchessault, and WD Niegisch. Crystal structure of poly- ϵ -caprolactone. *Acta Crystallographica Section B: Structural Crystallography and Crystal Chemistry*, 26(12):1923–1927, 1970.
- [143] Nadine Tenn, Nadège Follain, Kateryna Fatyeyeva, Fabienne Poncin-Epaillard, Christine Labrugère, and Stéphane Marais. Impact of hydrophobic plasma treatments on the barrier properties of poly (lactic acid) films. *RSC Advances*, 4(11):5626–5637, 2014.
- [144] Shamayita Patra, Sadiya Anjum, Alok R Ray, and Bhuvanesh Gupta. Effect of co2 plasma exposure on physico-chemical properties of porous polycaprolactone scaffold. *Polymer Bulletin*, 73(7):1875–1890, 2016.
- [145] Denis Mihaela Panaitescu, Eusebiu Rosini Ionita, Cristian-Andi Nicolae, Augusta Raluca Gabor, Maria Daniela Ionita, Roxana Trusca, Brindusa-Elena Lixandru, Irina Codita, and Gheorghe Dinescu. Poly (3-hydroxybutyrate) modified by nanocellulose and plasma treatment for packaging applications. *Polymers*, 10(11):1249, 2018.
- [146] Mpho Phillip Motloug, Vincent Ojijo, Jayita Bandyopadhyay, and Suprakas Sinha Ray. Morphological characteristics and thermal, rheological, and mechanical properties of cellulose nanocrystals-containing biodegradable poly (lactic acid)/poly (ϵ -caprolactone) blend composites. *Journal of Applied Polymer Science*, 137(19):48665, 2020.
- [147] Fatemeh Rezaei, Tom Planckaert, Chris Vercruyse, Jente Verjans, Pascal Van Der Voort, Heidi Declercq, Richard Hoogenboom, Rino Morent, and Nathalie De Geyter. The influence of pre-electrospinning plasma treatment on physicochemical characteristics of pla nanofibers. *Macromolecular Materials and Engineering*, 304(11):1900391, 2019.
- [148] Anna A Ivanova, Dina S Syromotina, Svetlana N Shkarina, Roman Shkarin, Angelica Cecilia, Venera Weinhardt, Tilo Baumbach, Mariia S Saveleva, Dmitry A Gorin,

- Timothy EL Douglas, et al. Effect of low-temperature plasma treatment of electrospun polycaprolactone fibrous scaffolds on calcium carbonate mineralisation. *RSC advances*, 8(68):39106–39114, 2018.
- [149] Sepidar Sayyar, Eoin Murray, Brianna C Thompson, Sanjeev Gambhir, David L Officer, and Gordon G Wallace. Covalently linked biocompatible graphene/polycaprolactone composites for tissue engineering. *Carbon*, 52:296–304, 2013.
- [150] Krzysztof Moraczewski, Magdalena Stepczyńska, Rafał Malinowski, Piotr Rytlewski, Bartłomiej Jagodziński, and Marian Żenkiewicz. Stability studies of plasma modification effects of polylactide and polycaprolactone surface layers. *Applied Surface Science*, 377:228–237, 2016.
- [151] Andreas Wurm, Evgeny Zhuravlev, Kathrin Eckstein, Dieter Jehnichen, Doris Pospiech, R Androsch, B Wunderlich, and Christoph Schick. Crystallization and homogeneous nucleation kinetics of poly (ϵ -caprolactone)(pcl) with different molar masses. *Macromolecules*, 45(9):3816–3828, 2012.
- [152] Kyusoon Shin, Euntaek Woo, Young Gyu Jeong, Chulkyu Kim, June Huh, and Kwang-Woo Kim. Crystalline structures, melting, and crystallization of linear polyethylene in cylindrical nanopores. *Macromolecules*, 40(18):6617–6623, 2007.
- [153] Xudong Chen, Gong Hou, Yujun Chen, Kun Yang, Yeping Dong, and Hui Zhou. Effect of molecular weight on crystallization, melting behavior and morphology of poly (trimethylene terephthalate). *Polymer Testing*, 26(2):144–153, 2007.
- [154] Lien Van der Schueren, Bert De Schoenmaker, Özlem I Kalaoglu, and Karen De Clerck. An alternative solvent system for the steady state electrospinning of polycaprolactone. *European Polymer Journal*, 47(6):1256–1263, 2011.
- [155] Assya Boujemaoui, Carmen Cobo Sanchez, Joakim Engstrom, Carl Bruce, Linda Fogelstrom, Anna Carlmark, and Eva Malmstrom. Polycaprolactone nanocomposites reinforced with cellulose nanocrystals surface-modified via covalent grafting or physisorption: A comparative study. *ACS applied materials & interfaces*, 9(40):35305–35318, 2017.

Appendix B

Research outputs

B.1 List of Publications

1. **Manikandan Sivan**, Divyabharathi Madheswaran, Sarka Hauzerova, Vit Novotny, Vera Hedvicakova, Vera Jencova, Eva Kuzelova Kostakova, Martin Schindler, David Lukas, “*AC electrospinning: impact of high voltage and solvent on the electrospinnability and productivity of polycaprolactone electrospun nanofibrous scaffolds*”. *Materials Today Chemistry*, 2022, 26, 101025.
Impact Factor (2021): 7.61 (Q1).
2. **Manikandan Sivan**, Divyabharathi Madheswaran, Jan Valtera, Eva Kuzelova Kostakova, David Lukas, “*Alternating current electrospinning: The impacts of various high-voltage signal shapes and frequencies on the spinnability and productivity of polycaprolactone nano fibers*”. *Materials & Design*, 2022, 213, 110308.
Impact Factor (2021): 9.41 (Q1). Citations: 18.
3. **Manikandan Sivan**, Divyabharathi Madheswaran, Mahtab Asadian, Pieter Cools, Monica Thukkaram, Pascal Van Der Voort, Rino Morent, Nathalie De Geyter, David Lukas, “*Plasma treatment effects on bulk properties of polycaprolactone nanofibrous mats fabricated by uncommon AC electrospinning: A comparative study*”. *Surface & Coatings Technology*, 2020, 399, 126203.
Impact Factor (2021): 4.86 (Q1). Citations: 17.
One of the images from this article has been featured in the cover page of the journal “*Surface and Coatings Technology*” 2020, 399.

4. Divyabharathi Madheswaran, **Manikandan Sivan**, Jan Valtera, Eva Kuzelova Kostakova, Tim Egghe, Mahtab Asadian, Vit Novotny, Nhung HA Nguyen, Alena Sevcu, Rino Morent, and David Lukas. “*Composite yarns with antibacterial nanofibrous sheaths produced by collectorless alternating-current electrospinning for suture applications*”. *Journal of Applied Polymer Science*, 2022, 139(13):51851. Impact Factor (2021): 3.05 (Q2). Citations: 5.
5. Caitlin Lawson, Andrei Stanishevsky, **Manikandan Sivan**, Pavel Pokorny, and David Lukas. “*Rapid fabrication of poly (ϵ -caprolactone) nanofibers using needle less alternating current electrospinning*”. *Journal of Applied Polymer Science*, 2016, 133(13). Impact Factor (2021): 3.05 (Q2). Citations: 35

B.1.1 The Web of Science or Scopus indexed Conference publications

1. Manikandan Sivan, Madheswaran Divyabharathi, Tomas Kalous, Pavel Pokorny, and David Lukas. “*Production of poly (ϵ -caprolactone) antimicrobial nanofibers by needleless alternating current electrospinning*”. *Materials Today: Proceedings*, 2019,17. Cite score: 2.3. Citations: 10.
2. Manikandan Sivan, *et al.* “*Hydrodynamics of fiber drawing from polymer solutions*”. *Fiber Society 2016 Spring Conference: Textile Innovations - Opportunities and Challenges*, ISBN: 978-295565600-6, Publisher Fiber Society.
3. Caitlin Lawson, Manikandan Sivan, Pavel Pokorny, Andrei Stanishevsky, and David Lukas, “*Poly (ϵ -Caprolactone) Nanofibers for Biomedical Scaffolds by High-Rate Alternating Current Electrospinning*”. *MRS Advances* 1, no. 18 (2016): 1289-1294. Cite score: 1.7. Citations: 2.
4. Divyabharathi Madheswaran,...., Manikandan Sivan, *et al.* “*Braided threads with AC electrospun nanofibers for hygienic and medical applications*”. *Proceedings 13th International Conference on Nanomaterials - Research & Application*, 2021.
5. Eva Kuzelova Kostakova,...., Manikandan Sivan, *et al.* “*AC Electrospinning; Theory and Applications*”, *Fiber Society 2022 Spring Conference: Textile Innovations - Opportunities and Challenges*.

B.1.2 Conferences

1. Manikandan Sivan, *et al.* “*Fabrication of poly(ϵ -caprolactone) Nanofibers using carboxylic acids by alternating current electrospinning*”. 1st Workshop on Mechanics of Nanomaterials, 2018, Czech Republic, ISBN: 978-80-7494-449-9.
2. Manikandan Sivan, *et al.* “*Analysis of electro-hydrodynamic instability involved in AC electrospinning*”. 1st Workshop on Mechanics of Nanomaterials, 2018, Czech Republic, ISBN: 978-80-7494-449-9.
3. David Lukas, Manikandan Sivan, *et al.* “*Stability analysis of AC electrospinning leads to nonlinear physics*”. Polish-Israeli Conference on Electrospinning & Tissue Engineering, 2018, Poland.
4. Manikandan Sivan, Divyabharathi Madheswaran, Pavel Pokorny, and David Lukas, “*Spinnability of poly (ϵ -caprolactone) using formic acid by needleless and collectorless alternating current electrospinning*”. NANOCON, 2017, Czech Republic.
5. Manikandan Sivan, David Lukas, and Pavel Pokorny. “*Poly(ϵ -caprolactone) Nano fiber for vascular Scaffold by Needle less Alternating Current Electrospinning*”. The 16th International Conference on Biomedical Engineering, Singapore, 2016.
6. Manikandan Sivan, Pavel Pokorny, and David Lukas, “*Spinnability of poly (ϵ -caprolactone) using formic acid by alternating current electrospinning*”. Workshop in Bila voda, 2016, Czech Republic. ISBN: 978-80-7494-293-8.

Manuscripts under preparation

1. Manikandan Sivan, *et al.* “*The coil-globule transition of polycaprolactone and its stability in the ternary solvent system*”.
2. Manikandan Sivan, *et al.* “*Controlling the drug loading efficiency through AC high voltage signal’s waveform and frequency*”.
3. Manikandan Sivan, *et al.* “*Analysis of electrohydrodynamic instability of polymeric liquid in the AC electric field*”.